A Thesis Submitted for the Degree of PhD at the University of Warwick

Permanent WRAP URL:

http://wrap.warwick.ac.uk/171955

warwick.ac.uk/lib-publications

Mixed Active-Passive Systems in Confinement

by

Stephen Williams

Thesis

Submitted to the University of Warwick

for the degree of

Doctor of Philosophy in Physics

University of Warwick, Physics Department

April 2022

Contents

List of Tables

List of Figures

Acknowledgments

"Run when you can, walk if you have to, crawl if you must; just never give up."

    - Dean Karnazes, American Ultrarunner

The first day of my PhD, sat already in the campus pub, someone told me "Over the next few years, you're going to be suffering". Although I can't remember who said it, I certainly remember the statement. But I also remember laughing back "Yes, probably, it'll be great!". This acceptance and lack worry stemmed from the many excellent people I have been fortunate to have around me.

The first of my thanks go to my supervisor Marco Polin, who's passion for science, astute discussions and oversight have contributed massively to my research during the PhD. Both my attention to detail and desire for self-scrutiny are skills I attribute to our collaboration. I have also had the opportunity to work directly with several other excellent scientists: Among these, Raphaël Jeanneret and Idan Tuval played a central role in my development; welcoming me to their Lab at IMEDEA in Mallorca and teaching me experimental techniques. As well as this, Raphaël taught me much about data analysis and presentation. Skills that, to this day, I lean on almost daily. During my PhD I have been based within the Warwick Soft-Biological Physics group. The many presentations and seminars were always a great pleasure and a great reminder of the rich perspectives and ideas people around me have. Many thanks to: Simone, Richard, Maria, Antoine, Iago, Ollie, Lewis, Paul and Stefan. With each I had the pleasure of sharing many chats, coffee breaks and trips to Varsity.

As well as the many people who kept me going while at work, just as many

provided their endless support outside of work, and for which I am eternally grateful: My parents Christine and Clive, my brother Michael and, last but not least my girlfriend Emily. Each has followed along the whirlwind, largely by way of mid-day phone calls. To receive such support has always been a great privilege.

To the many friends I've made during my time at Warwick: My fellow Physics Postgraduates, the University of Warwick Big Band members, the Wind Orchestra, Feelin' Saxy, all of the members of 95 Radford Road and many more!

This thesis is dedicated to all the great company shared along the way. Without which, my work would surely not have been possible!

Declarations

I declare that this thesis reports the work I carried out between October 2018 and March 2022 under the supervision of Dr. Marco Polin. The studies in this thesis have not been submitted either in full or in part to this or any other academic institution for the admission of a higher degree. In exception from where clearly indicated by reference in the text, any work reported in this thesis has been performed by myself. Any views expressed in this thesis are those of the author.

Chapters 3 & 4 are based on the manuscript which is currently under review for publication, with work performed during the course of the PhD:

- S. Williams, R. Jeanneret, I. Tuval, and M. Polin. Confinement-induced accumulation and spontaneous de-mixing of microscopic active-passive mixtures, 2021

The contribution to the manuscript are as follows: RJ, IT and MP conceived and designed the experiments. RJ and SW performed the experiments. RJ, SW and MP analysed the data. RJ developed the analytical model and SW performed the numerical simulations. All authors jointly discussed the results and wrote the manuscript.

Abstract

The dynamics of passive colloidal particles are explored when they interact with active *Chlamydomonas reinhardtii*, a green micro-algae. Through the implementation of different confining microfluidic geometries, we examine the resulting colloidal distributions and characterise the interactions which lead to them. Experiments are outlined in which we characterise the positional dependence of the 'jumps' passive particles undergo, which result from interacting with the active particles. These jumps are then used to reconstruct the overall positional distributions. Additionally, we outline experiments performed in a circular microfluidic confinement. By exploiting the aforementioned positional distribution of colloids and a semi-permeable membrane, this microfluidic device can be used to segregate the passive particles out of the mixture. Finally, features of a model are outlined which allows for the modelling of active-passive mixtures. The active particle of which is easily tuneable, allowing both pusher or puller type swimmers, as well as a variety of boundary scattering behaviours. Results show that confinement results in inhomogeneous swimmer dynamics, which then feed into the behaviour of passive particle dynamics. Microswimmer confinement is a clear example in which spatial inhomogeneities lead to passive particle accumulation and, upon implementing a semi-permeable membrane, can be used to perform particle demixing. Such interactions present exciting new possibilities for controlling micro-scale particles using active particles whose dynamics have such spatially dependent characteristics.

Chapter 1

Introduction

1.1 Outline and Structure

In this thesis the focus will be primarily systems which are made up of both active and passive particles, which exist in a state of confinement. The result of which leads to inhomogeneous active forces acting on the passive particles. The primary aim of this work is to introduce a relatively simple experimental system that combines active matter, passive matter and confining geometries. Pair-wise, these concepts have been relatively well studied as we will see in the literature, but we hope to build on this to understand their combined effect. We specifically focus on the impact of confinement and active particles on the dynamics and positional distributions of passive particles. In doing so, we largely neglect the impacts of passive particles on active. However, the systems considered are relatively dilute and the passive particles small, so this impact is expected to be minimal. To understand the impact on passive particles, we first ask what the positional distribution of the particles is in confinement when subject to an active bath. Next, we will try to address whether this resulting distribution can be understood by solely looking at the passive particle's dynamics, treating the motion as a coloured noise with thermal and active contributions. Based on this understanding we will attempt to describe the minimal considerations required to replicate such systems and also present numerical models of modified active-particles to see how further changes can be made by choosing different types of swimmer. Finally, we will introduce a simple experimental set-up that exploits features of the distribution to see whether it is possible to exploit the coloured noise to de-mix the active-passive mixture.

In this first chapter we will introduce active matter and some of its research history, microswimmers and their behaviour in confined environments. After this,

we will review the literature on mixed systems, composed of this active matter and passive matter. In this review we will look at the body of research that details the properties of such mixed systems. Next, we will look at a few select examples in which the understanding of mixed system enables us to solve real world problems: drug micro-delivery mediated by microswimmers, controlling the construction and melting of colloidal crystals using active interstitial particles, and the construction of exotic actively driven engines to produce meaningful work. Finally, the chapter will be concluded with a brief discussion on the origin of active displacements of passive particles.

In chapter two, several background topics will be outlined, relevant to the later chapters will be given. The topics are partitioned into four sections: experimental, data analysis, computational and theoretical. Within the experimental section we first introduce *Chlamydomonas reinhardtii*, the microswimmer that is used throughout as the active component of our mixed systems. Next, we detail the various techniques required to perform the microfluidic experiments, the results of which are then discussed in chapters three and four. The data analysis section details an algorithm used to process experimental images and extract positional information for the various agents within the system. The computational section focuses on the key statistical concepts that we focus on, the Poisson process and exponential distribution. After this, we discuss how, using acceptance-rejection schemes and inverse sampling tools, we can resample experimental distributions to make predictions about the system. These computational techniques are used extensively in chapter three alongside measured experimental data. We then go on to outline Milstein's Method, an algorithm which can be applied to stochastic systems which have spatially dependent noise. By including an extra drift term, which depends on the integration scheme employed, we can simulate such systems. We see in chapter four Milstein's algorithm used to make dynamic predictions of the particle's dynamics. The final computational topics are the Weeks-Chandler-Andersen force and numerical solutions for stochastic differential equations. The two topics are core to chapter five, in which they are used in tandem to simulate a model microswimmer interacting with passive particles. Within the Theoretical section we discuss briefly the Kramers-Moyal expansion, a Taylor series expansion of the Master equation. The expansion can be used to solve for a distribution for which the master equation is an integro-differential equation, allowing us to represent such a system as approximately a drift-diffusion system. Finally, we detail the narrow escape problem, focusing on the the relevant equations needed to calculate the time we should expect to elapse for a Brownian particle to reach a small absorbing portion of a reflective

boundary. The topics are presented here, so as to make more clear for the reader method used during later chapters, without distracting from the core results and discussions too much. These will also be cited explicitly during the later chapters to highlight, where they are directly relevant.

Chapter three will begin by discussing a series of experiments. The design features and choices will be introduced before moving on to the results. The overall arc of this research is as follows: first, by measuring the steady-state colloidal distributions within a straight channel. Then, by looking at the particle dynamics on an individual colloid level, specifically focusing on 'jumps' in the measure trajectories as their key feature. Finally, using numerical and semi-analytical models, which contain the different measured dynamical properties of the jumps, we reconstruct the main features of the steady-state.

Chapter four will outline the details of a second set of the experiments. Here, the experiments are focused on utilising key features of the steady-state discussed in chapter three to segregate the colloids. As with chapter three the chapter opens by discussing the experimental design. We will see that within the altered circular geometry that the steady-state features are very similar. Next, we discuss the use of a semi-permeable membrane to de-mix mixtures of colloids and swimmers. Next, we measure the dynamics of this de-mixing process. Finally, using the measured jump properties from chapter three, we show that the de-mixing dynamics can also be understood in terms of these jumps.

In chapter five we will introduce a 2D model of active self-propelled-particles which are mixed with passive particles. Using the various properties of the active particles, as well as a novel near-boundary Poissonian 'kicking' process to replicate microswimmer scattering, we attempt to capture the behaviour of a broad range of microswimmer mixtures. The chapter opens by describing the various features and origins of the model and some of the tools used to produce particle trajectories. After this, the data is given a similar treatment to that detailed in chapter three: using passive trajectory jumps to attempt to reconstruct steady-state distribution features.

The final conclusions chapter will be divided into two main sections: the first of which will sequentially outline the chapters' main results and outcomes. The second half of this chapter will outline briefly the remaining open questions and ideas to progress further the research.

1.2 Active Matter

Active matter is made up of a large number of agents which can utilise energy from their environment and as a result produce directed motion [1, 2]. Its study often involves an exciting mixture of both interdisciplinary work, and inter-field techniques from across physics. These different tools which have been drawn on are numerous, chief amongst these techniques from low Reynolds number hydrodynamics, kinetic theory and statistical physics. Many of which require modification owing to the fact that the systems involved are constantly consuming energy. Active particles, such as microswimmers, consume nutrients within their environment and by using different chemical processes are able to produce mechanical motion. This means that they cause fluxes of energy within their environment, changing it in such a way as that it can no longer be considered to be in thermodynamic equilibrium. Because of this, we refer to active matter as example of an out-of-equilibrium system. This is one of the core reasons why these systems are so interesting to the physics community, as they allow exploration into these non-equilibrium processes using familiar tools, which in turn leads to these tools becoming enriched or enhanced.

The study of active matter has taken place largely within the last half-century, often as a result of the application of techniques, both experimental and mathematical, to problems from traditionally different scientific fields. Progress within the study of active matter has many important implications to our understanding of many real world systems. Development has enabled a level of realism within modelling of several real world systems, for which equilibrium is rare, opening the possibility of addressing a broad class of previously inaccessible problems. An example of this is is present in the study of polar flocks in two-dimensions. Equilibrium equivalents of such such systems are bound to obey the Mermin-Wagner theorem, which means that at low-dimensionality there is no presence of spontaneous symmetry breaking and thus, at best, quasi-long-range order. However, for models that include the agent's energy consumption we can see long-range order, an insight which fundamentally contrasts that of the equilibrium case [2]. As well as theoretical advancements, active matter presents possible solutions to many of the most challenging problems we face, to name a few key to this: understanding the impacts and effects of microplastics within populated environments, improving the toolset of medicine for targeted delivery of drugs within the body, and alternative energy production using stochastically driven engines. In each of these highlighted cases we see that there is a clear interaction between a passive component of the system with an active. Focusing on the drug delivery case, we have the cargo, which

will be a passive particle that we want to deliver to a specific site within the body of a patient, and the active agent which performs the delivery. It is these sort of mixed systems we are primarily interested in. Such mixed systems form the basis of a body of exciting new research, in which the system being studied see this extra dimension of complexity with different types of particles interacting.

Throughout this introduction, we will be focusing on the most relevant example of active matter to our study: microswimmers. A brief overview on researches in active particles in confinement will be provided. Following this, there will be a brief discussion on early progress in mixed systems and the types of problem people are interested in. An overview of some of the most exciting developments in mixed active passive systems will be presented. Finally, a presentation of the two main sides of the research concerning active displacements. Addressing why, in this thesis, we are able to bypass this type of inquiry.

1.3 Microswimmers

The directed motion of bacteria had been studied as far back as 1901 [3], but was popularised largely within physics by the works of H. Berg [4, 5, 6] and later in E. M. Purcell's seminal paper 'Life at Low Reynolds Number' [7]: These works primarily highlight that viscous forces are hugely dominant over inertial at the scales at which microscopic locomotion occurs (the ratio of these forces is known as the Reynolds number). These organisms play largely by the rules dictated in the Navier-Stokes equations, a set of partial differential equations which can be used to describe motion of, and in this case within, viscous fluids. The Navier-Stokes equation is given by,

$$\rho \left[\frac{\partial \boldsymbol{V}}{\partial t} + (\boldsymbol{V} \cdot \boldsymbol{\nabla}) \boldsymbol{V} \right] = -\boldsymbol{\nabla} P + \rho \boldsymbol{g} + \mu \nabla^2 \boldsymbol{V}, \tag{1.1}$$

$$\boldsymbol{\nabla} \cdot \boldsymbol{V} = 0. \tag{1.2}$$

Here, in equation (1.1) ρ is the fluid density, $\boldsymbol{V}$ describes the resulting flow-field of the fluid, the term containing P encodes the effects of pressure gradients, $\boldsymbol{g}$ the external body forces (gravitational etc.) acting on the fluid and μ the dynamic viscosity which results in diffusion. Equation (1.2) is the continuity equation which comes as a result of considerations of mass conservation. We can determine the importance of the relative contribution of inertia and viscocity by considering the Reynolds number, which is defined as

$$\mathrm{Re} = \frac{\rho V \ell}{\mu}. \tag{1.3}$$

Here, ρ, μ and $V = |\boldsymbol{V}|$ are as previously defined, ℓ is the length scale that characterises the length scale of interest. Due to the fact that for microscopic organisms operate on small length scales ℓ and at relatively high viscosities μ, the Reynolds number in such systems is often very small, allowing us to neglect the inertial contributions to the Navier-Stokes equation. Inertial forces are, of course, very familiar from physical intuitions gained by living at a higher Reynolds number. People who frequently swim (where the Reynolds number is of the order 10^4) will note that, by pushing off the wall with a good body positioning, it is possible to coast and a human swimmer's motion will not be immediately arrested. A distance of a few meters can be covered by a human swimmer before it becomes beneficial to begin using a swim stroke. This is an example of inertially driven motion, since it takes a good amount of time for the drag from the water to slow the swimmer down. In contrary to this, for our microswimmer for whom the Reynolds number is on the order of 10^{-4}, they will have mere microseconds before viscous forces halt their motion. Through the inertial term's omission, which comprise the left hand side of (1.1) we get the Stokes equation,

$$0 = -\boldsymbol{\nabla} P + \rho \boldsymbol{g} + \mu \nabla^2 \boldsymbol{V}. \tag{1.4}$$

Such systems if they are subject to kinematic reversibility, the property that reversing the sign of the instantaneous forces and torques the swimmer is subject to reverses the sign of the flow-field but does not change the pattern, gain time reversibility [8].

If a microswimmer's motion acting on a fluid moves the organism forwards, the reverse of that motion (i.e. the motion in reversed time) will move it equally backwards (a visual example of this can be seen in [7]). As such, organisms which aim to swim in these conditions cannot use this kind of reciprocal motion. However, many strategies have evolved to overcome this limitation by using non-reciprocal motion for translation at low Reynolds number. Organisms, such as *Escherichia coli*, swim using flagellar motion [5]. The flagella in the case of *Escherichia coli* turns in a corkscrew-like manner. Since the bacteria can continue to turn the flagella in a single direction the motion is non-reciprocal, and as such fluid translated by the flagella allows for propulsion at low Reynolds Number.

Flagellates form a group of such microswimmers who swim in similar ways to this. Within this group there are a few different strategies of note: firstly, different
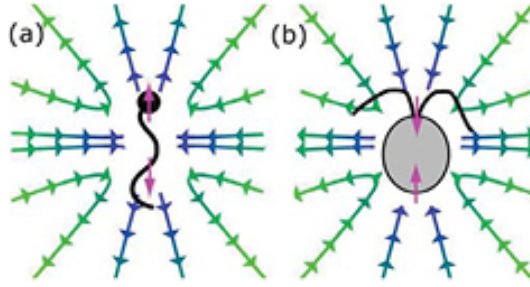
Figure 1.1: **Flow field for a pusher and puller.** Taken from: [13]. (a) Here we see the flow field for a force dipole resulting from a pusher. (b) Here we see the flow field for a force dipole resulting from a puller.

organisms have different numbers of flagella, *Escherichia coli.* for example, can be uni-flagellate (possessing only one flagella). But *Escherichia coli* is more commonly multi-flagellate, with many flagella protruding from it's body, which rotate around each other to form a bundle [9]. Further examples of uni-flagellate microswimmers include spermatozoa, *Mircomonas pusilla*, etc. As mentioned before, swimmers can be multi-flagellate, this class includes many types of bacteria, as well as some eukaryotes such as *Giardia* [10, 11]. Finally, there are several important bi-flagellate organisms. *Chlamydomonas reinhardtii* (CR) is in particular a popular example, owing to its relative simplicity [12]. As well as the number of flagella, another classification exists that separates the swimmers into two groups, whether a swimmer is a pusher or a puller. Self-propelled swimmers induce flow fields which is the far-field is well described by a dipole [8]. We can see a comparison of these in figure 1.1. In (a) we see a pusher, drawing the fluid in from the sides and pushing it outwards both in front and behind, while in (b) the fluid is pulled from in front and behind and pushed out the sides. Notice, in both cases the dipoles point in opposite directions leaving the swimmer force-free.

Pushers swim with their flagella behind their body, pushing the fluid behind them to move forwards. This group includes *Escherichia coli* and spermatazoa. On the other hand the pullers, which have their flagella in front of them as they, move using a breast-stroke-like motion to pull the fluid past them to enable motion and this group includes CR. Some rarer organisms are capable of the use of both of these types of motion. For example *Mircomonas pusilla*, which can be a pusher or a puller, depending on how its flagella moves [14].

These organisms swim, in the simplest description, in a manner known as run-and-tumble [7, 15, 16]. What this means is that the trajectories resulting from their motion are made up of ballistic 'runs'. Within the trajectories then are interspersed
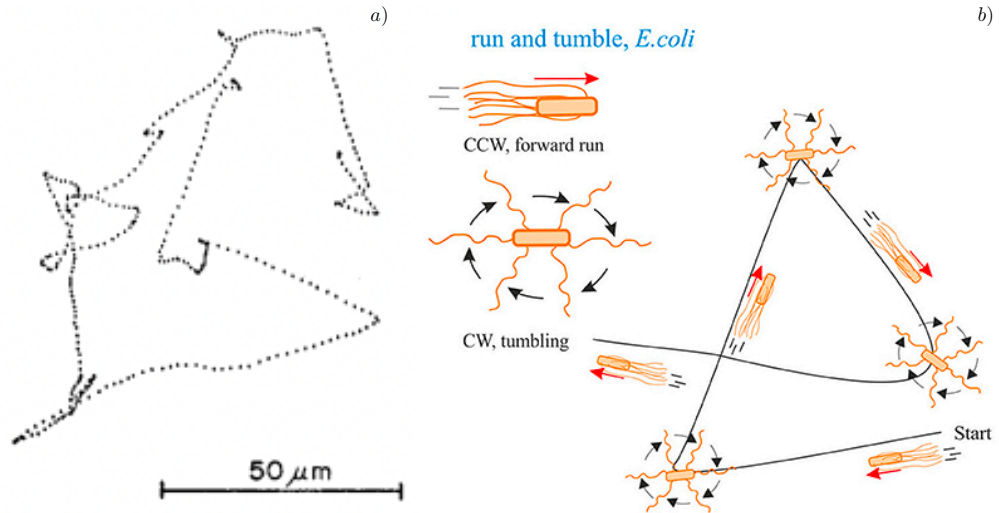
Figure 1.2: **Schematic of Run-and-Tumble Motion in *Escherichia coli*.** (a) Taken from [7], shows an experimentally tracked trajectory of a swimming *Escherichia coli*, using temporally equally spaced dots to show the distinct types of motion. (b) Taken from [17], shows a schematic of the motion, with the flagella changing their behaviour to reorient the swimmer.

'tumbles', in which the swimmers stop moving, randomly reorienting their direction, before undergoing another 'run'. A schematic and example of this is given in figure 1.2.

By modifying aspects of this run and tumble motion using feedback mechanisms, the organism is able to perform the various taxis, often to maximise favourable conditions: chemical, light, etc. This can be achieved by exploiting various mechanisms within the organism. Chemotaxis, for example, in some bacteria is performed by using an internal memory of detected local chemical concentration. Based on the temporal gradients experienced in this measured concentration the tumble rate is modified to give motion up the gradients [4].

In modern times there has been development around more exotic types of experimentally realisable active particles. Some experimental systems of synthetic microswimmers have become prominent in the literature. Janus particles in particular can be used as a close experimental equivalent of active Brownian particles [18, 19]. Janus particles are made up of two distinct faces, which either have different physical or chemical properties. This difference leads to symmetry breaking allowing translational motion when subject to various phoretic mechanisms: chemotactic

[20], thermotactic [21] or phototactic [22], to name just a few. Exploiting these then enables an experimental set up which mirrors closely the 'active Brownian particle' (ABP) studied widely in computational literature. While on the other end of the organic-synthetic scale there are some reports such structures as enzymes, which are traditionally considered passive, too act as active particles [23].

1.4   Active Particles in Confinement

Throughout this thesis, confinement is implemented as the method of creating non-homogeneous environments in which passive and active particles can interact. For passive particles, confinement will largely mean that at very close-range they will be physically blocked from continuing their motion. However, for swimmers, much as is the case when they undergo chemo/thermo/photo-taxis, the result of such confinements also result in a long-range change in their behaviours. As such, geometric confinement will be the fundamental way in which the swimmer's behaviour, throughout the research presented in this thesis, is modified. However, in a more general sense, considering the effects of confinement on active matter allows us to add complexity to the system being studied. The result of this is moving us closer to descriptions of real world systems, in which more often than not active matter is found in confined environments. Since, in this thesis we aim to describe active matter's interaction with passive matter, first looking at the literature on active matter's interaction with large immobile passive boundaries is a good place to begin. Separately, then considering active matter with passive particles without the presence of boundaries. Finally, literature which considers all these ideas together. The core theme of which will be to see how, swimmer behaviour as modified by the presence of boundaries, then mediates the passive particle behaviour.

   People for some time have studied active particles of all forms alone in confined environments. Specifically, there has been a focus on their transport dynamics and the modification of their collective behaviours when confined [24, 25, 26, 27, 28]. One of the key results, which will be referred to extensively, is that confinement modifies active particle positional distributions near boundaries. It has been shown that active particles in confined environments generally have a tendency to accumulate near to such surfaces. This accumulation is the result of of an asymmetry in the processes individuals are subject to which bring microswimmers towards boundaries and those that move them away. When an active particle is at a boundary it is effectively stuck at that boundary until it is able to turn away from it [29, 30, 19]. As well as this the hydrodynamic effects of individuals play a role in the near boundary be-

9

haviour of microswimmers [31]. It has been experimentally shown in *Escherichia coli* that close to surfaces the swimmers trace out clockwise circular trajectories, staying close for extended periods of time. In [31], it is then shown that this motion can be understood by considering the hydrodynamics of a force and torque-free swimmer close to a no-slip surface. The flagella must have a force on it, acting perpendicular to both the direction of motion and the outward normal of the boundary, to satisfy the non-slip conditions at the boundary. Thus, the swimmer moves in circles along the surface. Such active particles, which are near to boundaries, can then cause interruption of more nearby swimmers in collisions. The effect of these collisions in denser systems is traffic-jam-like, with clusters of swimmers clumping together close to boundaries as a result of this collective effect. We can see an example of such an accumulation in figure 1.3: showing a strong preference of the swimmers, in this case a strain of *Caulobacter crescentus*, to congregate near the boundary. In [24] a simulation of this effect is presented. At low swimmer concentrations it was shown that at low concentrations there is indeed a strong accumulation of the swimmers near to the boundaries. However, as the concentration is increased large-scale flows emerge leading to enhanced mixing of fluid across the channel, moving the accumulation peaks further from the boundary as the concentration increases.

1.5 Mixed Active-Passive Systems

Up to this point, we have discussed the studies of different biological systems in isolation using the tools of physics. However, it should be clear that in the real world these sorts of systems rarely appear in isolation. The natural question is, how many real world complexities can we include into models of these sorts of systems, while still allowing us to gain meaningful insights: specifically, can we model the interaction of active matter with free moving passive matter? There are, of course, a large number of considerations within this question: from relative active particle to passive particle size ratio, passive particle shape, active & passive particle density, to name just a few. Within this section we will aim to discuss some of the work done regarding such considerations, the resulting properties in such mixed systems and their resulting practical applications. As highlighted at the beginning of this chapter, several mixed-system problems are central to solving of the most pressing issues in modern times. Understanding the interactions of passive particles with active could lead to breakthroughs in emerging technology, such as micro-scale targeted cargo-delivery for drug delivery. As well as this, mixed system research plays an important role in helping to understand, and perhaps even mitigate, the
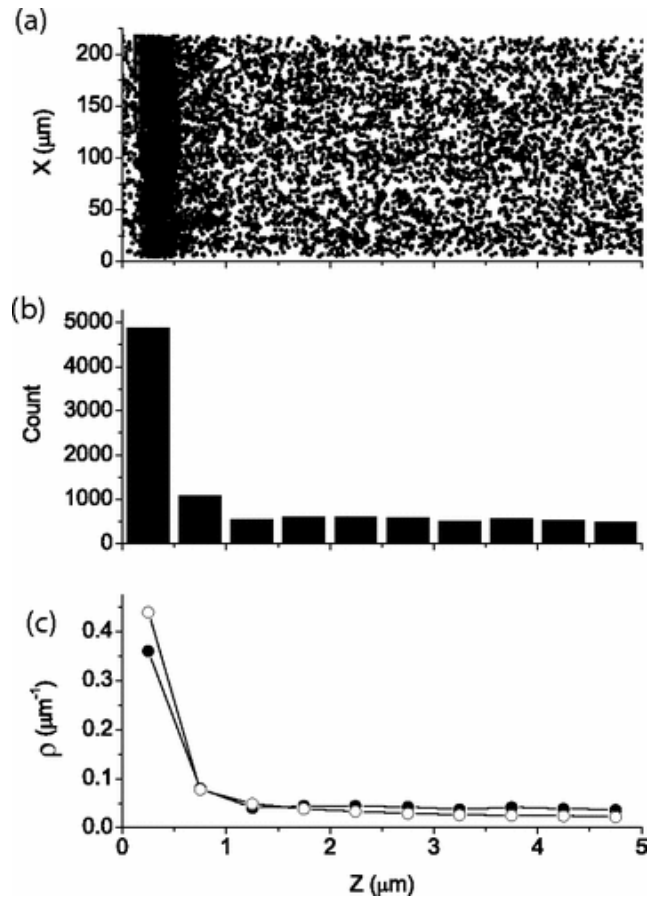
Figure 1.3: **Swimmer Positional Distributions Near to a Boundary.** Taken from [29]. (a) Shows a Z-X plot of over 10000 measured cell positions from 699 cell trajectories close to a boundary (Z=0). (b) Shows a histogram of the measurements shown in (a). (c) Shows a comparison between the experiments (solid circles) and model (clear circles) outlined in the paper.

stress that microplastics currently pose for aquatic environments. In this case, research can allow us to better understand how different species, for example motile algae, interact with microplastics in their natural environment and whether this results their transport via bioconvection or accumulation of such pollutants. Finally, these systems could allow new methods for the design and production of functional materials, with active interstitial colloids being used to modify colloidal crystal growth.
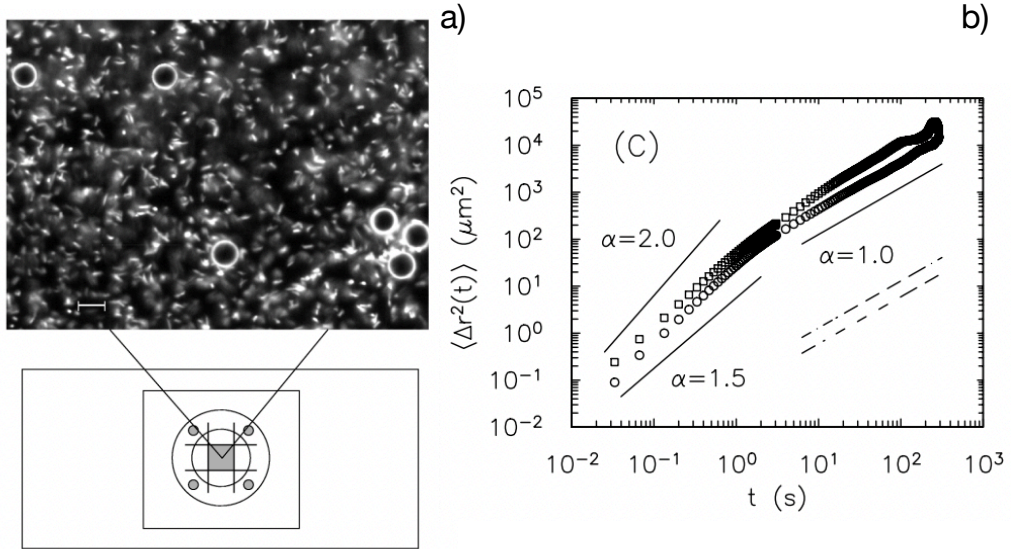
Figure 1.4: **Schematic of tracers in a bacterial bath and their enhanced diffusion.** Taken from [32]. (a) Here we see 10μm tracers (solid black circles with white outline) in a bath of swimming bacteria. Below shows the experimental schematic: a soap film (grey square), the humidity of which was maintained by four water-droplets (grey circles). (b) A log-log plot of the mean squared displacement of the tracers measured in the experiments. In the bottom left the gradient expected of the thermal diffusivity of 4.5μm and 10μm particles is shown respectively.

1.5.1 Enhanced Diffusion: The Birth of Mixed Systems

Some of the earliest work in mixed systems came about in 2000. In [32], an experimental set-up is described which utilised a soap film which contained both swimming bacteria and passive tracer particles of 10μm. The tracers were then tracked to see how the presence of active particles effected their behaviour. A schematic of the set-up can be seen in figure 1.4a. The key result noted is presented in figure 1.4b is the presence of super-diffusion of the passive colloids at short timescale and a recover of the normal diffusion at longer. The effect initial was thought to be a crossover of the dynamics from overdamped to an underdamped regime, however due to the system being at low Reynolds number it cannot be as a result of inertial effects. It was found instead to be the result of transient formations of coherent structures within the active bath. The crossover time from the long to short time dynamics was found to correspond to the life-time of such structures and to linearly increase with the bath concentration. The overall contribution of the two time-scles was found to result in an effective temperature (in the sense of the Stokes-Einstein

equation) between 2-3 orders of magnitude above that of room temperature within the bath. This observation is also the key take away for many other similar studies [33, 34, 35, 36, 37, 38, 39, 40, 41, 42] and could easily be considered central to the field of mixed-system research. These studies of bacterial-colloid mixtures span over the last two decades and probe a wide range of properties of tracer diffusion in bacteria of various densities. The different studies use vastly different tools, albeit commonly they approach the presence of super-diffusion: some using pair interaction, others the collective behaviours and, some with analogs to fluid dynamics phenomena, such as Taylor dispersions within the underlying space [39].

As well as this, starting in 2009 with [43] we start to see experimental studies capturing this enhanced passive particle diffusion in a broader class of microorganisms. In this case, and in many others, this is CR [44, 45, 46, 47, 48, 49]. Again, we see in the literature a vast toolset being applied to understanding the enhancement of the tracer dynamics for mixed systems. These result suggest a universality, that many kinds of active matter are capable of inducing enhanced diffusion on tracer particles they are in contact with. This has important implications for the various applications we have highlighted (e.g. drug microdelivery) since one of the key tools they require is fine control of microscopic particles. Controlling micron scale passive particles within different environments is of course a difficult task. However, as we have previously noted, the different types of active matter are capable of responding to various environmental stimuli: light, chemical concentration, thermal, etc. These sorts of environmental changes are relatively easy to induce and hence, controlling active particles on these scales. Thus, if we can understand how the transport properties of passive particles is affected by active particles, this is a possible way in which passive particles can be controlled within these scales. With such a wealth of experimental results, beginning early in the history of mixed systems we start to see computational models [50]. The early approaches use straightforward modelling, mixed systems containing two different species. This being an ABP with an active driving force and another passive particle subject to thermal diffusivity. Many such other studies have then followed along these lines in an attempt to study the diffusion of tracers within a toy-model setting [51, 52, 53, 54, 55, 56, 57, 58].

Janus particle, the synthetic microswimmers, then acts as a kind of bridge, that has emerged in the literature between these real world experiments and simulated systems [59, 60, 61, 62, 63]. As mentioned in section 1.3, Janus particles become active through many different mechanisms. As such, this has enabled verification of our theoretical understanding in systems composed of biological swimmers. They also present a start-point for us to begin to, by exploiting various environmental

stimuli in a controlled laboratory setting. By inducing directional motion in these active particles, we can then modify the transport properties of passive particles to gain precise control of passive objects.

With this expansion of research to many types of swimmer; in more recent studies, we also see a diversification of the tracer particles which are being studied: from elongated or elliptic particles [45, 49, 64, 51], or polymer chains [65, 66, 67, 68, 69, 56], to exotic asymmetric structures [70, 71]. Such tracers, specifically those with of asymmetric shape, once again present exciting possibilities for applications where the precise control of micro-structures is desirable. Since, the literature clearly shows for such objects, when under the influence of active particles, this is an induced overall directed motion.

Another key topic in active-passive mixture research is the concept of the 'active bath'. Which comes about largely from studies ignoring the specific features of the swimmers. This result should be unsurprising given the vast (but not exhaustive) list of organisms and swim strategies for which this enhanced diffusivity has relevance. The result of this view of the systems; instead, we present the passive particle as existing within an 'active bath'. As far back as the earliest papers this was an idea that was present [32], with the enhanced diffusivity measured by tracking the colloid motion without consideration of the active-displacements which the colloids underwent to drive this enhancement. The passive particle when in an active bath must then be subject to two distinct types of noise. The first of which is the standard Gaussian white noise which results from the thermal activity of the particle. The second is a coloured-noise, which comes as a result of the presence of the active particles [72]. This is a highly prevalent idea that is present throughout the body of mixed systems literature.

1.5.2 Frontiers of Active-Passive Research

In this section, we will introduce very briefly a few of the recent key developments in mixed system research. Some speculative research papers looking at potential medical or biotechnological applications, others, the production of exotic structures.

A few studies of the application of active particle to emerging medical technologies have been reported in the literature. One of the most important mixed system researches of this kind is the control and delivery of microscopic compounds. Specifically, within the human body, for use in techniques such as personalised medicine and drug micro-delivery. Using appropriately chosen active matter, the

introduction of which does not have negative effects on the patient, the hope is, with sufficient understanding this topic could lead to the invention of new medical technologies. In [73], it was demonstrated that for a given three-dimensional microstructure, that active particle accumulation could be induced. Given previous result on the behaviour of active particle in confinement, this alone isn't new. However, in this study as well as the accumulation of bacteria they demonstrated that passive colloidal beads were also accumulated in such areas. The concentration of these colloids was shown to be strongly increased or decreased given the local topography of the underlying structure. An exciting result, suggesting that such micro-control of particles is not too far out of the reach of current technology.

As well as this, with increasing amount of plastic pollution being introduced into marine environments [74] there is ever-present interest in understanding how this plastic will manifest within such environments, the interaction with native organisms and the associated outcomes [75]. A good example of this interdisciplinary exchange of ideas is given in this pair of articles [76, 77]. The first paper [76] concerns bio-mixing by krill of nutrient-rich water. It poses the question as to whether swimming organisms can induce significant mixing in marine environments, an idea presented as counter intuitive since the majority of organisms involved are on a length scale of less than 1cm. Concluding that in fact, due to the low efficiency of small mixers and the rarity of large that the overall affect of biomixing is likely to be low. The second outlines a toy-model, using a Stokesian model of mixing in krill-like systems, of lengths in the cm scale. The conclusions of this research are mixed on the importance of biomixing. Specifically, that within a school of active particles, even those of a small scale, the impact is significant and results in a diffusion as much as five times higher. However, it's stated outside such schools of active particles the results are less clear due to the simplicity of the modelling. It is hopefully clear from this example, a greater understanding of the interactions of mixed systems can reveal insights contrary to intuition.

There is also a lot of interest in different accumulation behaviours that can be observed in mixed systems. A range of such behaviours have been observed contrasting the thermal case. In [78], systems who's accumulation profile is tuned by active particle dynamics are studied. It was observed that passive particles which are subjected to an optical potential, both smooth and containing a speckle pattern, will accumulate. However, in the presence of an active bath this effect is disrupted. The characteristics of which depend on the type of optical potential applied, with smooth potentials seemingly accumulating with a longer time-scale and rough leading to a depletion in the region of the optical trap. This effect is because

15

the active particle's long time dynamics are modified by such potentials. Thus, the accumulation behaviour of the the colloids can be modified by controlling the underlying active particle dynamics. Much research has focused on such clustering of colloids in active baths, with the swimmers inducing long-ranged interactions between the colloids which would otherwise not be present [79, 80, 81, 82, 83, 84].

Another exciting area in which the study of mixed-systems have found application is in the growth dynamics of colloidal crystals. One main issue of the formation of colloidal crystals is that due to the rapidity of their formation by condensation, often metastable gels will instead form. However, computational evidence suggests that by using mixtures of active self-propelled particles and colloids, it becomes thermodynamically favourable for crystalline structures to form [85, 86]. In [87], an experimental set-up is demonstrated of active colloids undergoing dynamic accumulation changes. The colloids, when illuminated, formed colloidal crystal and dissolved when the light was removed. The self-assembly was noted to be the result of propelling forces, osmotic effects and the coupling between the active colloids and passive tracers in the mixtures. As far back at 2015, there has been speculation that active-passive colloidal crystal systemscould be expanded upon, to give systems where users have precise control, to manually design and oversee supra-colloidal assembly [88].

In section 1.5.1 we saw several papers focussed on the enhanced diffusion of increasingly exotic passive structures. It has been noted that, for certain passive structures, directed motion can be achieved by the introduction of active particles [89, 41, 90, 59, 91]. Further to this, ratchet effects in asymmetric passive structures resulting from active particle influence have been observed [92, 93]. From these topics, research has lead naturally to the development of stochastic engines. Systems in which a passive (often colloidal) particle in contact with an active bath is used to extract useful work [94, 95, 96, 97, 98, 99]. A recent review published [100] looks at the body of literature emerging on this exciting new topic: from the descriptions of such systems, to their overall efficiency as compared to equilibrium cases.

1.6   Active Displacements

The phenomenology and applications of mixed systems, it is hopefully clear, is rich and diverse. Up until this point the different effects that have been highlighted are the outcomes of the interaction of the active and passive particles. However, we may also ask, what aspects of this interaction actually lead to these effects. The answers to this question largely falls into two categories: the hydrodynamic effects

and the steric effects.

Within the hydrodynamics literature the swimmers are largely modelled either as Stokesian dipoles (or squirmer) [101, 102, 103] or using slender body theory [104, 105]. These approaches note as outcomes for such models: the enhancement of the transport properties in some cases [106, 107, 108, 109] , novel features like pair-wise interactions between passive particles [110, 111] and, loop-like trajectories caused in the far field of the microswimmer [112]. With these systems often focusing on swimmers much smaller than the tracers they are interacting with, to minimise the contributions of the contact forces. The steric effects then report similar results for given, but often much larger, scales with colloids of comparable size to the swimmers [46, 113]. With some small body of research highlighting specifically the features of these steric contact events [114].

Although these different approaches to the origin of active displacements, and indeed the distance at which they are relevant, are distinct. It is clear that the outcome is largely the same, with the passive particles undergoing non-thermal motion as a result. In this thesis, no such distinction between the origin of the different forces on passive particles is drawn. In later sections the method of extracting 'non-Brownian' trajectory sections is outlined, to capture all such effects.

Chapter 2

Background & Methods

2.1 Introduction

In this section various distinct topics will be introduced and discussed. This is done here to make more succinct the explanations within the main text when discussing the research. The topics will be broken down into sections pertaining to experimental, data analysis, computational and theoretical. To aid in connecting these sections to the main text, in the later chapters the relevant subsections of the background material will be cited explicitly.

2.2 Experimental

2.2.1 Introduction to *Chlamydomonas reinhardtii*

In chapter 3 and 4 two microfluidic experiments are central to our results, in which *Chlamydomonas reinhardii* (CR) are used as the active particles in active-passive mixtures. We will begin by outlining the details of this model organism to help make it clear that they are suitable of use in such experimental systems. CR is a green micro-algae, it is a single-celled biflagellate organism (See figure 2.1). The first description of the species came in 1888 by Dangeard who named them for Ludwin Reinhardt, a botanist from Ukraine [12]. The wild-type strain, cc-125 or 137c, was first isolated by G. M. Smith in 1945 [116] in Massachusetts. The most common research cell lines allegedly originate in the strain Isolated by Smith. CR was the first alga to have its entire genome mapped, highlighting the importance of the organism [117]. The results of this mapping were published in full in 2007 [118]. CR also forms the background strain used to generate many mutants, many of which can be easily ordered from collections from all over the globe. The ease of acquiring the
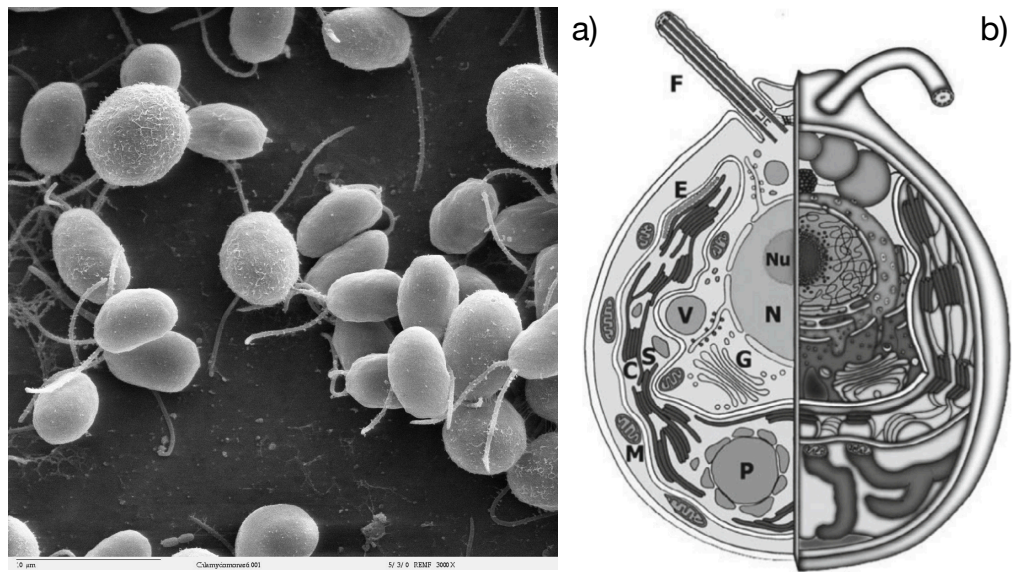
Figure 2.1: **Chlamydomonas reinhardtii** (a) (From Dartmouth Electron Microscope Facility, public domain) Shows a TEM image of a collection of Chlamydomonas, with a faint scale bar for 10μm shown in the bottom left. (b) Taken from [115], shows a chlamydomonas cell, the structures and organelles labelled. F: flagella; E: endoplasmic reticulum; V: vacuole; S: starch granule; C: chloroplast; M: mitochondria; P: pyrenoid; G: Golgi apparatus; N: nucleus; Nu: nucleolus.

various different stains makes the organism straight-forward to begin working with, further reinforced by the ease in maintaining them within a laboratory setting. In a laboratory setting CR are stored within a diurnal chamber. The chamber runs on a day-night cycle, 16 hours of 'day' and 8 hours of 'night'. This cycle keeps the cells in a (vegetative) haploid state (gametes contain the same number of the chromosomes as their offspring). These cells will then reproduce indefinitely asexually producing clone cells. They can also perform sexual reproduction, in which pairs of CR produce non-clone offspring. To do this, the cells must be moved into a medium which has no nitrogen sources. However, for our purposes it was sufficient to allow the cells to reproduce asexually in the diurnal chamber.

A review of CR can be found in [12], however several details of interest will be outlined briefly here. CR's body is roughly 10 micrometers in diameter. Enclosed in the cell wall around the body there are the usual set of eukaryotic cell organelles: vacuoles, smooth/rough reticulum, nucleus, etc. However, as well as these there is a large half-moon shaped chloroplast for photosynthesis, a pyrenoid which aids the availability of CO_2 and an eyespot that enables light sensing [115]. Protruding from the cell body, the two flagella generally measure 10-12 micrometers. These

flagella move in a breast-stoke like motion to enable the motion of the CR, much like the 'flexible oar' example outlined in [7]. The flagella beat at approximately 50Hz, giving an overall speed of the CR around $100\mu\mathrm{ms}^{-1}$ during the run phase of its motion. As previously discussed, it is possible to easily generate mutants of the wild-type, and so these features are somewhat malleable, with some research focusing on mutants that have shorter or longer flagella [119, 120].

2.2.2 Culturing Techniques in *Chlamydomonas reinhardtii*

To perform the experiments outlined in chapters 3 and 4, we must culture and sustain a healthy population of CR to enable them to swim within our experiements. In this section we will detail the main techniques needed to produce a population of suitable swimmers. To store them in a diurnal chamber we make use of the Tris-acetate-phosphate (TAP) medium, which is standard for the culturing of freshwater algae. This medium is sufficient to provide nutrients the cells need for motion and reproduction. The media can be made using the following protocol: [121], to produce liquid TAP. The cells can then be kept short term, requiring daily TAP media substitution or long term, requiring the transference of the cells between old and new solid media gel.

We will first discuss the use of solid media to create stocks of CR. To convert the TAP to a solid gel the following steps must be followed: the TAP must be mixed with 3% W/V agar and 0.4 W/V yeast and then autoclaved. The agar makes the liquid-TAP mixture into a semi-solid gel. The yeast speeds up bacterial growth to aid in identifying contamination. The heated mixture can then be transferred into individual tubes after autoclaving, held in a slanted rack. By filling until the mixture is level with the lower lip of the tube within a slanted rack, it can be cooled within the tube to create a gel surface that the cells can be deposited onto. The cells should be spread in a zig-zag pattern across the surface where possible, this enables easier recovery of the cells in the case of contamination. After the cells have been deposited onto the media, the rack can be transferred into the diurnal chamber where it can be stored for up to six months.

From the solid stocks, liquid cultures can then be produced. Using a sterile inoculation loop, a sample of cells from the solid stocks can be transferred into a small beaker with 25ml of TAP (liquid) media. This beaker can then be put onto a stirrer plate within the diurnal chamber. Over several days the media will change from clear, with the green sediment of the cells, to a pale green colour. This liquid culture is now ready to be used for substitutions.

Cells left too long in liquid media encounter several issues. Some will grow

too large which can impede their ability to swim, at saturation the media can be depleted of nutrients leading to the cells dying out, etc. To avoid these issues, after the cells have reached the pale green state described above, a small sample is transferred each day into fresh media. This process is called substitution. First, the concentration of the cells must be established. Using a sterile serological micropipette a small sample can be taken from the liquid culture. Within this sample the cells should be killed using a small amount of Lugol's iodine and appropriately diluted for easier cell counting. The resulting diluted mixture can be inserted between a haemocytometer and a cover slip, then a microscope can be used to count the total number of cells. A factor for the dilution (~ 10) and the haemocytometer ($\sim 10^4$) enables the calculation of the concentration of liquid culture's CR per ml. The liquid cultures should be brought down to 10^6 cells ml^{-1} using an appropriate dilution of TAP. Expected growth at this concentration should be a factor of $\sim$5-8 overnight each day.

The benefit of keeping cells in long term storage is that liquid (short term) cultures, being frequently interacted with, are more vulnerable to contamination. Long term storage means they can be interacted with minimally, lowering the chances of contamination. Hence, if there is an issue with the liquid cultures, having a ready supply of solid stocks means that the liquid cultures can be readily replaced. However, a liquid culture that has been regularly substituted over several days is needed for the use of the CR cells in experiments. Within swimming experiments liquid cultures CR are generally required, for which the concentration can easily be modified. Maintained in this way liquid culture's cells will swim better, with less cells overgrown or lacking flagella.

2.2.3 Producing Concentrated Swimmer-Colloid Mixtures

Within the mixed system experiments passive particles are implemented. These are colloidal, weakly-Brownian particles. The colloids are polystyrene and can be ordered in desired diameters [122]. We will later see in chapter 3 that the colloids used have a diameter of $10(\pm1)\mu$m. In chapter 4 the colloids are $6(\pm0.6)\mu$m, to enable the boundary to be permeable to the colloids but not the swimmers. The swimmers themselves must be concentrated to create a concentration that is low enough to avoid swimmer-swimmer interactions, while being high enough to maximise the swimmer-colloid interactions which we're interested in capturing. To do this, first we move 1ml from the liquid culture using a sterile micropipette into a 1.5ml Eppendorf tube. This can then be centrifuged at 1000 RPM for 10-15 minutes. The result of this will be a pellet of CR suspended at the bottom of the Eppendorf. At
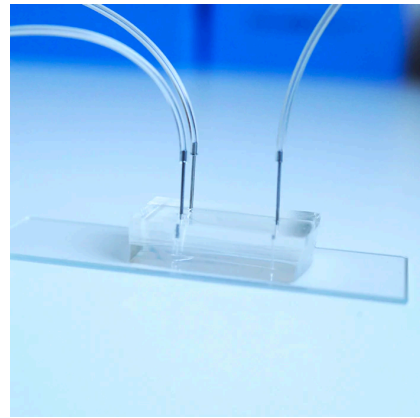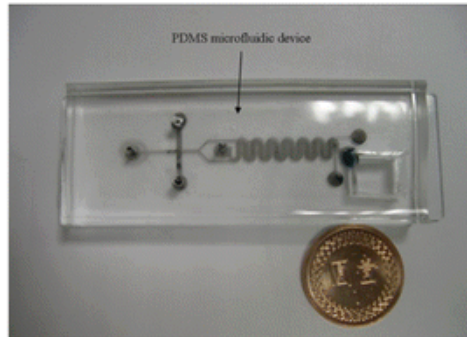
Figure 2.2: **Examples of microfluidic devices** A few examples of microfluidic devices are shown. (Left) A PDMS device, with a coin shown for approximate scale from: [124]. (Right) A PDMS device, bonded with tubing inserted into inlets and outlets from: [125].

this point the liquid supernatant may be removed and then the pellet resuspended in the desired new volume of DI water. The resulting osmotic pressure from the DI water has not been seen to affect the viability of swimming of the CR due to internal water regulating structures [123] At this point the desired quantity of colloids can be added and, keeping track of the volume of the combined mixture, we can estimate the CR concentration. The pellet can be agitated gently to resuspend the CR without damage the cells. The tube should then be returned to the diurnal chamber for ~ 1 hour to allow the cells to recover before being used in experiments.

2.2.4 PDMS Microfluidic Devices

In chapters 3 and 4 the experiments are performed using microfluidic devices. In this section we will detail what these are and how they can be produced in a laboratory setting. Polydimethylsiloxane (PDMS) is a silicon based organic polymer. It is optically clear, reasonably inert and non-toxic. PDMS is also hydrophobic, preventing wetting which makes it a good candidate for containing liquids. Raw PDMS is a viscous liquid initially. However, it can easily be cured by using a cross linker to form a transparent solid. In the following an outline of the key steps will be given for microfluidic device production (for further details see [126]).

To cure liquid PDMS a cross-linking compound is added at a ratio of 10:1. The resulting mixture can be degassed to remove bubbles and then upon heat treatment, over time, it will become an elastic solid. The trick here is that this curing can be performed with the PDMS poured on top of any textured surface. Upon pealing away the cured PDMS, after it has solidified, we are left with a negative of that textured surface stamped into the PDMS using a mould.

Using photolithography, SU-8 photoresist can be conditionally hardened on a substrate (a silicone wafer). It is possible in this way to produce moulds of any reasonable shape to perform this stamping. To do this, with the aid of computer software, a design for the microfluidic chamber can be made and a precise mask produced. This mask is a thin sheet which allows the formation of the negative, where the cavity of the microfluidic is intended to be, to allow columnated UV light to pass through the sheet. First, by using a spin coater, the photoresist coats the substrate to a precise desired thickness. Then using a UV light-source and the mask, the photoresist is induced to cross-link in locations intended to form the textured surface. Finally, a developer compound is used to remove the excess photoresist (non cross-linked). These moulds then act as our textured surface and are used to stamp designs into the PDMS [127, 128].

The cured PDMS is reasonably soft. As such, by using a scalpel it can easily be cut, to aid in its removal from the mould. Using a circular biopsy punch, holes through the device can also be cut, which can later be used as inlets or outlets for fluid flow (See figure 2.2 right). With the device prepared it can now be bonded to a glass cover slip. The bond comes as a result of exposing the surface of both the PDMS and the cover slip to plasma. The plasma leads to oxidation, which in turn causes the addition of silanol groups to both surfaces. When both exposed surfaces come into contact they are able to form strong permanent bonds to each other. This contact must occur somewhat quickly, as the new groups will not persist after the plasma is removed. As a result of this bonding between the glass and the PDMS the cavity is formed. Inlets can then enable liquids, cells, etc. to be inserted into this space (see figure 2.2 left, shown as a grey substance).

2.2.5 Insertion of Prepared Swimmer-Colloid Mixture into Devices

Having produced a concentrated mixture of active and passive particles and produced the relevant microfluidic devices for the experiments, we can now describe the process of insertion used in the experiments detailed in chapters 3 and 4. The devices can be filled using a syringe and if necessary a small amount of tubing. Between removal and re-insertion of any tubing, the inlet and outlet should be left

with a small liquid droplet above, to avoid gas bubble introduction to the cavity. Small gas bubbles, which are present after devices have been filled, drive undesirable flows which can disrupt experimental measurements. Despite the fact that PDMS is impermeable to liquids, owing to its hydrophobic nature, it is gas-permeable. As such, by using the gas-permeability of the PDMS, any bubbles inside the chamber can diffuse out through the PDMS. In general, the method for ensuring there are no bubbles is to seal the outlets (using a paperclip or similar implement), pressurise the chamber and wait for the bubbles to diffuse through the PDMS. Methods of pressurisation include the use of a syringe, held at a constant plunger depth or the removal of the plunger altogether, suspending a filled syringe at height to allow gravitational potential to drive the pressure.

The insertion of both cells and colloids presents the issue of surface adhesion. This leads to the particles getting pinned and no longer moving within the chamber, which can disrupt experiments. To avoid the devices are pre-filled, using a Pluronic-127 5% W/V solution (P-127). This thinly coats the walls within the chamber, thus 'passivating' the surface. The passivated surface will give less particle adhesion of colloids or swimmers through adsorption. However, P-127 is non-biocompatible with microswimmers. To prevent cells being damaged, after filling with P-127 and leaving it to settle for ∼30 minutes to fully ensure the surface is passivated, the P-127 should be thoroughly flushed out using water prior to cell insertion. When the cells are inserted, following the passivation, the outlet and inlet (which as mentioned prior should have a droplet above them to avoid bubbles) need to be blocked. This blocking is used to prevent evaporation which can also drive flows within the device. Blocking can be achieved using semi-solid oils like Vaseline.

2.2.6   Microscopy Techniques

The microscope used in this thesis for imaging was a Zeiss AxioVert 200M inverted microscope [129] with a long-pass filter (cutoff wavelength 765nm) in the optical path. The filter was added to prevent phototactic response from the CR cells in the experiments.

Throughout this thesis, the microscope was used to perform bright-field illumination to image the samples. This is the simplest form of optical microscopy, in its most basic form it can be broken down to a few components. In this form of illumination, white light is produced from a light source (for the Zeiss this comes from a halogen lamp). A condenser lens is used to focus the light onto the sample being imaged, it is this focused light that is filtered using the long-pass filter in this thesis' experiments prior to sample illumination. After the light has then passed
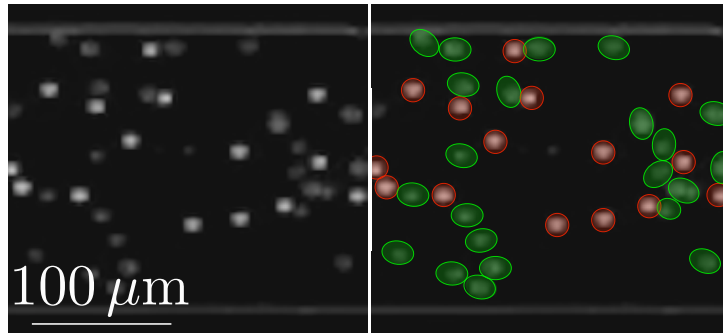
Figure 2.3: Taken from [131]. (Left) Shows an image containing two species of particle, separable by eccentricity and visual intensity. (Right) Shows the Results of the Kilfoil Algorithm, with CR (green) and colloids (red) highlighted.

through the sample, which will modify the light by attenuation, the light is collected by an objective lens, this lens also magnifies the resulting image. Finally, the light passes to the camera where the images of the system can be captured. The camera will then have a physical pixel size. When combined with the magnification from the objective lens the pixel size can be used to calculate the physical size of the sample being imaged.

A complete introduction to the available techniques is given in [130] chapter 12, as well as more details on bright-field microscopy.

2.3 Data Analysis

2.3.1 Digitising Trajectories

During the experiments a series of images are captured. Within the images, we can see both the swimmers and the colloids. Our aim is then to automate the recognition of their positions, which is important to section 3.2.2. In this section, need to measure the positional information for the colloids first to look at the stationary distribution and then to extract information of large 'jump' events. This can be done using a featuring algorithm such as that produced by M. Kilfoil (and various other authors, using alternative programming languages) [132, 133]. The process for positional data extraction will be described and an example of the result is shown in figure 2.3. The first step in this process is to remove pinned artefacts, for example, colloids which have become stuck within the channel and are thus immobile. To do this, we can take an average of all of the collected images, the averaged image can

then be subtracted from each image to remove such stationary artefacts. Following this process, we have within our images a bright background (since nothing blocks the microscope's light from the objective) with dark spots where the cells or colloids are. Using now the expected size, particle eccentricity and, a window of expected maximum and average intensities, we are able to identify and distinguish the species in the image. The recognition was performed first on a test set in our experiments, with the tracking parameters modified to give the best particle recognition. Where possible, they were chosen to maximally rule out false positives, while not giving too many false negative cases. With the positions of all the colloids and the swimmers marked within each of the frames, the next thing is to work out how the frames are related. By considering both a range of possible distances and a number of frames for which the particles can 'disappear', we are able to get the full particle trajectories. Heuristically, for a position at step t a small circle around the position is looked at at time $t+1$ to see if any measured positions are close. Multiple passes are made for increasing circle sizes. Between t and $t+m$ colloids can be detected, where m is the number of frames in the memory. This allows correction for frames in which colloids got false negatives, using colloids stored in the memory (and then re-detected in subsequent frames) to fill in the gaps. Missing steps can be easily corrected for, by interpolating the trajectories during missing steps since the step size is small. For full details of this procedure works see: [133].

2.4 Computational

2.4.1 Important Statistical Processes and Distributions

During the computational portions of the work we will refer extensively to the Poisson process, Poisson distributions and exponential distributions. Specifically, once we extract the jumps from the colloid's measured positional data in section 3.2.3, in section 3.2.4 we will model the colloid's jump process as a Poisson process, the result of which is a jump with an exponentially distributed size. Armed with descriptions of the details of Poisson processes, we go on to implement them throughout section 3.4 for the stationary distribution, 4.4 for the dynamics, and in section 5.3. A brief outline of each will be given here and references provided for further details.

The first process of interest is the Poisson point process. This is a model used for discrete random events where the average rate is fixed, but the exact moment when the events happen is random and independent of the previous. A loose anecdotal example (since in the strictest sense it is untrue in the real world) of this is bus arrival times. Most bus companies will advertise 'every 20 minutes', however,

due to traffic and real world conditions these buses arrival times in fact randomly distributed. As well as this, the next bus driver, who sticks rigidly to his timetable (which sets the process' rate), will not know the previous was late/early. Thus, we see in this case that these events are independent from each other.

For such continuous time Poisson processes, for which the events are independent with a given rate, then the probability of k events occurring before a time t is given by

$$p_p(k;T) = \frac{(\lambda T)^k}{k!} \exp(-\lambda t), \qquad (2.1)$$

where λ is the rate of the process. For such a process, we can also calculate easily the probability of an event occurring at, or before, a given waiting time: τ. To do this we look at the probability that no events occur $p_p(0;\tau)$ and then look at $1 - p_p(0;\tau)$ to give the probability this did *not* happen

$$P_w(\tau) = 1 - p_p(0;\tau) = 1 - \exp(-\lambda \tau). \qquad (2.2)$$

Finally, for Poisson distributions we note, for small τ we can make the following approximation, expanding the exponential, with terms of order τ^2 negligible we get

$$P_w(\tau) = \lambda \tau. \qquad (2.3)$$

The next type of distribution is the exponential distribution. This process is generally also associated to the time it takes for events to occur. A real world example could be nuclear decay or the subsequent production failed product on a factory's production line. In this case the probability density of a given event is

$$p_e(t) = \frac{1}{\ell} \exp\left(-\frac{x}{\ell}\right). \qquad (2.4)$$

Importantly, the average value $\langle x \rangle$ is given by ℓ. Notice, that $P_w(\tau)$ with $\lambda = \frac{1}{\ell}$ is the associated cumulative distribution function of (2.4). The reason for this is because the lengths of the wait times in a Poisson process are exponential distributed.

2.4.2 Acceptance-Rejection Schemes and Inverse Sampling

In section 3.3 we will detail a numerical model in which experimentally measured of dynamical property's distributions are re-sampled, in an attempt to replicate the stationary distribution. To do this we need to implement, an acceptance-rejection (AR) scheme, a numerical method used to generate discrete sample events which

follow a given distribution. The idea is as follows, a uniformly distributed number is selected, a portion of this interval designated as 'accept' according to a distribution and the remainder is 'reject'.

To use the example of (2.3), which gives the probability of a Poisson process generating an event between $t = 0$ and $t = \tau$ for a small τ. Here, to use acceptance-rejection we need a subset of the interval [0,1] of width $\lambda\tau$ (corresponding to the probability from (2.3)): $\Lambda = [\frac{1-\lambda\tau}{2}, \frac{1+\lambda\tau}{2}]$ is such an interval. So, if a uniformly distributed random variable (which is generated at each time-step for comparison) is within this interval Λ, it constitutes an acceptance, while if it's in the complement of this interval then it is a rejection. The result of which will be a sequence of 'accept' or 'reject', and the acceptances will be Poisson distributed with a rate λ.

Inverse transform sampling is a method of generating a series of samples which are distributed according to a known distribution. However, rather than getting a binary (discrete) value as was the case for AR, we hope to generate a continuous value at each step. If we have a random variable X which has an associated cumulative distribution function F_X, then we may construct a new random variable: $Y = F_X(X)$, and this new random variable will now be uniformly distributed on [0,1]. If an inverse of the cumulative distribution can be formed, then we get: $F_X^{-1}(Y) = F_X^{-1}(F_X(X)) = X$. So we see that the values of $F_X^{-1}(Y)$ for a Y which is uniformly distributed on [0,1] will itself have the same distribution as X. This process can be used for a distribution measured from experimental data by using interpolation methods (for example spline [134]), allowing arbitrary distributions to be sampled.

2.4.3 Milstein's Method

In section 4.4, we describe a simulation that replicates the dynamical properties of passive particles under the influence of active particles in the presence of a selectively permeable membrane. To do this, we implement drift and diffusivity which positional dependence and so we need to use tools that account for this inhomogeneous system. Milstein's Method is a way to approximate the solutions for certain stochastic differential equations (SDEs), which have both positionally dependent drift and diffusion. We consider the following SDE,

$$dX_t = a(X_t)dt + b(X_t)dW_t, \tag{2.5}$$

where X_t represents the position at a time t, $a(X_t)$ captures the magnitude of a spatially dependent drift, dt is an infinitesimal time interval, $b(X_t)$ gives the spatially

dependent diffusivity size, W_t is a Wiener process [135] with $\Delta W_t = W_{t+1} - W_t$. What this means is that W_t has increments which are normally distributed, that is $W_t = W_t - W_0 \ N(0,t)$, with 0 mean and a variance t.

For such an equation, the following recursive relation can be used as an approximation to the solution,

$$X_{n+1}^m = X_n^m + a(X_n^m)\Delta t + b(X_n^m)\Delta W_n + \frac{1}{2}b(X_t^m)b'(X_t^m)\left((\Delta W_n)^2 - \alpha\Delta t\right). \quad (2.6)$$

Here, X_n^m is the Milstein approximation to the true solution, where the nth time step is $t_n = n\Delta t$ within an interval of total length T. It follows from this that $\Delta t = \frac{T}{N}$ and for $N \to \infty$ the approximation will converge to the true solution [136, 137]. There are two key features here to note. Firstly, the presence of the b' contribution on the right hand side of (2.6), which is in effect another contributing drift, due to gradients in the diffusivity. Secondly, the term α, which codifies the integration scheme which is being used, $\alpha = 0$ being the Stratonovich scheme, and $\alpha = 1$ being the Itô scheme [136].

2.4.4 Weeks-Chandler-Andersen Forces

In chapter 5, we will implement a model of active particles interacting with passive particles. Unlike in previous simulations, where there is no interactions between colloids and swimmer-colloid is captured by implementing a coloured noise, this time the simulation captures this inter-particle interaction explicitly. So, we need to introduce a force particle in contact with each other experience. The Weeks-Chandler-Andersen (WCA) potential is a modification of the Lennard-Jones (LJ) potential [138]. It can be used to model the potential between two objects which is repulsive at short distances and non-interacting (zero) otherwise. LJ is repulsive at short distances, but instead becomes attractive further away. To counter this, WCA shifts the LJ potential to ensure it is always purely repulsive (or attractive) and ensures that it remains 0 above this point. The form of the two are as follows:

$$\Phi_{WCA}(r) = \begin{cases} \Phi_{LJ}(r) + \epsilon & \text{if} \quad r \leq 2^{\frac{1}{6}}\sigma \\ 0 & \text{if} \quad r \geq 2^{\frac{1}{6}}\sigma \end{cases}, \quad (2.7)$$

$$\Phi_{LJ}(r) = 4\epsilon\left[\left(\frac{\sigma}{r}\right)^{12} - \left(\frac{\sigma}{r}\right)^{6}\right]. \quad (2.8)$$

Here, r is the separation between the two interacting objects which are being considered, ϵ is the depth of the attractive well for the Lennard-Jones potential, σ the constant which sets the separation at which the objects feel neither attraction or repulsion. The second case within (2.7) is exactly the separation where the LJ potential is at a minima and so there is no force, by setting the potential to be 0 beyond this point. This ensures beyond a threshold distance the objects continue to be non-interacting. Conversely, beyond this point in (2.8) we see the 6th power term overcomes the repulsion from the 12th power term, hence we get attraction.

With this in place, we are now able to discuss the forces that result from such a potential. Using $F_r = -\nabla_r \Phi$, given our expression Φ for the potential, for $r \leq 2^{1/6}\sigma$ we have

$$F = -24\epsilon\sigma^6 \left[\frac{r^6 - 2\sigma^6}{r^{13}} \right]. \tag{2.9}$$

Notice, here the nominator inside the square brackets is always negative, since this expression is only valid for $r < 2^{\frac{1}{6}}\sigma$, otherwise the force is zero. As a result of this, we can see that the resulting force from the interaction always has a positive sign, and so the objects are pushed from each other.

These results can easily be generalised to a pair which exists in a two-dimensional space (or more) by noting $r = \sqrt{(x_2 - x_1)^2 + (y_2 - y_1)^2}$ for particles at (x_1, y_1) and (x_2, y_2). Using $x = x_2 - x_1$ and $y = y_2 - y_1$, then taking instead: $F_x = -\nabla_x \Phi$ and $F_y = -\nabla_y \Phi$, we are able to construct component-wise the forces. The result of which is that

$$F_{x_i} = -\frac{\partial \Phi}{\partial r}\frac{\partial r}{\partial x_i} = -24\epsilon\sigma^6 \left[\frac{r^6 - 2\sigma^6}{r^{13}} \right] \frac{x_i}{r}, \tag{2.10}$$

where x_i can be either the x or y directions.

Another generalisation which can be easily made is the extension to calculating torques. This time, we consider particles placed at (x_1, y_1) and $(x_2 + a\cos(\theta), y_2 + a\sin(\theta))$, this means that now our distance equation is modified to give

$$r = \sqrt{(x_2 + a\cos(\theta) - x_1)^2 + (y_2 + a\sin(\theta) - y_1)^2}. \tag{2.11}$$

From this result, by using the chain rule we can get the force due to orientational changes of the form

$$F_\theta = -24\epsilon\sigma^6 \left[\frac{r^6 - 2\sigma^6}{r^{13}} \right] \frac{a(y\cos(t) - x\sin(t))}{r}. \tag{2.12}$$

Here, x and y are defined as: $x = x_2 + a\cos(\theta) - x_1$ and $y = y_2 + a\sin(\theta) - y_1$.

2.4.5 Numerical Solutions for Stochastic Systems

When modelling the particles in chapter 5, since we now explicitly include the particle-particle interactions through the WCA potential, we introduce the possibility of large moves due to numerical errors. To avoid this, the simulation's time-step must be decreased. However, as we will describe in this section by implementing higher-order numerical schemes, we can also prevent these numerical errors at a larger time steps. The most basic numerical scheme available for the solution of differential equations is the Forward-Euler (FE) method [139]. If we are given an initial value problem: $dy/dt = F(y,t)$ and $y(0) = y_0$, where $y(t)$ is the desired function. Then for a fixed small value h we can write the iterative equation

$$y(t + h) = y(t) + hF(y(t), t) + O(h^2). \tag{2.13}$$

Here, $O(h^2)$ is the local truncation error, the error associated to each individual iterative step. This value scales as the square of the time-step h and it's value added up over the solution as the iteration is used to find $y(t)$ for all the various values of t. Once the value of this error is summed over the course of the solution we get the global truncation error, which in the case of Forward-Euler is $O(h)$. What this means practically: If we perform two numerical solutions with h_1 and h_2, where $h_1 = 2h_2$. The comparative error we should expect for the h_2 simulation will be half that of the h_1 solution.

Next, we generalise this solution scheme to a stochastic differential equation (SDE). In this case we have that

$$dX_t = a(X_t)dt + b(X_t)dW_t. \tag{2.14}$$

Here X_t has conventionally replaced $y(t)$, a and b are positionally dependent functions which determine the relative contribution sizes of each of the terms and, dW_t is an infinitesimal increment in a Weiner Process $W(t)$ defined as: $dW_t = W(t + dt) - W(t)$. Notice, this equation is an analog to the initial value problem, so if we have $X(0) = X_0$ and choose a fixed time-step δt then we can write iteratively

$$X_{t+\delta t} \approx X_t + a(X_t)\delta t + b(X_t)\delta W_t. \tag{2.15}$$

Notice this is an equation of similar form of (2.13). This solution is called the Euler-Muruyama (EM) scheme [139]. However, this time we have a system with a global

truncation error $O(dt^{\frac{1}{2}})$. As such, we require relatively a much larger reduction in the time-step to achieve equal improvements in the solution's error.

To improve upon the associated error, one can use higher order numerical schemes. One such example of this is the Runge-Kutta (RK) scheme [139], which is an implicit-explicit method. To explain what this means we will outline qualitatively how this numerical scheme works for second-order. First, as with the previous schemes, for a given time-step we know the current state of the system. Using the information encoded in the differential equation to be solved we can construct the solution a small time ahead (as indeed we did in FE). This information is explicit since we only use information from time t to calculate it. At this point the scheme diverges; we retain this newly calculated position and from this position calculate another time-step forward into the future. This two-steps ahead position is known implicitly, since we have used position from $t + \delta t$ to calculate it. Written as a rough equation we then have $y(t + 2\delta t) = y(t) + \delta y_1 + \delta y_2$. However, this is not the position we implement in our solution, instead we use: $y(t + \delta t) = y(t) + \frac{1}{2}(\delta y_1 + \delta y_2)$. Here, we have used an average of the implicitly calculated and explicitly to give a position which factors for both. In this case we get a resulting global truncation error of $O(\delta t^2)$.

Much like for the FE which can be converted into the EM for SDEs, the same is true of RK schemes; the name of the solution for the more general class of differential equations remains RK in the literature (SRK will refer to the stochastic variant). As with EM when compared to FE, there is a reduction of the order of the global truncation error due to the stochastic terms. In the case of second order SKR we get a global truncation error $O(\delta t)$ [140, 141].

2.5 Theoretical

2.5.1 Kramers-Moyal Expansion

In section 3.4, building from a Langevin equation we derive an integro-differential master equation, the solution of which describes the probability distribution of passive particles under the influence of coloured noise. This master equation proves intractable to solve and requires the use of a Kramers-Moyal expansion to proceed. In this section, we will derive how the master equation of a distribution can be written in terms of the moments of a conditional probability distribution function, which relates to how the distribution evolves in time. If we can do this, and we know these moments, then we can get the master equation. This full master equation written in terms of the sum of all of the moments is called the Kramers-Moyal expansion of

the distribution [142, 143].

First, a distribution function $P(x,t)$ is a function describing the probability of finding a particle in the positional range $(x, x+dx)$ at a given time t. In stochastic systems such functions can provide important information about their properties. In general, for time dependent system we can write

$$P(x, t+\tau) = \int w(x, t+\tau|x', t)P(x', t)dx'. \tag{2.16}$$

This is because, all particles at $(x, t+\tau)$ must have arrived there from somewhere, by moving from various other positions (x', t). At time t, $P(x', t)$ can be interpreted as the total proportion of particle at (x', t) and by calculating the product $w(x, t+\tau|x', t)P(x', t)$ we can work out what proportion of the particles that started at (x', t) ended up at $(x, t+\tau)$. Finally, by integrating over all the possible values of x' (including x'=x), we can work out the portion of particles that are at $(x, t+\tau)$ after this transition has occurred. We assume then that all of the moments of the conditional probability distribution function are known, then

$$M^{(N)}(x', t, \tau) = \int (x-x')^n w(x, t+\tau|x', t)dx. \tag{2.17}$$

We can then write the conditional probability distribution function

$$w(x, t+\tau|x', t) = \int \delta(y-x)w(y, t+\tau|x', t)dy. \tag{2.18}$$

Where $\delta(y-x)$ is the delta function. We can then use an expansion of the delta function, with a slight modification of the derivative to give

$$\delta(y-x) = \delta(x'-x+y-x') = \sum_{n=0}^{\infty} \frac{(y-x')^n}{n!} \left(\frac{\partial}{\partial x'}\right)^n \delta(x'-x)$$

$$= \sum_{n=0}^{\infty} \frac{(y-x')^n}{n!} \left(-\frac{\partial}{\partial x}\right)^n \delta(x'-x). \tag{2.19}$$

Here, we have used the fact that $\partial/\partial x' f(x-x') = -\partial/\partial x f(x-x')$. This can be seen by setting $x-x' = y$, on taking the derivative with respect to x' we get $\partial/\partial x' f(y) = \partial f(y)/\partial y \; \partial y/\partial x' = -\partial f(y)/\partial y$. By considering $\partial/\partial x f(y)$ we get the desired result. Putting all this back into equation (2.18) then we have

$$w(x, t+\tau|x', t) = \sum_{n=0}^{\infty} \frac{1}{n!} \left(-\frac{\partial}{\partial x}\right)^n \int dy (y-x')^n w(y, t+\tau|x', t)\delta(x'-x)$$

$$= \left[1 + \sum_{n=1}^{\infty} \frac{1}{n!} \left(-\frac{\partial}{\partial x}\right)^n M^{(n)}(x', t, \tau)\right]\delta(x'-x). \quad (2.20)$$

By substituting this into equation (2.16) and rearranging then we can write

$$P(x, t+\tau) - P(x, t) = \sum_{n=1}^{\infty} \left(-\frac{\partial}{\partial x}\right)^n \left[\frac{M^{(n)}(x', t, \tau)}{n!}\right]P(x, t). \quad (2.21)$$

By dividing both sides of this equation by τ and taking a limit of $\tau \to 0$ then we get the equation of motion in the Kramers-Moyal expansion form

$$\frac{\partial P(x, t)}{\partial t} = \sum_{n=1}^{\infty} \left(-\frac{\partial}{\partial x}\right)^n \left[D^{(n)}(x, t)P(x, t)\right]. \quad (2.22)$$

Where $D^{(n)}(x, t) = \frac{1}{n!}\lim_{\tau \to 0} \frac{1}{\tau} M^{(n)}(x, t, \tau)$ are the Kramers-Moyal coefficients.

The coefficients are subject then to Pawula's theorem [143]. What this tells us is that there are only three such forms of this expansion. The first case is that $D^{(n)}$ vanishes for all $n > 1$ in which case the equation of motion is deterministic and the motion consists only of a drift. Secondly, $D^{(n)}$ vanishes for $n > 2$, this gives us the Fokker-Plank equation and the motion is made up of both a drift and a diffusion. Finally, we can have that the expansion contains all terms. In this last case any truncation of the expansion for a finite order higher than $n = 2$ will lead to a non-positive $P(x, t)$, which of course is non-physical. We will see in section 3.2 that the jumps in colloid trajectory constitute a non-zero second moment. Thus, in section 3.4 we are either in the case which requires two moments or infinitely many, and we shall see it is sufficient to consider the first two moments to reproduce the experimental positional dependence.

2.5.2 The Narrow Escape Problem

The narrow escape problem is a famous problem, the statement of which is as follows. We consider a system with a particle moving around within a container. The container then has two distinct types of boundary. The first type is reflective, if the particle reaches this boundary type it bounces off and then continues moving. The second type is absorbing, if the particle reaches this then it is absorbed and

thus removed from the system. For such a system, given a prescribed type of motion (classically this is Brownian), we can then calculate the expected amount of time a particle will take to be absorbed at the boundary. This is exactly the situation we find ourselves in, in chapter 4. Up to this point, our simulations implement a coloured noise. However, we see in section 3.4, we can also model this system as an effective drift diffusion equation. In this section, we will look how such a system can be modelled.

For a two-dimensional disk of radius R and one absorbing 'exit' on the boundary corresponding to $|\theta| < \epsilon$, where the particle's coordinates are given in polar coordinates by (r, θ), the equations needed to work out the mean first passage time of a Brownian particle to the absorbing portion are

$$\nabla^2 t(r, \theta) = -D^{-1} \quad |r| < 1, \quad -\pi \leq \theta < \pi,$$
$$\frac{\partial t(r, \theta)}{\partial r}\bigg|_{r=1} = 0 \quad |\theta| > \epsilon,$$
$$t(r, \theta)_{r=1} = 0 \quad |\theta| < \epsilon. \tag{2.23}$$

Here, $t(r, \theta)$ is the expected time to be absorbed given an initial condition of (r, θ) and D is the diffusivity associated to the Brownian motion of the particle. The second line codifies the reflecting boundary condition (since there is no flux through the boundaries) and the third line the absorbing, since particle which begins at such positions instantly is absorbed [144, 145]. This is in effect a Poisson equation with mixed inhomogeneous boundary conditions. A one-dimensional derivation of which is given in [145] and also some direction towards inclusion of drift by analog to electrostatic boundary-value problems.

Although, as we see in [144] some of these problems can be solved analytically, due to the large number of small exits (the result of which is a relatively large boundary portion associated to absorption) these calculations will turn out to be unhelpful and thus are omitted here. The chief take away from section is that for such systems we have equations (2.23), which can be solved numerically for a given constant diffusivity and prescribed geometry. However, we will see for this system the numerical solution does not give a good prediction of the dynamics of escape we measure in the experiments and that inclusion of particle drifts are needed to reproduce the measurements.

Chapter 3

Active-Driven Dynamics of Colloids in Confinement

3.1 Introduction

We begin by introducing a set of experiments in which a mixture of active and passive particles are introduced into a straight pseudo-two dimensional microfludic channel together. It has been established that many microswimmers, in the presence of boundaries, will tend to accumulate near them to varying degrees [29]. In [146], a system of interacting self propelled particles was studied using numerical simulations within straight channels subject to a variety of flows. In this study it was clearly demonstrated that particle aggregation near to the boundaries occurs. Indeed, we see in our dilute system this accumulation manifests as a time-averaged effect; partial accumulation near the boundary, with swimmers occasionally leaving and re-enter this region. As a result of this, there is an inhomogeneous distribution of swimmers close to any surface. If we measure the swimmer distribution over a long period of time, we see a non-uniform distribution. Since the swimmers continuously consume different energy forms within their environment, they are able to sustain a non-equilibrium distribution. Despite this the distribution is found to be stationary, with a consistent time averaged shape. The shape of any confining chamber that swimmers are placed into, in an experimental context, is if course entirely controllable. This is because we can design a microfludic device to be of any shape, by doing so altering the swimmer distribution shape. Hence, if we understand the relationship between the shape of such chambers and the resulting inhomogeneous distribution of swimmers, then in theory by tuning the confining geometry, desirable swimmer distributions can be produced. In experimental systems it is well

known that wall scattering dominates the boundary interactions [147, 151], where it's noted that flagella contact in the vicinity of boundaries leads to a distribution of exit angles. Using this scattering idea, and by modifying the confining boundary's curvature that the cells experience, experiments have been designed to use this curvature to guide the swimmer's motion [148]. The results of which is further explored in [149], where experiments using CR and simulations are used to show that by considering the curvature in general confining geometries, the active fluxes that are generated by the motion of the CR can be calculated. In this chapter we will build on this idea. Considering the the swimmers as active bath, which thanks the the chamber geometry will have spatially dependent properties. As a result of these properties we will see that a non-uniform distribution of swimmers results in a straight channel, replicating what has been seen in previous work [146]. We will see how this swimmer distribution impacts the behaviour of passive colloids by measuring their positional distribution and their dynamics.

3.2 Microfluidic Straight Channel Experiments

In this section we will briefly introduce the experiments performed and explain the design choices of the system being studied.

3.2.1 Experimental Design

By utilising CR and similarly sized ($\sim 10\mu$m) polystyrene colloidal particles we can, using microfludics, explore this inhomogeneous swimmer distribution's effect on passive colloidal particles. In sections 2.2.1-2.2.5 an outline of the various experimental protocols and some further references for a more comprehensive description are given. The simplest confining chamber geometry available is a pseudo-two-dimensional straight channel, bound by two walls. The channel's height is designed to be comparable in size to the diameter of a CR cell. Another key benefit to the pseudo two-dimensional channel design, we have a system of colloids and swimmers that all lie in one focal plane. Within the experiments, bright-field microscopy (see section 2.2.6 for details) was used to acquire images. As noted in 1.6, the previous work on this subject has seen a split in focus for active-displacements. Hydrodynamic effects on one side, looking at the effect that the flow generated by the swimmer affects the passive particles. Steric events, on the other, in which contact between the particles plays the major role. In this work we have not distinguished these types of event, instead focusing on 'large' events, without focusing on what interaction type originates them. By having the colloids and swimmers be constantly
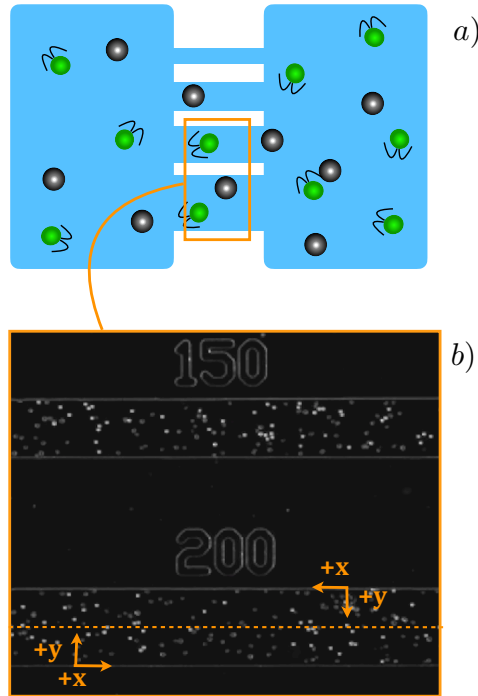
Figure 3.1: **Schematic of the straight channel microfluidic** (A) Schematic showing the geometry of the microfluidic channels, with lengths exaggerated for clarity. Swimmers are shown as green circles with two flagella, the colloids as black circles. We see the different channel widths between the two reservoirs. (B) Experimental image of the channels taken away from the reservoirs.

in focus and using a high frame rate, all such large events can be tracked in their entirety.

Within the straight channel's confinement it is clear that there are two principle directions. These being perpendicular to the boundary and parallel. As we study the dynamics of the colloids, it will become clear that it is in fact the perpendicular direction which contains the most dynamical inhomogeneity.

As well as this, we will compare channels of different widths. Far away from any of the boundaries, we should expect that the behaviour of the system will return to a 'bulk' behaviour. By looking at the different channel widths, we are able to assess whether or not any difference in behaviours, that result from the boundaries, can be boiled down to purely the distance from it. In effect, if this can be shown to be the case then we have reduced the passive dynamics dimensionality from a two-dimensional problem, to a one-dimensional. Since then all we need to know is the distance to the nearest boundary to predict the behaviour.
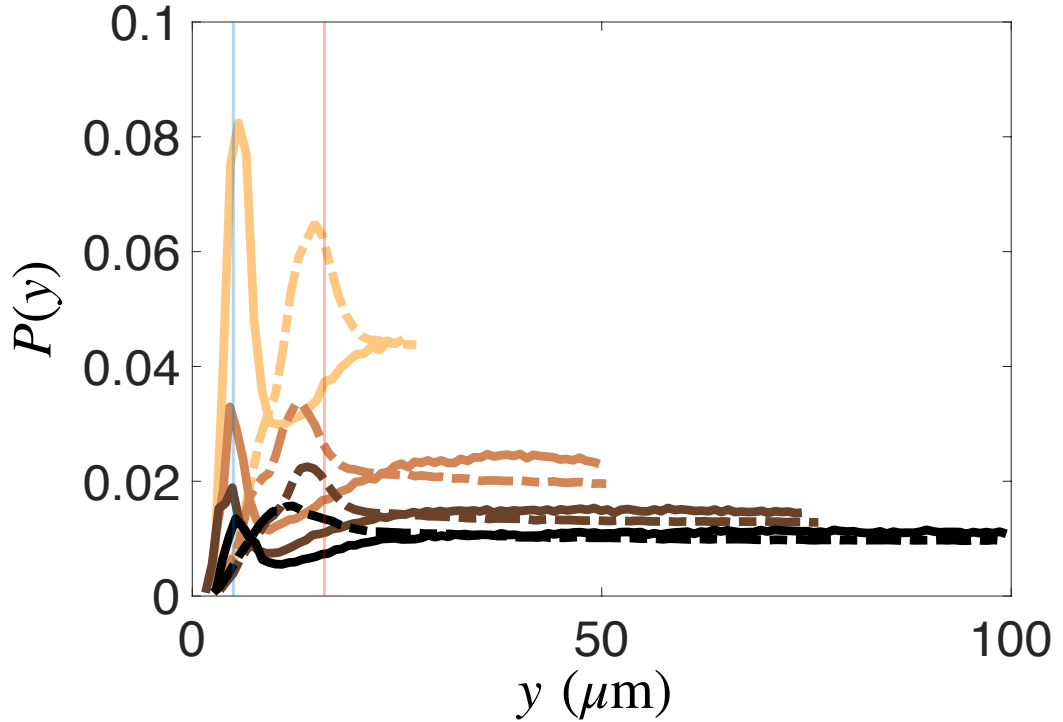
Figure 3.2: **Stationary distribution of colloids and swimmers** Figuring showing the relative probability of finding colloids (solid line) and swimmers (dotted line) at given distances y measured in micron from the closest boundary. Four different channel widths are indicated using the following colours: 50um (yellow), 100um (orange), 150um (brown), 200um (black). Two faint lines are used to indicate two key lengths, (blue) indicates the distance of one colloid radius (5μm) from the boundary and (red) shows the sum of a colloid diameter and a swimmer radius (16μm).

The microfluidic channels are positioned between two large reservoirs, which themselves are connected to the inlet and the outlet, to allow for easy insertions of mixtures. The reservoirs serve to maintain the concentration of CR and colloids in the thin channels between them, and by imaging close to the centres of these thin channels we are able to neglect the effects of the reservoirs. The concentration of swimmers and colloids is reasonably dilute. This ensures that any collective effects of both species can be neglected.

3.2.2 Stationary Distributions of Colloids and Swimmers

The data from the microfluidic experiments described above is in the form of a time lapse of 80,000 images taken at 10 frames per second. The images show the positions

of the colloids and swimmers over the duration of the experiment. From the images digital trajectories for each particle can then be produced (in the section 2.3.1 details are given on this tracking process), with the positions of the centres of the colloids and swimmers at each time-step measured. From this positional data we can get the positional probability density function (PDF) as a function of distance from the nearest boundary. By choosing to use the distance to the nearest boundary as the principle measurement, this allows us to symmetrise the data around the centreline of the channels, effectively doubling the overall data. This PDF can be seen in figure 3.2.4, where we see the colloid distributions represented by a solid line and the swimmer distribution in dashed. Each of the channel widths tested in the experiments is shown in a different colour. In both species, the curves show non-monotonic behaviour.

Starting first with the curves for the swimmers; there is a clear peak in the positional distribution for all widths at $\sim 15\mu$m from the boundary ($y = 0$), roughly the sum of the CR radius and either a colloid diameter or a flagella. It has been shown previously that flagella interactions dominate the near boundary behaviour of CR [147], as as a result this causes a peak due to the extra time swimmer spend at this distance from the boundary scattering. However, this result is also likely exacerbated by the presence of the colloids which, due to their accumulation, could also be acting as a partial boundary. On either side of this swimmer PDF peak we see a decrease on the boundary side decreasing to 0. While inside the channel the distribution decreases to a constant value. This tells us that far enough away from the boundary we expect that the swimmers will distribute uniformly and recover their 'bulk' behaviour. Since there is a fixed distance from the boundary in which the swimmers feel the effects of the boundary. For the smaller channel widths, this boundary area makes up a larger portion of the overall channel, so we see that the effect is larger in these cases.

The colloids, similarly, have a distributional peak near to the boundary. However, this time the peak is present $5.9 \pm 1.5\mu$m, comparable to the particle radius which is indicated in figure 3.2.4 with a faint blue line. Between $10 - 20\mu$m we then have a depleted region. This depletion is in the vicinity of, but not exactly aligned with, the swimmer's distributional peak, suggesting that this is perhaps not merely an exclusions effect. As we will come to see, when we study the dynamics of the colloid motion near the boundary, it turns out that this effect is due to an asymmetry between motion of the colloid toward and away from the boundary in this area. As a result there is an excess of colloids which are pushed toward the boundary. Following this depletion region there is a recovery to the bulk value, as we
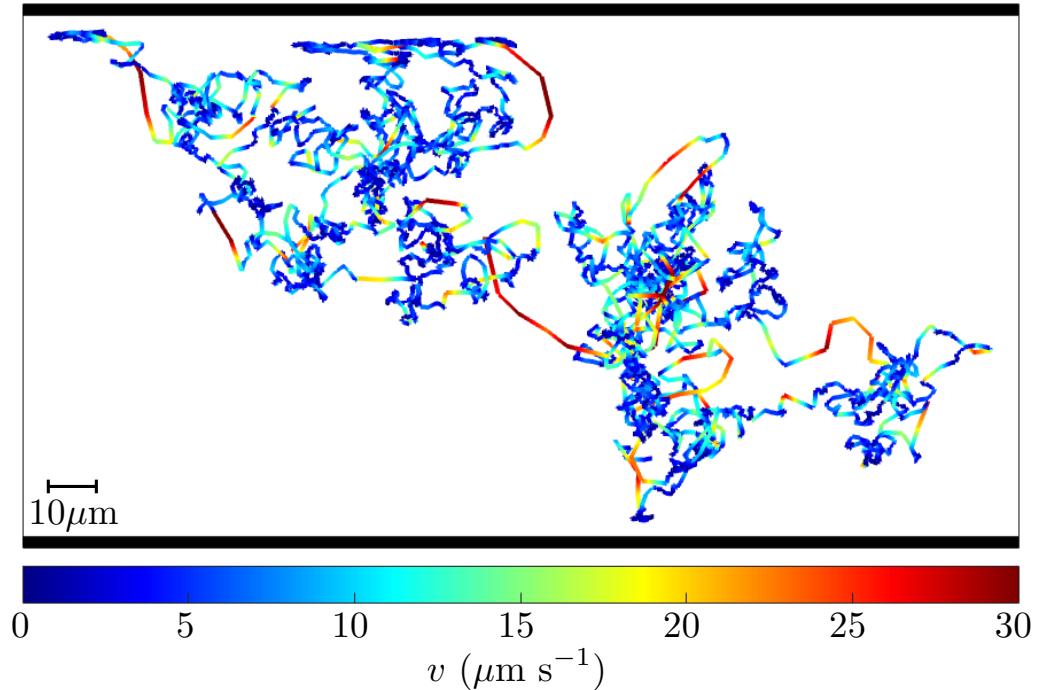
Figure 3.3: **Example trajectory colourised by local speed** Figure showing a single example trajectory of a colloid tracked in the experiments. The colour showing the local velocity of the colloid as it moves along the trajectory: values of which are given in the colour-bar in μs^{-1}. Boundaries within the system are shown at the top and bottom by thick black lines. A $10\mu m$ scale bar given.

saw with the swimmers. As with the swimmers, this peak, depletion and recovery is present for all the channel widths in the experiments.

3.2.3 Extracting Colloid Jumps from Positional Data

In 1.6 we highlighted the various methods in which large displacements can come about for colloids, due to swimmers. These can be either hydrodynamic or steric. However, in both cases these large displacements have hallmark features that enable us to distinguish them from Brownian motion within the trajectories. In figure 3.3 we see an example trajectory of a colloid colourised by the local velocity along the trajectory. For the most part the motion can clearly be distinguished into two distinct types; (blue/green) slow diffusive motion and (yellow/red) fast 'jump'-like ballistic motion. Based on previous works, [150, 46], we postulate that the overall positional PDF largely depends on these fast jump events, which can be

distinguished by noting that the local velocity during the jump events and the directional correlation behaviours are very different to what they undergo during Brownian motion. As such, we will isolate these portions of the trajectory and characterise the dynamics to see if indeed the jumps do dictate the behaviour of the stationary state.

In order to recognise the jump events within positional trajectories, we use a hybrid method, similar to both [150, 46], but with some slight modifications. The process follows first the method of [150], using directional correlation between subsequent particle displacements to identify candidate periods of non-Brownian displacement. Subsequently, as in [46], the individual displacements during these periods are evaluated to ensure that their constituent steps are sufficiently large, verifying them as non-Brownian in origin.

To look for the directionally correlated windows we start by defining the displacements $\Delta\mathbf{r}(t) = \mathbf{r}(t + \Delta t) - \mathbf{r}(t)$, where $\mathbf{r}(t)$ is the colloid position at time t. With these we calculate the scalar product $p_{\Delta t}(t) = \Delta\mathbf{r}(t + \Delta t) \cdot \Delta\mathbf{r}(t)$. In the Brownian case $\langle p_{\Delta t}(t)\rangle = 0$ with a standard deviation given by $q_c = \sqrt{8}D_0\Delta t$. For a diffusivity $D_0 = 0.0439\,\mu\mathrm{m}^2/\mathrm{s}$ (the thermal diffusivity for a $5\,\mu\mathrm{m}$ radius at $300\,\mathrm{K}$ in bulk water found using the Stokes-Einstein relation) and a time between frames $\Delta t = 0.1\,\mathrm{s}$, we have $q_c = 0.0124\,\mu\mathrm{m}^2$. Notice that, due to hydrodynamic interactions between colloids and boundaries, D_0 over-estimates the thermal diffusivity of the colloids in our experiments. This makes the threshold for classification of active jumps more stringent. From this we compute $q_{\Delta t}(t) = (p_{\Delta t}(t + \Delta t) + p_{\Delta t}(t))/2$, and use $4q_c$ as a threshold to select sections of a colloids' trajectory which are sufficiently directionally correlated, and which could therefore be non-Brownian in origin. Finally, we confirm that each of these potential jumps (consecutive time steps where $q_{\Delta t}(t)$ is above the threshold) has individual constituent displacements which are sufficiently large to rule out correlated Brownian motions. To do this, we calculate for these trajectories the displacement magnitudes $|\Delta\mathbf{r}(t)| = |\mathbf{r}(t+1) - \mathbf{r}(t)|$, we can then compare these values to the Brownian expectation $\sqrt{4D_0\Delta t} = 0.132\,\mu\mathrm{m}$. For a candidate jump trajectory, requiring that at least 70% of the individual displacements within it are larger than the Brownian prediction for the overall jump to be confirmed. This percentage strikes a balance between being over-selective, losing a large portion of actual jumps, and under-selective, mis-classifying non-jump events as jumps.
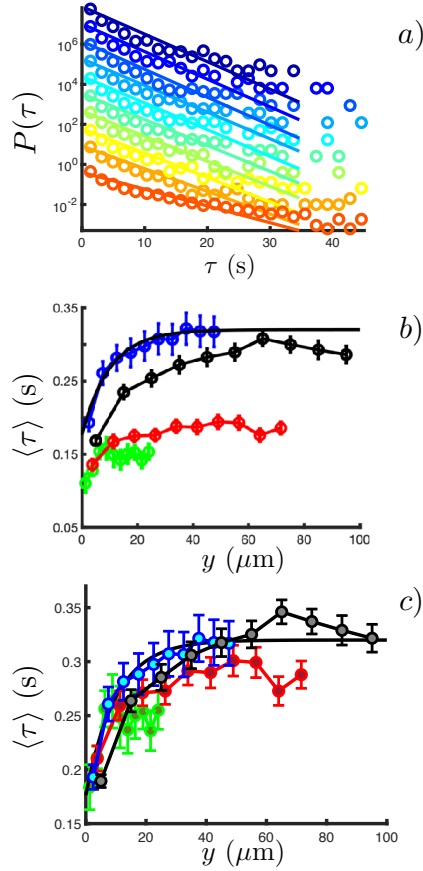
Figure 3.4: **Colloidal jump wait time dynamics** (a) Shows a semi-log probability distribution plot of a given wait time (τ) for the 50μm channel width experiment. Here, the colours show distance from the boundary with red at the boundary and blue in the bulk. Single rate Poissonian fits are shown as a solid line. (b) Shows the average wait time measured as a function of distance to the boundary. The colours represent 50μm (green), 100μm (blue), 150μm (red) and, 200μm (black) channel widths. A fit is given in solid black for the 100μm. (c) As with (b), the average wait time is shown. Each curve in (c) has been scaled by their concentration relative to that of the 100μm channel's.

3.2.4 Space-dependent Properties of Colloid Jumps

The first question that must be addressed to characterise the jump dynamics is the following: For a given colloid, at some distance from the boundary, how long should it be expected to wait before a jump will occur?

Since we can distinguish jumps from within a trajectory it is possible to measure this. We can look at the time at which the jump n ends and compare this to the time at which jump $(n+1)$ starts, the difference in which we call the wait time.

43

Along each of the colloid's individual trajectories we are able to construct these wait times. Further, we associate these wait times to the position at which jump n ends to give the waits themselves positions. Here, we are implicitly assuming, since the diffusivity of the colloids is relatively low, they don't move far from this point. Thus this is the point at which the waiting was done. By binning all of the wait times by the distance of the position where the colloid waited from the boundary, it is possible to construct the PDF of colloid wait times within these uniformly sized bins. This distribution can be seen in figure 3.4(a), for the case of the 50μm width channel, where the circular markers show the experimentally measured distribution. Within this plot we can see different distances from the boundary represented by the colour of the markers, with red markers near the boundary and blue markers in the bulk. Noting this plot is in semi-log scale then we can see two straight line gradients for each of the curves, depending at which part of the curve we look at. There is a steeper straight line for early wait times and then a shallower line for the longer wait times. The earlier value gradient is suspected to be due to repeated interactions of the colloid with the same swimmer. Some swimmers observed in the experimental time-lapse had a tendency to interact with a colloid, pass it and then turn back. Despite these slightly disparate gradients for the two time scales, to a reasonable degree of accuracy the two can be encapsulated by a single gradient. This is represented in each binned distance's PDF by the solid lines within the figure. The assumption being made here, with the use of a single fit line, is that the waiting time is given by a Poisson process (further details on these processes and their associated distributions are given in 2.4.1). However, it is also clear that priority must be given to either to early or late times if we are to approximate the curves as a process with a single rate. To do this we must consider both the fact that, as a Poisson process, the late times are crucial to capturing the dynamics. But also that, due to their rarity, events of this length are less likely and so the statistics on these are not as good. We find that for our data the single rate fitting based on early times has a characteristic time-scale $\sim$1s and based on the long times $\sim$3s.

To determine which timescale is more important these fits, an alternative method of estimating this wait time can be performed, by measuring instead the bulk effective diffusivity. If we think of the whole trajectory as being made up of diffusive parts and jump segments, with an occurrence average rate λ and length $\langle \ell \rangle$, we are able to estimate an effective diffusivity of the colloids. Here, we are trying to estimate only the bulk wait time, so we exclude trajectories close to the boundary, since we know from the measurements in 3.4(a) that close to the boundary (red curve) the rate is significantly different from the bulk. To distinguish these

trajectories we use the trajectories that lie in a 120μm strip within the centre 200μm channel. Within this strip the average wait time (and hence encounter rate) can be considered constant, since we are far enough away from the boundary to neglect its influence, so we have an average rate $\lambda(y_{ctr})$. The same is true of the length of the jumps, we we consider $\ell(y_{ctr})$. Using the measured trajectory data of the colloids, the effective diffusivity in bulk can be directly calculated. Then by separating the trajectory into diffusive and jump portions, which can be done using the jump detection previously outlined, we are able to calculate the diffusivity in trajectory portions in which the colloids are only diffusing and the net length of the jumps in the remainder of the trajectory. In this case, the long-time diffusivity D_{eff} is

$$D_{\text{eff}} = D_{\text{WJ}} + \frac{1}{2}\lambda(y_{ctr})\langle\ell^2(y_{ctr})\rangle, \tag{3.1}$$

where D_{WJ} is the diffusivity of the colloids within the channel when they are not undergoing a jump and $\langle\ell^2(y_{ctr})\rangle$ is the averaged squared size of the jumps. The experimental value is found to be $D_{WJ} \simeq 0.162 \pm 0.0057\,\mu\text{m}^2/\text{s}$. If instead we work with the full trajectory, without distinguishing jumps, within the central strip then we are able to work out the effective diffusivity $D_{\text{eff}} = 1.82 \pm 0.02\,\mu\text{m}^2/\text{s}$. Finally, we can work out $\langle\ell^2(y_{ctr})\rangle$ by looking at the net displacement of all the jumps that occur within the strip to give $\langle\ell^2(y_{ctr})\rangle \simeq 15.5\,\mu\text{m}^2$. All of these values, together with equation 3.1, then allow us to estimate the bulk rate $\lambda(y_{ctr}) = 0.23\text{s}^{-1}$. For the data in figure 3.4(a) the gradient estimation can be done in the following way. By using the standard least squares fitting to the distribution, which gives a bulk rate of $\lambda(y_{ctr})_{\text{lin}} = 0.97 \pm 0.02\text{s}^{-1}$ or using the least squares fitting to the logarithm of the distribution of the wait times, giving $\lambda(y_{ctr})_{\text{log}} = 0.32 \pm 0.01\text{s}^{-1}$. The result of these two measurements is respectively a weighting toward earlier time and later times. We can see that the latter estimation, which gives more weight to the tails of the distribution, provides a better estimate of the interaction rates when compared to the bulk effective rate, confirming that using the tail of the distribution provides a better match to the average rate measured directly. We therefore extract the effective rates $\lambda(y)$ using the least squares fit to the logarithm of the experimental data and these are the lines are then plotted in 3.4(a) as solid lines. To further support this approximation, we will see that it turn out to be sufficient to recapitulate the distributions both in numerical simulations in 3.3 and in the theoretical modelling in 3.4.

Now that the wait time PDFs have been measured, it is then reasonable to extract the space-dependent encounter rates $\lambda(y)$ from the gradients identified. However, at this point, we must note that the different channels have somewhat

different swimmer concentrations. These concentrations are given in table 3.1. As a result of the different concentrations, each of the channel's colloids sees a somewhat different encounter rate.

We can see these unscaled rates in figure 3.4(b). With a further processing step, re-scaling to the channel swimmer concentration, we recover the same boundary dependence for each of the channels, this is shown in 3.4(c). This extra step accounts for the fact that the swimmer concentrations within each of the channel is quite different. Supporting that, at these concentrations the encounter rate is approximately linear in swimmer concentration. In each channel width in 3.4(c) we see that there is a decrease in the encounter rate near the boundary and a recovery to a bulk value over a similar range in each case. Interestingly, the shape of this curve does not match the positional PDF of the swimmer's distribution. It might be intuitive to assume based on the previously highlighted detail, more swimmers means more jumps (via. the encounter rate), that this would be the case. However, we saw in figure this is not the case, which likely reflects the fact that the proximity to the wall limits the possible directions that the swimmers can move in when interacting with the colloids. A fit to the characteristic encounter rates is given in the figure (solid black), this is an exponential relaxation to a bulk value as the colloid moves away from the boundaries. The analytic function for this fit curve is

$$\lambda(y) = (\lambda_w - \lambda_b) \exp\left(-\frac{y - y_{\text{col}}}{\ell^\lambda}\right) + \lambda_b. \tag{3.2}$$

Here, λ_w is the encounter rate at the wall (boundary), while λ_b is the encounter rate in the bulk of the channels far from the walls, y is the distance to the nearest boundary, y_{col} is a correction for the colloid's finite radius (since y=0 is the boundary) and ℓ^λ is the characteristic length over which the encounter rate relaxes.

Next, we will focus on the net direction of the jumps. Using the start and end positions measured for the jumps, we can measure the distribution this value. In figure 3.5(a) we can see this plotted. Once again the convention is that measurements near the boundary is shown in red, while in bulk is blue. In this figure negative and positive jump orientations indicate jumps towards or away from the boundary

Channel Width μm	Cell Surface Density (cells/μm^2) ($\times 10^{-4}$)
50	2.7 ± 0.7
100	4.5 ± 0.8
150	2.9 ± 0.6
200	4.0 ± 0.7

Table 3.1: Experimentally measured cell density for the different channel widths.
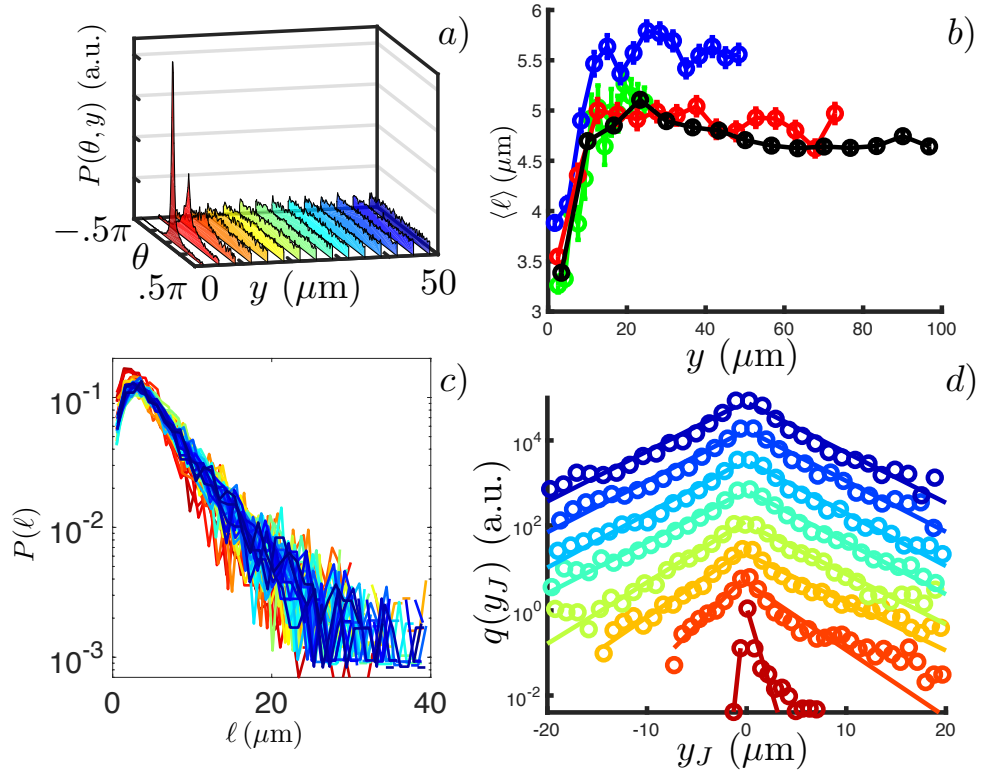
Figure 3.5: **Jump direction and size** (a) A distribution of jump direction, as a function of jump orientation (θ) and distance from the boundary. With close to the boundary shown in red and in the bulk in blue. (b) The average jump size $\langle \ell \rangle$ as a function of distance from the boundary. With channel widths: 50μm (green), 100μm (blue), 150μm (red) and, 200μm (black). (c) The semi-log distribution of the jump size, colourised with red near the the boundary and blue in the bulk. (d) The semi-log distribution of jump sizes projected perpendicular to the boundary. (Red) closest to the boundary and (blue) in the bulk. An exponential is fitted to the positive and negative values for each position, given by the solid lines. These curves have been shifted vertically to allow for easier comparison.

respectively, while $\theta = 0$ corresponds to a jump that was parallel to the boundary. The parallel directions along the boundary are considered equivalent, since it does not matter for our purposes if a colloid moves right or left, parallel to the boundary. We can see for colloids close to the boundary (red) that there is a strong peak in the distribution for $\theta = 0$. There is clearly a strong anisotropy, which reflects the anisotropy of the swimmers motion in this region of the channel, since swimmers in this position are reoriented to swim along the boundaries. This anisotropy has been observed up to $\sim 100\mu$m away from boundaries [151]. The peak of the curve of $P(\theta, y)$ decays exponentially as we move away toward the bulk with a characteristic

length of $L_\theta = 16.4 \pm 0.3 \mu$m.

Next, we will discuss the jump magnitudes. The measured jump magnitudes were similar to those measured in previous studies for micro-sized particles [46, 114]. We can see in figure 3.5(b) that above $\sim 4\mu$m there is an exponential decay in this jump length. From this distribution of jump sizes we can then calculate the average jump length $\langle \ell(y) \rangle$, this is then shown in 3.5 (c). In this figure we have each of the different channel widths represented: 50 μm (green), 100 μm (blue), 150 μm (red) and 200 μm (black). We see that in each case there is a decrease within $10 - 15\mu$m from the boundary of $\sim 30\%$. This decrease is to be expected due to the obvious limitations of the active movement of the colloids imposed by the presence of the boundary.

Since we are interested in the dynamics across the channels it is useful to reduce the full two-dimensional jump distribution functions to their projection $q(y_J|y)$ along the axis perpendicular to the channel boundary. Here, y_J is the associated jump size, with a positive signed jump moving away from the boundary and a negative toward it and y is the position at which the jumps origination, given by the distance to the nearest boundary. In figure 3.5(d) we see these distributions; as before, the colour here represents the position within the channel at which the jump occurred. The plot is given here in semi-log with the circular markers showing the experimental measures. By separating the jumps into jumps towards and away from the boundary we are able to see that they can be reasonably fitted with a straight line, specifically in the bulk (blue) where the plot is reasonably symmetric about $y_J = 0$. It follows then that these jumps can be reasonably approximated with two exponential distributions (further details on these is presented in section 2.4.1). These distributions show some of the strongest positional dependence so far encountered: Near the boundary (orange-red) we see that the characteristic length scale of the associated to the exponential fits starts to change, with the steepest (and therefore shortest length) given by the jumps nearest to the boundary. The measures length scales here start to lose their symmetry, as we noted in the case of the bulk (blue), the exponentials have near-identical characteristic lengths associated. But near to the boundaries we see a strongly non-heterogeneous behaviour. This is likely once again due to the fact that the jumps are highly anisotropic in this region. Further, as a result of the presence of the boundaries, we see that the negative jump size is capped; yellow and orange curves show a cap on the experimentally measures jump sizes for the negative portion of the plot, which is not present for the positive jump sizes. This cap in jump size is due to the presence of the boundary, which physically prevents larger jumps. In the experimental time-lapses, this can be seen
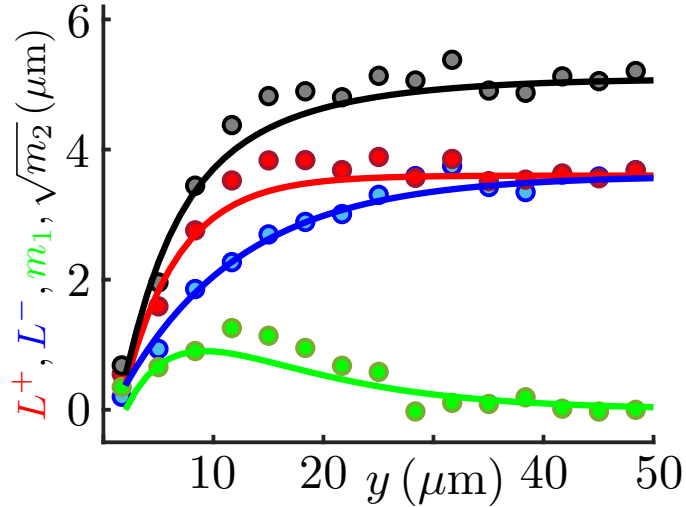
Figure 3.6: **Jump distribution moments** A plot showing the first two moments of the jump distribution $q(y_J|y)$: m_1 given in green, two related values $L^{\pm}$ are in red and blue respectively and, $\sqrt{m_2}$ given in black. In each case the values from the jumps measured in the experiments are shown (solid circles) and a fit given (solid line).

to cause the colloid and swimmers to separate, effectively pre-emptively ending the jump event.

With this distribution, we can then explore its various moments. A few relevant values to be discussed are shown in figure 3.6. We begin with $L^{\pm}$, the characteristic lengths associated to the positive (red) and negative (blue) jumps respectively, as a function of the colloid's distance from the nearest boundary. These are calculated from the gradients of the two exponential distributions for each position in the channel in $q(y_J|y)$, measured by method of least squares to the logarithm of the data. We see in the $L^{\pm}$ plots the difference in the magnitudes of characteristic length between jumps away from the boundary versus towards it. As in previous figures, the circular markers show the experimental values while the solid line is a fit to the data. In both cases we see that the jump characteristic length both toward and away from the boundary increases as we move away from the boundary. However, the jumps that are toward the boundary L^+ increases more rapidly. If we model $L^{\pm}$ as exponentially relaxing from a boundary value (solid red/blue) we have the following analytic functions for these characteristic lengths

$$L^+ = (L_w^+ - L_b) \exp\left(-\frac{y - y_{\text{col}}}{\ell^+}\right) - L_b, \tag{3.3}$$

$$L^- = (L_w^- - L_b) \exp\left(-\frac{y - y_{\text{col}}}{\ell^-}\right) - L_b. \tag{3.4}$$

The value $L_w^\pm$ represents the characteristic jump sizes at the walls (boundaries). These are both equal and fixed as 0.375μm. L_b then is the characteristic jump length in bulk, again this is equal in both cases and is set as 3.6μm from the experimentally measured bulk projected jump size and y_{col} is due to the finite radius of the colloids. Since in bulk the jumps the colloids are eventually uniformly distributed it should be clear that the value of L_b should be equal, leading to bulk jumps being isotropic in this projected direction. The difference then between these two functions is codified in the values of $\ell^\pm$, the characteristic lengths over which the jump's characteristic size decays.

We previously noted that $q(y_J|y)$ was made up of two exponential distributions, which had distinct negative and positive domains which were characterised by the $L^\pm$ values. Motivated by this description, the following form for $q(y_J|y)$ can be proposed:

$$q(y_J|y) = \frac{1}{L^+(y) + L^-(y)} \exp\left(-\frac{|y_J|}{L^\pm(y)}\right). \tag{3.5}$$

With the $L^\pm$ used in the exponential term determined by the sign of y_J. Using these different definitions then we are able to calculate the moments of $q(y_J)$ as:

$$m_n(y) = \int_{-\infty}^{\infty} dy_J \, y_J^n q(y_J|y). \tag{3.6}$$

By breaking this integral up into positive and negative domains we can also write for the first two moments that

$$m_1 = L^+(y) - L^-(y), \tag{3.7}$$

$$m_2 = \frac{L^+(y)^3 + L^-(y)^3}{L^+(y) + L^-(y)}. \tag{3.8}$$

If we calculate the value of equation (3.6), then we get the local drift caused by the asymmetry of jumps toward and away from the boundary. We can see this in figure 3.6 (green), due to difference the rates at which $L^\pm$ recover to the bulk

value there is a net drift. Leading to a near boundary tendency for colloids to be pushed inwards to the centre of the channel. The second moment is then shown in figure 3.6 (black). The square root of m_2 is shown so it's dimensionally consistent with the other curves. Here we see again, this curve can be approximated as an exponential relaxation to a bulk value far enough away from the boundary, while the value decreases sharply near the walls. As a result of this, close to the boundary we have a lower effective diffusivity contribution from the jumps.

3.3 Jump-Diffusion: Computational Modelling of Experiments

With the dynamic properties of the jumps characterised in the previous section, the next step is to check if these features we have highlighted are sufficient to reconstruct the stationary state of the colloid's positional distributions in the channel. In this section we will outline a simple model based off the data from the experimental plots, to see whether such a model does a good job at the reconstruction and further how this model can be modified to highlight the essential dynamical properties.

3.3.1 Jump-Diffusion Simulation Outline

We focus once again on a reduced one-dimensional system, since the dynamics parallel to the boundary are symmetric. The aim is to create a simple simulation in which passive particles are both diffusing and undergoing a Poisson process of jumps studied, as in the previous section. Proceeding in this way, we neglect the explicit presence of the swimmers. Instead the colloids are treated as active Brownian particles (ABP), in this case weakly Brownian, owing to the relatively large size of the passive particle. The active component of the motion has been converted from an explicit active displacement due to the presence of the swimmer to a coloured active noise term resulting from the active bath.

We will start by outlining how the motion of the passive particles is determined when the motion is uninterrupted by jump events. For the passive particles, at each time-step a accept-rejection scheme is implemented using the following tests (full details are given in section 2.4.2). A uniformly distributed random number is drawn and a comparison is made to the interval $\Lambda(y) = [\frac{1-\lambda(y)\delta t}{2}, \frac{1+\lambda(y)\delta t}{2}]$, where $\lambda(y)$ is the rate of the Poisson process and δt is the time-step 0.1s, chosen to match the frame rate of the images in the experiments. Here, following section 2.4.1 we have expanded the Poisson probability of an event to give $1 - \lambda(y)\delta t$, further terms

in this expansion for $\delta t = 0.1$ would result in a contribution $\sim \frac{1}{2}0.1^3$ for $\lambda \sim 0.1$. Thus, our expansion here is sufficient. The jumps themselves are drawn from the discrete experimental distributions of jump size within each bin (without interpolation) and implemented as instantaneous events without interactions, as such a jump within a given bin can take a colloid no further than a bin-width (3μm) outside the system. We use a stopping boundary, which is discussed in more detail later within this section to stop these rare events. If the uniform drawn number is within $\Lambda(y)$ then the passive particle undergoes a jump event, otherwise it will move diffusively with a move size $\delta y = \sqrt{4D_0\delta t}\eta(t)$; $D_0 = 0.0439$ μ^2s^{-1} is the thermal diffusivity of a 5μm particle and $\eta(t)$ is a normally distributed random variable. The form of this δy means we're sampling a normal distribution to get our step sizes for the diffusion. Here, the time-step must be considered as close to the boundary, since diffusion is the only way the time-step enters into the magnitudes of the motion. If we consider a value $\eta(t) \sim 0.05$ at around 2-standard deviations for a normal distribution with variance 1 to give a reasonably rare jump, then the resulting displacement is $\delta y = 0.007\mu$m for $\delta t = 0.1$s. Diffusion as such has a very limited ability to displace colloids outside of the box and this is dealt with using a reflecting boundary which we discuss in greater detail later. Although the time step is large, since we have no inter-particle or particle-boundary interactions and the jump sizes come directly from the experimental distribtuions, the move sizes thus cannot introduce numerical errors from non-physical events. If the jump criteria is met the the passive particle is able to undergo a large non-Brownian event. The size of this can be determined by inverse transform sampling (ITS) the distribution $q(y_J|y)$ (see section 2.4.2 for full details), by doing this jumps can be sampled which are correctly distributed and the size of these can be directly implemented as $\delta y = y_J$. The sampled jumps here are signed, and so based on the sign of the jump from the inverse-sample we have both jumps going towards and away from the boundary. Notice, here we have made a subtle simplification in the dynamics, the jumps measured in the experiments have a finite duration which can be seen in figure 3.7. Within our implementation the jumps are instantaneous. In the experimental system we justify this by noting that the jump durations are on average ~ 1.2s while the waits are ~ 3.5s, sufficiently longer than the overall time that a jump takes. As we will see, even with this jump duration simplification it will be sufficient to replicate the overall outcome of the distributions.

With this in mind, we can define each of the steps using the iterative equation
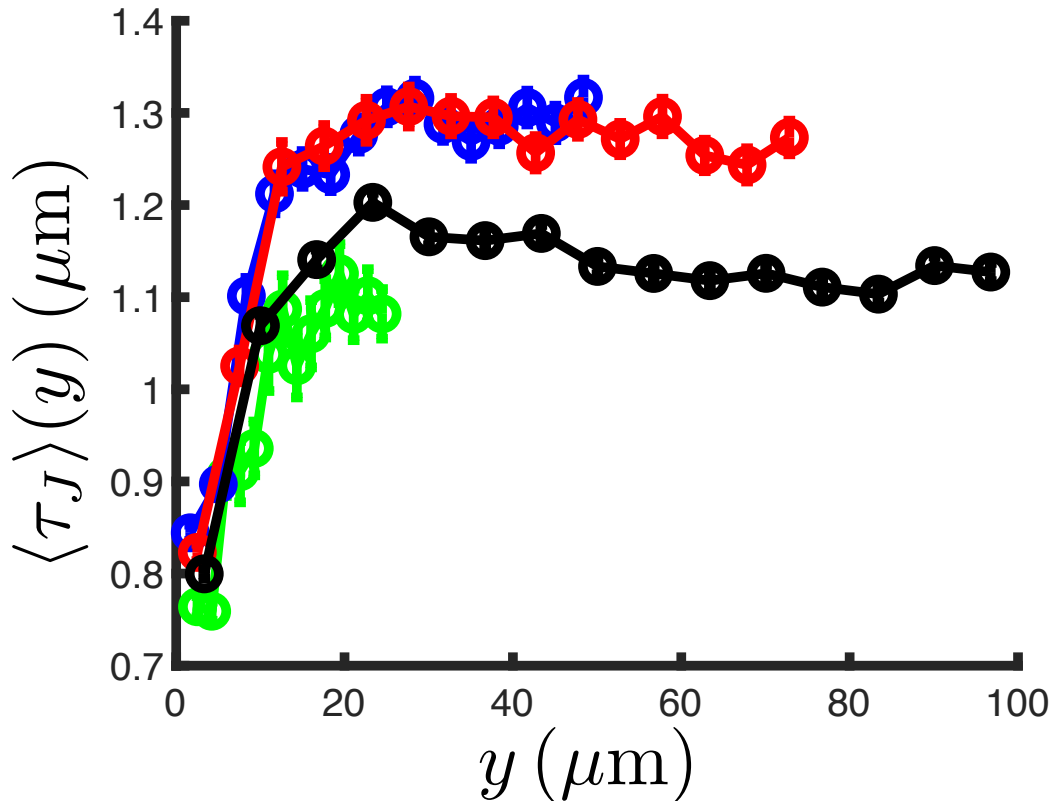
Figure 3.7: **Jump duration** A plot showing the average jump duration as a function of the distance from the boundary. With channel widths: 50μm (green), 100μm (blue), 150μm (red) and, 200μm (black).

$$y'(t + \delta t) = y'(t) + \delta_p(t)y_J(t|y'(t)) + (1 - \delta_p(t))\sqrt{4D_0\delta t}\eta(t), \qquad (3.9)$$

$y'(t)$ is the channel position (which will be defined in detail in subsequent paragraphs), $\delta_p(t)$ an indicator function which determines if the Poisson process is giving a jump and $y_J(t|y'(t))$ the jump generated at time t starting from $y'(t)$. Here, we have neglected the x-direction. As previous stated, it was noted in the experiments that the jump distributions are symmetric in the x-direction for all distances from the boundary. As such, we model the system as pseudo two-dimensional and consider only the projection of the jumps motion normal to the boundary.

As we saw in several previous figures, the colloids dynamics are not defined for the point $y = 0$, since the passive particles have a finite radius, so instead the jump-diffusion process is defined with a new coordinate system, taking values

in $[-W/2 + y_{\text{col}}, W/2 - y_{\text{col}}]$ where W is the channel width and y_{col}, as before, is the passive particle radius. Unlike the previous system, where $y = 0$ was the boundary, these simulations have $y' = 0$ as the centre of the channel. As a result, several quantities must be calculated by transforming the values from simulation coordinates to distance to the nearest boundary coordinates: For example, in ITS to sample jump sizes from $q(y_J|y)$ the value y from the experiments is the distance to the nearest boundary, while the coordinates of passive particle in the system are given in signed distance from the centre of the channel.

The passive particles interact with the boundaries in two distinct ways depending on the type of motion they are undergoing. The first case is when a particle crosses the boundary via a diffusive motion, then the passive particle as a result is reflected back into the channel. For example: A passive particle which would diffuse from $y'_1 = W/2 - y_{\text{col}} - \epsilon_1$ to $y'_2 = W/2 - y_{\text{col}} + \epsilon_2$ will in fact be moved to $y'_2 = W/2 - y_{\text{col}} - \epsilon_2$. This ensures that there is no loss of passive particles through the boundary. This is clearly an approximation for any real system, giving overall a slight overcompensation. However, as we previously discussed the impact of this is negligible for our time-step because the colloids are weakly Brownian with a low diffusivity. Another alternative method would be to use a stopping boundary condition resulting in $y'_2 = W/2 - y_{\text{col}} - \epsilon_s$ where ϵ_s is a fixed but small value, which would give an under-compensation of the boundary effect. However, since the diffusivity is small either approximation would be sufficient. The second case is a boundary crossing which is the result of a jump. In this case it is possible for a passive particle to end up some distance into a physically forbidden area, meaning that a reflective condition here would result in a large over-compensation. Instead a stopping boundary condition is used, where the colloids are placed at a very small distance from the boundary that was crossed. This decision of boundary condition was motivated largely by the experimental movies of the colloids. When they are undergoing jump events due to swimmers, the forces from the boundary generally lead to the colloid disengaging from the swimmer. The result of this is the colloid being left at the boundary while the swimmer continues on. Again, this boundary implementation suffers similar limitations as an approximation to what really happens. However, again we shall see it is sufficient for replicating the distributions.

3.3.2 Jump-Diffusion Simulation Results

The results of this simple numerical resampling of the jumps can be seen in figure 3.8. Here, we have focused on the 100μm channel's distribution (note: We saw in figure 3.2.4 this distribution is reasonably uniform beyond 50μm, so these results
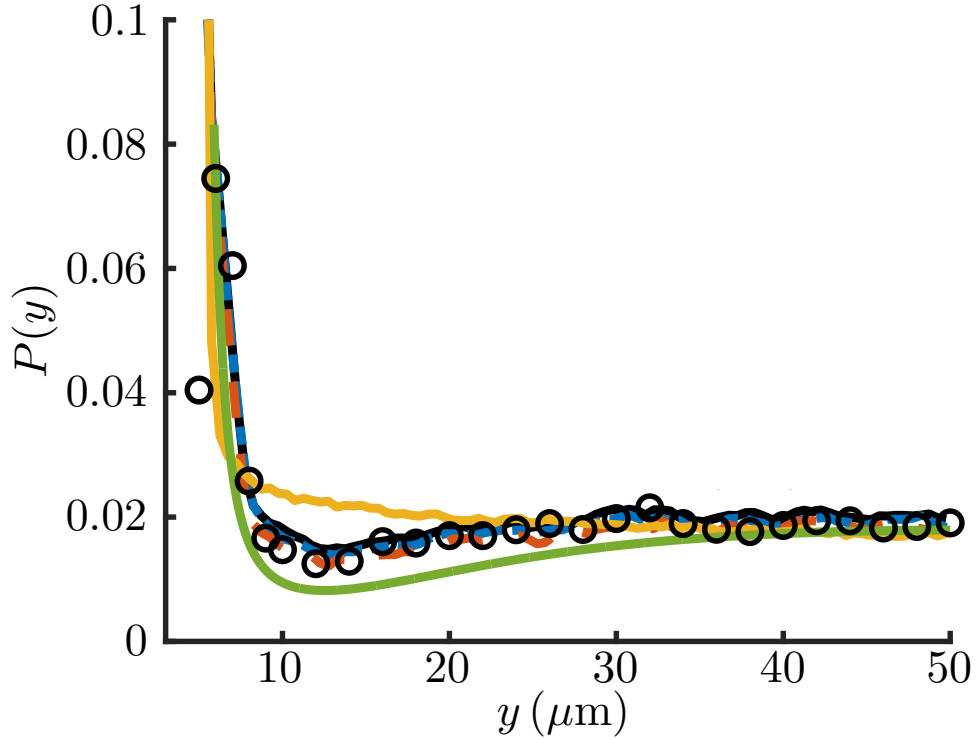
Figure 3.8: **Simulated jump's resampled passive distributions.** Positional distributions resulting from a numerical simulation resampling the jumps, symmetrised. We have: The experimental values (black circles), full dynamics simulation (solid black), no diffusion (blue dashed), bulk-encounter rate (dashed orange), using the bulk jump distribution (yellow), and (green) the predictions of modelling outlined in section 3.4.

can be extended to other channel sizes). The experimental measurements for the distribution are shown as the clear black circular markers, while the full dynamics numerical model is given by the black solid line (this line is under each of the other curves). We can see that there is good agreement of this model with the experimental results. The key features that were highlighted for the distribution are all recaptured: The peak of the distribution at the boundary, the local depletion around 10μm away and finally, the recovery of the overall distribution to a flat profile far away from the boundary. As such, we conclude that the positionally dependent dynamics of the jumps is clearly sufficient to recapture the various long-time behaviour of the colloid's distributions in the experiments.

The next step then is to reduce the overall information we feed into the

resampling, to highlight which of the jump event's features are core to understanding the positional distributions. To do this we can re-perform the numerical simulation described in the previous subsection; systematically removing different aspects of the simulation to see how the overall positional distribution is affected.

Firstly, if instead of $\Lambda(y) = [\frac{1-\lambda(y)\delta t}{2}, \frac{1+\lambda(y)\delta t}{2}]$, we have a homogeneous acceptance-rejection criteria $\Lambda = [\frac{1-\lambda(y_b)\delta t}{2}, \frac{1+\lambda(y_b)\delta t}{2}]$ where y_b is a position deep in the interior of the channel, giving an encounter rate representative of the bulk behaviour of the colloids. The idea of this modification is to remove the spatial dependence of the Poisson process determining when the jumps will occur. We can see in figure 3.8 with the dark blue dashed line the outcome of such a modification. It is clear, the full dynamics are almost indistinguishable and that the positional dependence of the encounter rate is not fundamental to the colloid's distribution. Looking at the positionally averaged encounter rate it makes some sense that this would be the case, since the largest deviation from the bulk value only occurs very close to the boundary.

The next modification to the full dynamics to consider is one in which the non-jump steps do not result in any motion (note: The rate was returned to positional dependence). To do this we can set $D_0 = 0$, so there is no thermal diffusivity of the passive particles within the simulation. This can then be seen within the figure as the orange dashed line; the key features of the distribution are replicated with the line once again nearly indistinguishable from the full dynamics. On closer inspection it can be seen that this line has a small amount of variability around the full dynamics, likely due to the fact that diffusion is no longer smoothing out the distribution. As we have previously noted, the colloids used in the experiments are relatively large and thus only weakly Brownian, so once again it is easy to rationalise that the removal of their thermal motion does not affect their overall distribution throughout the channel.

The final case to consider is jumps drawn from the bulk jump size distribution $q(y_J|y_b)$ where y_b once again is a distance far from the boundary. In this simulation's case we get the yellow line in the figure. There is still a measurable accumulation, which follows from the fact that large jumps near the boundary that lead to the passive particles being outside of the channel are made more possible. The spatial dependence of the jumps (when we include positional dependence) leads to the jumps themselves getting smaller closer to the boundary, especially in the negative direction (towards the boundary). As well as this the depleted region is destroyed entirely, with the curve instead slowly decreasing the the bulk value, which is slightly lower, instead of recovering to it from below. What this tells us then is that the

colloid's positional distribution is largely a result of the spatial dependences in the projected jump length distribution and the asymmetry of the distribution $q(y_J|y)$.

3.4 Jump-Diffusion: Theoretical Modelling of Experiments

In this final section we will now expand on these results. For this, a general analytical model for the system will be outlined. Within this section, we will look at a derivation. Starting by outlining a Langevin-equation that encodes both the colloid's diffusivity and positionally dependent jumps, we will work towards an integro-differential master equation for the system. Finally, we will discuss a method of reducing this master equation to an effective drift diffusion equation for which, given suitable boundary conditions, we can then predict the overall distribution of the colloids.

3.4.1 Derivation of the Jump-Diffusion Fokker-Planck equation

Motivated by the numerical validation outlined in the previous section of the jump-diffusion dynamics and following previous work: [152] we first write a stochastic (Langevin) equation for the passive particle's dynamics

$$Y_{t+\tau} = Y_t + N_\tau + \Delta_\tau(Y_t), \tag{3.10}$$

where τ is an infinitesimal time interval, Δ_τ is a random variable describing the inhomogeneous Poisson process and N_τ is a standard Wiener process. As in the numerical simulations, notice that this derivation has the implicit assumption that the jumps which occur are instantaneous and that the movement from $y - y_j$ to y takes no time.

This can then be used to derive the Master equation for this system. We first write

$$\begin{aligned}P_{t+\tau}(y) &= \langle \delta(y - Y_{t+\tau}) \rangle, \\ &= \langle \delta(y - (Y_t + N_\tau + \Delta_\tau(Y_t))) \rangle,\end{aligned} \tag{3.11}$$

with the angular brackets denoting an average over all noise realisations, which we can express in the following way by integrating over all the possibilities

$$P_{t+\tau}(y) = \int_{-\infty}^{+\infty} dy' P_t(y') \int_{-\infty}^{+\infty} \int_{-\infty}^{+\infty} dy_{\mathrm{J}} \, d\Delta\eta \, p_\tau^{y'}(y_{\mathrm{J}}) r_\tau(\Delta\eta) \delta(y - (y' + y_{\mathrm{J}} + \Delta\eta)), \tag{3.12}$$

where $p_\tau^{y'}(y_{\mathrm{J}})$ is the probability density that $\Delta_\tau = y_{\mathrm{J}}$ at position y' and $r_\tau(\Delta\eta) = e^{-\Delta\eta^2/(4D\tau)}/\sqrt{4\pi D\tau}$ is the transition probability for the Wiener process (with diffusion coefficient D) [153]. Integrating first over $\Delta\eta$ we get

$$P_{t+\tau}(y) = \int_{-\infty}^{+\infty} dy' \frac{P_t(y')}{\sqrt{4\pi D\tau}} \int_{-\infty}^{+\infty} dy_{\mathrm{J}} \, p_\tau^{y'}(y_{\mathrm{J}}) e^{-\frac{(y-y'-y_{\mathrm{J}})^2}{4D\tau}}, \tag{3.13}$$

which we can Fourier-transform, giving

$$\begin{aligned}
\tilde{P}_k(t+\tau) &= \int_{-\infty}^{+\infty} dy' \frac{P_t(y')}{\sqrt{4\pi D\tau}} \int_{-\infty}^{+\infty} dy_{\mathrm{J}} \, p_\tau^{y'}(y_{\mathrm{J}}) \int_{-\infty}^{+\infty} dy \, e^{-iky} e^{-\frac{(y-y'-y_{\mathrm{J}})^2}{4D\tau}}, \\
&= \int_{-\infty}^{+\infty} dy' P_t(y') \int_{-\infty}^{+\infty} dy_{\mathrm{J}} \, p_\tau^{y'}(y_{\mathrm{J}}) e^{-ik(y'+y_{\mathrm{J}})} e^{-D\tau k^2}.
\end{aligned} \tag{3.14}$$

Now we are going to expand Eq. (3.14) at first order in τ. Following [152], we can write

$$p_\tau^{y'}(y_{\mathrm{J}}) = (1 - \lambda(y')\tau)\delta(y_{\mathrm{J}}) + \lambda(y')\tau q(y_{\mathrm{J}}|y') + o(\tau^2), \tag{3.15}$$

where $q_{y'}(y_{\mathrm{J}})$ is the probability of having a jump of size y_{J} at position y' and $\lambda(y')$ is the Poissonian rate at position y'. We can then get the first order expansion

$$\begin{aligned}
\tilde{P}_k(t+\tau) &\approx (1 - Dk^2\tau) \int_{-\infty}^{+\infty} dy' \, P_t(y') e^{-iky'} - \tau \int_{-\infty}^{+\infty} dy' \, P_t(y')\lambda(y') e^{-iky'} \\
&\quad + \tau \int_{-\infty}^{+\infty} \int_{-\infty}^{+\infty} dy_{\mathrm{J}} \, dy' \, P_t(y')\lambda(y')q(y_{\mathrm{J}}|y') e^{-ik(y'+y_{\mathrm{J}})}, \\
&\approx (1 - Dk^2\tau)\tilde{P}_k(t) - \tau \int_{-\infty}^{+\infty} dy' \, P_t(y')\lambda(y') e^{-iky'} \\
&\quad + \tau \int_{-\infty}^{+\infty} \int_{-\infty}^{+\infty} dy_{\mathrm{J}} dy' \, P_t(y')\lambda(y')q(y_{\mathrm{J}}|y') e^{-ik(y'+y_{\mathrm{J}})}.
\end{aligned} \tag{3.16}$$

From this expansion, we can express the time-derivative of $\tilde{P}_k(t)$

$$\frac{\partial \tilde{P}_k(t)}{\partial t} = \lim_{\tau \to 0} \frac{\tilde{P}_k(t+\tau) - \tilde{P}_k(t)}{\tau},$$

$$= -Dk^2 \tilde{P}_k(t) - \int_{-\infty}^{+\infty} dy' P_t(y')\lambda(y')e^{-iky'} \tag{3.17}$$

$$+ \int_{-\infty}^{+\infty} \int_{-\infty}^{+\infty} dy_\mathrm{J}\, dy'\, P_t(y')\lambda(y')q(y_\mathrm{J}|y')e^{-ik(y'+y_\mathrm{J})}.$$

We can now inverse Fourier-transform Eq. (3.17) to get

$$\frac{\partial P_t(y)}{\partial t} = D\frac{\partial^2 P_t(y)}{\partial y^2} - \int_{-\infty}^{+\infty} dy' P_t(y')\lambda(y')\delta(y - y')$$

$$+ \int_{-\infty}^{+\infty} \int_{-\infty}^{+\infty} dy_\mathrm{J} dy' P_t(y')\lambda(y')q(y_\mathrm{J}|y')\delta(y - y' - y_\mathrm{J}), \tag{3.18}$$

and finally obtain the master equation for this system

$$\frac{\partial P_t(y)}{\partial t} = D_0\frac{\partial^2 P_t(y)}{\partial y^2} - \lambda(y)P_t(y) + \int_{-\infty}^{+\infty} \lambda(y - y_\mathrm{J})P_t(y - y_\mathrm{J})q(y_\mathrm{J}|y - y_\mathrm{J})dy_\mathrm{J}. \tag{3.19}$$

The various terms present can be identified in the following way: the first term on the right hand side describes the gain of passive particles to position y via diffusive means, the second term then is a loss of passive particles from position y due to various jumps which lead the the passive particle leaving the position and the integral then describes a summation of all the passive particles which arrive at position y from each of the various initial (previous) positions $y - y_J$ for all possible y_J.

3.4.2 Reduction of the Master-Equation to an Effective Drift-Diffusion Equation

Notice that master equation described above has the integral term, because of this there is no simple analytical solution for the distributions. However, we can perform a Kramers-Moyal expansion (see 2.5.1) on the term inside of the integral, we will now see how this then leads to an effective drift-diffusion equation. First we rewrite $q(y_\mathrm{J}|y - y_\mathrm{J}) = q(y - y_\mathrm{J}, y_\mathrm{J})$ for clarity when performing the expansion of what is being expanded. The expansion used then

$$\lambda(y - y_{\mathrm{J}})P_t(y - y_{\mathrm{J}})q(y - y_{\mathrm{J}}, y_{\mathrm{J}}) = \lambda(y)P_t(y)q(y, y_{\mathrm{J}}) - y_{\mathrm{J}}\frac{\partial}{\partial y}\Big[\lambda(y)P_t(y)q(y, y_{\mathrm{J}})\Big]$$

$$+ \frac{y_{\mathrm{J}}^2}{2}\frac{\partial^2}{\partial y^2}\Big[\lambda(y)P_t(y)q(y, y_{\mathrm{J}})\Big] + o(y_{\mathrm{J}}^3). \qquad (3.20)$$

Insertion of this into our master equation gives

$$\frac{\partial P_t(y)}{\partial t} = D\frac{\partial^2 P_t(y)}{\partial y^2} - \lambda(y)P_t(y) + \lambda(y)P_t(y)\int_{-\infty}^{+\infty} q(y_{\mathrm{J}}|y)dy_{\mathrm{J}}$$

$$- \frac{\partial}{\partial y}\Big[\lambda(y)P_t(y)\int_{-\infty}^{+\infty} y_{\mathrm{J}}q(y_{\mathrm{J}}|y)dy_{\mathrm{J}}\Big] + \frac{\partial^2}{\partial y^2}\Big[\frac{\lambda(y)P_t(y)}{2}\int_{-\infty}^{+\infty} y_{\mathrm{J}}^2 q(y_{\mathrm{J}}|y)dy_{\mathrm{J}}\Big].$$

$$(3.21)$$

From this we notice, several interesting simplifications have arisen. Firstly, the loss term on the right hand side of the equation is now compensated; this follows from the fact that $\int_{-\infty}^{\infty} q(y_J|y)dy_J = 1$, owing to the normalisation of the distribution of jump sizes. Next, we notice that the remaining integrated terms on the right hand side can be identified as the moments of the distribution of jump size $q(y_{\mathrm{J}}|y)$, noting we previously defined $m_n(y) = \int_{-\infty}^{+\infty} y_{\mathrm{J}}^n q_y(y_{\mathrm{J}})dy_{\mathrm{J}}$.

Putting these together and inserting our newly defined moments, we get

$$\frac{\partial P_t(y)}{\partial t} = \frac{\partial}{\partial y}\Big[\Big(D + \frac{\lambda(y)m_2(y)}{2}\Big)\frac{\partial P_t}{\partial y}\Big]$$

$$- \frac{\partial}{\partial y}\Big[\Big(\lambda(y)m_1(y) - \frac{1}{2}\frac{\partial}{\partial y}[\lambda(y)m_2(y)]\Big)P_t(y)\Big]. \qquad (3.22)$$

Here we have collected the various terms, putting it in the form of an effective drift-diffusion equation with effective diffusivity $D_{\mathrm{eff}}(y) = D + \frac{\lambda(y)m_2(y)}{2}$ and effective drift $V_{\mathrm{eff}}(y) = \lambda(y)m_1(y) - \frac{1}{2}\frac{\partial}{\partial y}[\lambda(y)m_2(y)]$. By comparison to previous work [46] we see their asymptotic diffusivity obtained comparable, with a contribution from the jump event frequencies and the variance of the jump size.

With this new effective drift-diffusion equation and the additional stipulation that there is no flux of particles for a given boundary we are able to solve for a closed form of the steady state solution

$$P(y) = \frac{A}{D_{\mathrm{eff}}(y)}\exp\Big(\int_0^y \frac{\lambda(y')m_1(y')}{D_{\mathrm{eff}}(y')}dy'\Big), \qquad (3.23)$$

where A is a normalisation constant. From this we can see that without the asym-

metry of the jump dynamics; $m_1(y) = 0$ everywhere, the result is the solution of a state dependent diffusive process with Itô convention for multiplicative noise integration. Since, in our case the $m_1(y)$ values are significant up to $\sim 30\mu$m away from the boundary the exponential's contribution cannot be neglected.

3.4.3 Jump-Diffusion Effective Drift-Diffusion Model Results

The comparison of equation (3.23) and the experimental measurements is facilitated by the heuristic fitting of various properties of the jumps properties: Using exponential fits for $L^+(y)$, $L^-(y)$ enabled us to write an analytical form for $q(y_J|y)$ and using exponential fits as previously described for λ we had

$$m_1(y) = L^+(y) - L^-(y), \tag{3.24}$$

$$m_2(y) = 2\frac{L^+(y)^3 + L^-(y)^3}{L^+(y) + L^-(y)}, \tag{3.25}$$

$$\lambda(y) = (\lambda_w - \lambda_b)\exp\left(-\frac{y - y_{\text{col}}}{\ell^\lambda}\right) + \lambda_b. \tag{3.26}$$

Armed with this description, we can now construct an approximate jump-diffusion model distribution of the passive particles to compare to the experimental curves. This can be seen in figure 3.8 in the green curve, which has been shifted downwards to allow for better comparison. As with the numerical simulations we see that this approximate jump-diffusion model nicely captures the different key features that we expect: the peak in distribution near the boundary, the depletion and then the recovery to a flat bulk.

Chapter 4

Segregation of Colloids

4.1 Introduction

Following on from the previous chapter, we will look at a set of experimental results. From these a model, motivated also by the previous work, will be used to highlight key aspects of the experimental observations. Once again, we'll be examining a mixture of CR with passive colloids. However, two major changes are present, firstly the colloids themselves will be smaller and second the shape of the chamber in which they coexist is markedly different. Specifically, the chambers are designed with the overall aim of enabling the segregation of the colloids from the swimmers. This segregation occurs largely as the result of the spatial distribution of the colloids in the presence of active particles. We will look first at whether this separation is indeed possible, then look at the dynamics of the underlying process and how the separation is maintained by the continued work provided by the active particles.

4.2 Microfluidic Segregation Experiments

In this section there will be a brief introduction to the experiments performed and where possible an explanation of the design choices.

4.2.1 Experimental Design

As stated previously, the experiments involve a mixture of CR and markedly smaller colloidal particles (diameter of $\sim 6\mu$m). Once again, the chamber is designed to be pseudo two-dimensional, with the device thickness in the range of 14-20μm. As we see in figure 4.1, the chamber has a large circular central region and coming out from this are thin side-channels. The diameter of the overall chamber is 400μm to allow
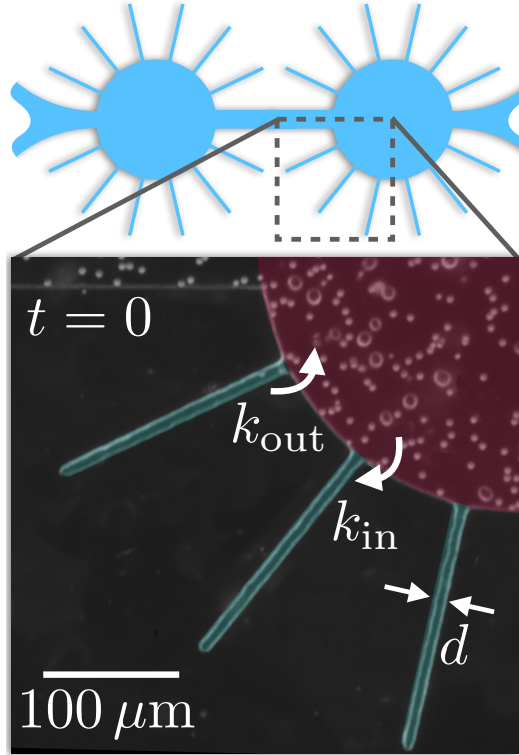
Figure 4.1: **Schematic of the segregation channel microfluidic** (top) Here we see in blue the overall schematic for the microfluidic, with the inlets and outlets on the far left and right. The chambers themselves then consist of large central cavities radius 200μm with offshoots of thickness d=7-8μm. (bottom) An experimental image is shown, with the scale bar. The central cavity is shown in red, the side channels in blue. Within this the two species are present. The colloids are the small round white objects and the CR white outlined grey objects with higher eccentricity. Conventions for the rates of colloidal transport are also defined.

a sufficient number of CR and colloids to fit inside while still keeping the mixture reasonably dilute. As well as this, the resulting chamber walls have a relatively low curvature. The width of the side channels is $7 - 8\mu$m and their length is $\sim 190\mu$m; by design they can fit many of the smaller colloids but they will not fit the CR cells. As such, the chamber's boundary acts as a semi-permeable membrane that can only be penetrated by the colloids. In figure 4.1, we see the central chamber highlighted in red, while the side channels are shown in blue. In this figure we can see the scale of the CR and colloids relative to the side-channels.

From the previous set of experiments we expect that near to any sufficiently flat boundary there will be a sharp peak in the colloid's spatial distribution, then a depleted region outwards from this and finally a bulk uniformly distributed re-

gion. We note here, these expectations stem from the assumption the distributions resulting from a flat boundary can be applied in the circular chamber. Thus, the radius must be such that the local boundary has low enough curvature so as to be approximated locally as flat.

4.2.2 Experimental Colloid Properties

The experiment was performed at 10 frames per second over several hours. The data for the first ~ 320 minutes then contained the dynamics of the system settling from its injected state to the stationary state. As with the previous experiments, this resulted in a time lapse of images of the colloids and swimmers and using the properties of each of the species the particle's positions can be extracted and thus their trajectories digitised.

From the digitised positions we are able to measure the positional distribution within the chamber (red in 4.1). This distribution is shown in figure 4.2. Here, the

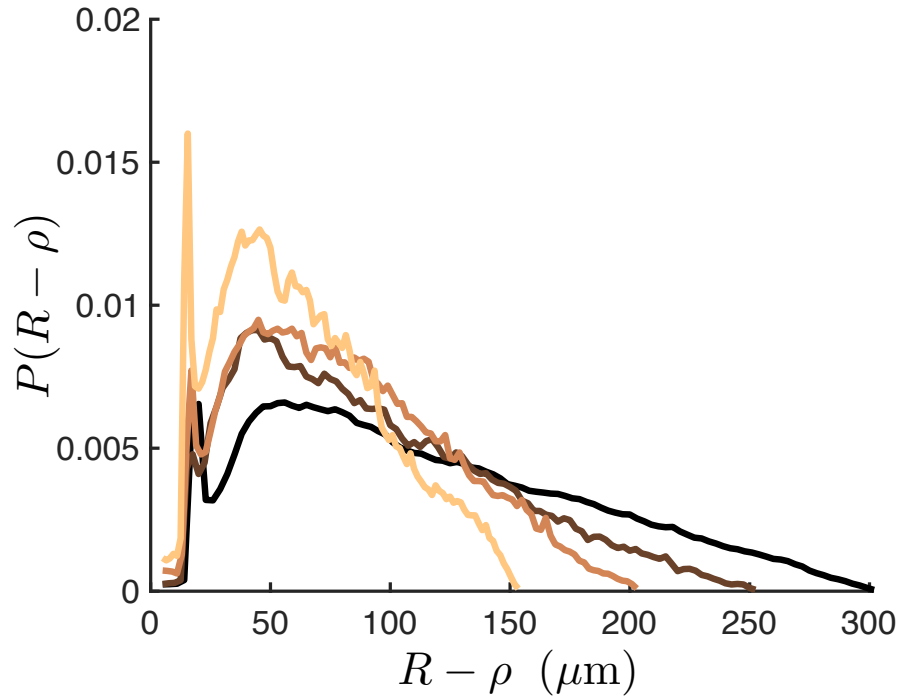Figure 4.2: **Colloid positional distributions within a circular chamber** Here we see the positional distributions for various central chamber sizes. Here, the x-axis shows the distance of the colloids from the boundary calculated from the radius R minus the distance from the centre point of the chamber ρ. Chamber radius R 150μm (yellow), 200μm (orange), 200μm (brown) and, 300μm (black) are shown.

value ρ is the radius used to produce the annulus, of thickness $\Delta\rho$, within the chamber used to bin the colloids, in which the positional distribution is defined. As in the previous case, we see the colloids are restricted from approaching the boundary closer than their radius allows. Matching that highlighted at the start of this section, in our expectations for the experiment, we see the key features of the colloid distribution are present. The peak in the distribution near to the boundary, a depleted region as we move away and finally a recovery to a bulk value. Rather than decreasing to flat value in the distribution we see a decrease in the value. In measuring, we used $\int_0^R P(\rho)d\rho = 1$ to define our distribution. Thus, built into the value of $P(\rho)$ is some information about the area annulus on which it is measured. The area is given as $A = 2\pi\rho d\rho$, notice how this is proportional to ρ the distance from the centre at which we measure, thus the area decreases closer to the interior of the channels we see the value decrease to zero.

As well as this, we can also measure the number of colloids within the channel and the side-channels as a function of time. In figure 4.3 the red line above the others corresponds to the number of colloids in a control chamber which contains no swimmers. None of the colloids were seen to enter the side channels by thermal means during several hours of this control. For the mixture, initially upon flowing the swimmer-colloid mixture there were no colloids in the side channels. However, over time the thermal motion and the interactions with the swimmers then enabled the colloids the move into the side channels. We can see this in figure 4.3. The plots shows the number of colloids (a) and the surface number density (b). The properties of the colloids in the side channels, given as a function of time (showing here the initial ~ 320 min), are shown by the cyan solid line. The red solid line shows the properties of the colloid in the main chamber and the total number of colloids for the two region combined is then shown by the purple solid line. In the figure we can see that the number in the side channels (cyan) increases initially quickly. However, the number moving into the side channels as time goes on decreases and it eventually settles to a stationary state. In response to the entry of the colloids into the side channel we see an equal decrease in the number in the main channel (red). Further confirmed by the fact that the total (purple) remains relatively constant over the course of the experimental measurements. The number of colloids and their number density show a great deal of change within the side channels, but the number density's relative change within the main channel is noticeably lower.

Next we will characterise these dynamics. We call the amount of colloids in the side channels $N_s(t)$, in the central chamber $N_c(t)$ and the total $N_t(t)$; t representing the time. If we assume that there is a constant rate at which the
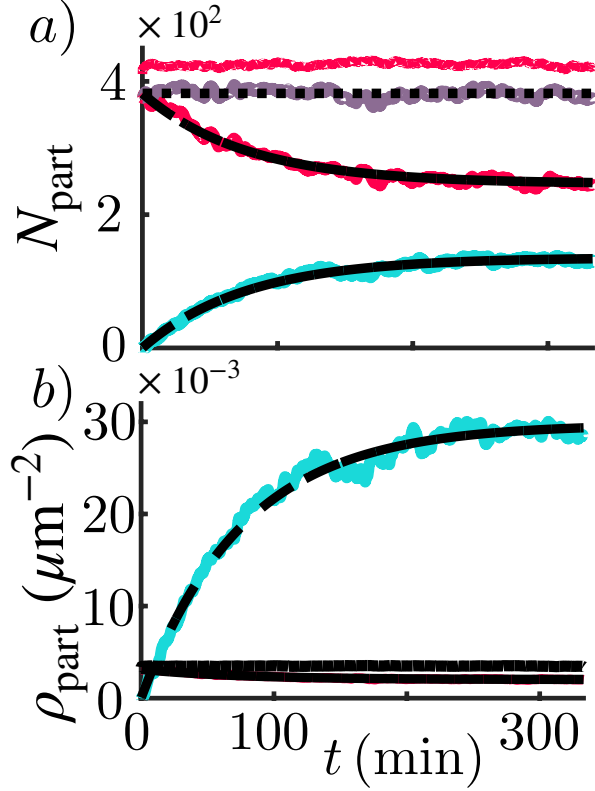
Figure 4.3: **Dynamics of side-channel filling in microfluidic** (a) and (b) Show the time evolution of the number of particles and surface number density within the circular chamber (red solid line) and the side channels (cyan solid line) in presence of the swimmers. Within this time the total number of particles in the chamber remains constant (purple solid line). Dashed/dash-dot lines are a fit to the first order kinetics. The top red line in (a) corresponds to a control without swimmers.

colloids enter and leave the side channels then simple first-order kinetics can be used to model these results. In a first-order kinetic system the following set of equations are obeyed

$$\frac{dN_c(t)}{dt} = -k_{\text{in}}N_c(t) + k_{\text{out}}N_s(t), \tag{4.1}$$

$$\frac{dN_s(t)}{dt} = +k_{\text{in}}N_c(t) - k_{\text{out}}N_s(t). \tag{4.2}$$

Here, k_{in} and k_{out} represent the rate at which the colloids enter and leave the side channels respectively. From the experimental data, we noted that the overall number of colloids that are split between the two sections is relatively constant. Thus, we

have the constraint: $N_t = N_t(t) = N_s(t) + N_c(t)$, allowing us the then solve the two equations, giving:

$$N_c(t) = N_t \left[\frac{k_{\text{out}} + k_{\text{in}} \exp(-kt)}{k} \right], \tag{4.3}$$

$$N_s(t) = N_t \left[\frac{k_{\text{in}} (1 - \exp(-kt))}{k} \right], \tag{4.4}$$

$$\tag{4.5}$$

where $k = k_{\text{in}} + k_{\text{out}}$. This value k determines the relaxation rate of the exponential governing both equations. Using the experimental data this can be estimated as $1/k = 77 \pm 4$ min. Further, we can use the long time behaviour of both regions to determine the following: $N_c^\infty/N_t = k_{\text{out}}/k = 0.64 \pm 0.02$ and $N_s^\infty/N_t = k_{\text{in}}/k = 0.36 \pm 0.02$, leading the estimates for the two rates as $k_{\text{in}} = (7.8 \pm 0.6) \times 10^{-5}\text{s}^{-1}$ and $k_{\text{out}} = (13.9 \pm 0.6) \times 10^{-5}\text{s}^{-1}$. The latter value of which results from the passive dynamics of the colloids within the side channels, which depends on their thermal diffusivity, potential electrostatic interactions with the boundaries, short-range hydrodynamic interactions between the beads, channel design, etc [154, 155]. The former value is the result of the active-displacements of the colloid which results from the interaction with the swimmers. From equation (4.1) we can see that in a stationary state $\frac{k_{\text{in}}}{k_{\text{out}}} = \frac{N_s}{N_c} \sim 0.56$. The relative value comes as a result of a few effects. Overall, there is a great deal more space in the chambers and so the value of N_c takes a higher value. As well as this, the value of k_{out} is heavily impacted by the initial situation of colloids entering the side channel, all colloids that enter the side channel do so at the position of the exit. As such, they are relatively likely to diffuse out of the space quickly and we see this manifested in the value of k_{out} when compared to k_{in}, since the colloids inside the channel have a lot more space to leave the area of the side-channel entrances after they exit. It encapsulates the out-of-equilibrium nature of the system, a property immediately clear when we compare the relative steady-state densities between the side channels ($\rho_s = 0.0295 \pm 0.007 \mu m^{-2}$) and the main chamber ($\rho_c = 0.0019 \pm 0.0001 \mu m^{-2}$).

4.3 Exist Rate Calculation using Various Constant Effective Diffusivity

In this section we will outline a rudimentary method that can be used to estimate the escape rate of colloids k_{in}, whose experimentally measured value is $k_{\text{in}} = (7.8 \pm 0.6) \times$

$10^{-5}\,\mathrm{s}^{-1}$. The result of this model will be within reasonable order of magnitude, but ultimately an overestimate of the value.

The system we will consider is composed of a single particle within a circular chamber, subject to diffusion and in the subsequent section we will include also drift. Both of these properties will have built into them a spatial dependence to their magnitudes. Different sections of the boundary wall of the circular chamber are divided into two types: The first is a no-flux part which the colloids cannot penetrate. The second is an absorbing part where the colloids are removed from the system upon arrival. We will estimate the escape rate as the inverse of the average time taken by a colloid to be absorbed at the boundary. This is of course a case of the famous 'Narrow Escape Problem' [145]. However, it will require two modifications to enable us to predict the escape rates: Firstly, in order to stay faithful to the geometry of the experiments, the boundary must be composed of several distinct absorbing patches, rather than a single one (of the same total size) as would be standard in the Narrow Escape Problem. Secondly, the particles will need to be subject to space-dependent diffusivity and drift, while the Narrow Escape approaches generally have constant diffusivity and no drift. In this section we will look at several possible cases of constant diffusivity. The value of which will attempt to capture the spatial dependence of the dynamics of the colloids. In the subsequent section, we will then see how inclusion of full spatial dependence of diffusion and drifts allows for a quantitive match to the experimental rate measurements.

For a single absorbing patch on the boundary of a disk, the Narrow Escape Problem can be posed as a system of partial differential equations which can be analytically solved for a particle with constant diffusivity [144]. Following this work, we begin noting that solving the mean first passage time, and hence the particle's escape rate, means solving the following Poisson equation with mixed Neumann-Dirichlet inhomogeneous boundary conditions

$$\begin{cases} D\Delta t(r,\theta) = -1 & \text{for } r < R, \, 0 \leq \theta < 2,\pi \\ t(r,\theta) = 0 & \text{for } r = R, \, \theta \in \Theta_a, \\ \frac{\partial t(r,\theta)}{\partial r} = 0 & \text{for } r = R, \, \theta \notin \Theta_a, \end{cases} \qquad (4.6)$$

where (r,θ) are the coordinates on a disk of radius R, D the constant diffusivity, $t(r,\theta)$ the escape time given initial position (r,θ) and Θ_a is the set of angles for which the boundary is absorbing. Here, as opposed to the standard narrow escape problem this is a set of 12 regions with angles corresponding to 7.5μm exits, matching what we had in the experimental system. This set of equations can then be solved
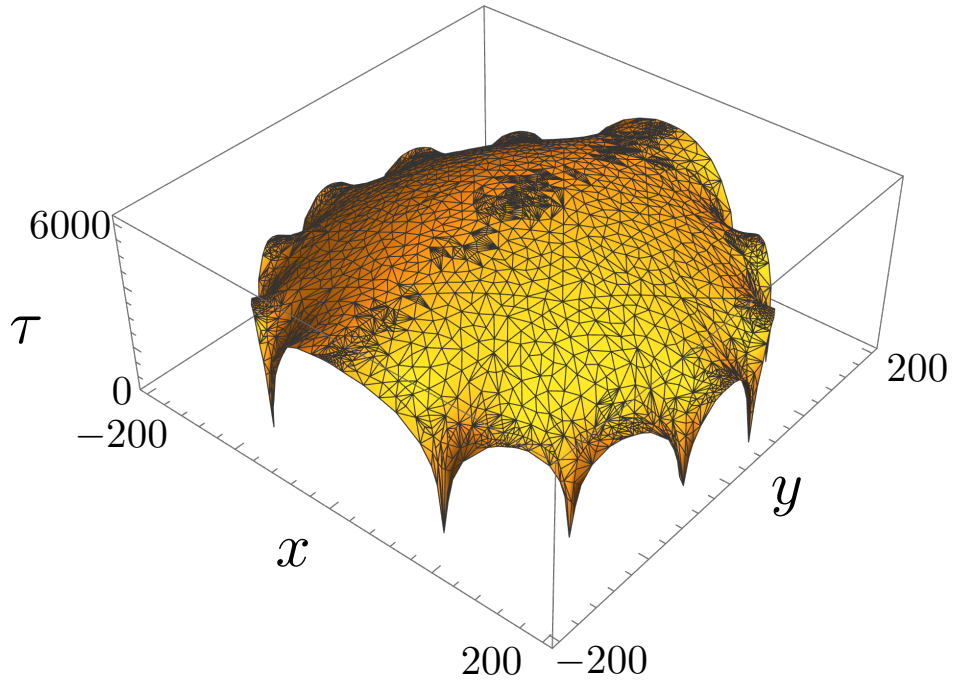
Figure 4.4: **Surface plot showing the numerical solution to equations** (4.6) A plot showing the expected escape time given different initial conditions with $D = \langle D(r, \theta) \rangle$. The exit geometry matching the experimental design, with 12 exits shown as downward spikes on the surface.

numerically for a given prescribed boundary, an initial condition and diffusivity to give the escape rates of the colloids. This diffusivity inserted into the series of equations to be solved is given as constant. To solve this set of equation we propose several appropriate values of constant diffusivity which each codify slightly differently the spatial-dependence diffusivity.

The results for a control case and three chosen constant diffusivities and, their initial conditions are given in table 4.1, which shows the rates obtained from the numerical solution of equation (4.6). The various initial conditions (corresponding to the different columns) used are as follows: The first column describes a particle starting from the exact centre of the chamber and diffusing from there, as such this can be thought of as a lower bound on the expected escape rate, since it is in the position that is the furthest from all of the exits of the chamber. This can be visualised as the time corresponding to $(x, y) = (0, 0)$ in figure 4.4. The next column is then the average rate, calculated from particles that are uniformly

D (μm^{2}s^{-1})	$t(0,0)^{-1}$ ($\times 10^{-5}$ s^{-1})	$\langle t(r,\theta)\rangle^{-1}$ ($\times 10^{-5}$ s^{-1})	$\langle t(r,\theta)\rangle_\rho^{-1}$ ($\times 10^{-5}$ s^{-1})
$D_{\text{th}} = 0.05$	0.228	0.295	0.280
$D_{\text{bulk}} = 3.55$	16.2	20.8	19.9
$\langle D(r,\theta)\rangle = 3.14$	14.3	18.3	17.6
$\langle D(r,\theta)\rangle_\rho = 3.12$	14.2	18.3	n/a

Table 4.1: Escape rates for constant diffusivities in the Narrow Escape numerical model. Th experimental value, for comparison, if given by: $k_{\text{in}} = (7.8 \pm 0.6) \times 10^{-5}$s^{-1}.

distributed throughout the chamber. In this way we have accounted for the particles in the chamber which start off near to one of the exits and then escape through it relatively quickly. This is the average over all the value on the surface of figure 4.4. Finally, the last column corresponds to an initial distribution that follows equation (3.23), normalised to describe a circular chamber. In these, y taken to be the distance to the closest boundary along a line connecting the boundary to the centre (the distribution is assumed to be radially symmetric). This initial condition then accounts for the fact that the stationary state of the colloids is non-equilibrium and that a relatively larger portion of them are closer to the boundary, thus have less distance to travel to escape. As before, this is the average over the value in figure 4.4, but with the weighting as described by the stationary distribution.

The first diffusivity case solved is the thermal value as calculate from Stokes-Einstein, to be performed as a baseline for the other cases: If we use the measured rate for the thermal case to provide a characteristic time for a particle to exit the system we see the time is on the order of ~ 120 hours. From this estimate we gain some understanding of the observation that no colloids entered the side channel in the control experimental case, where there were no swimmers present. Since the duration measured for was only ~ 320 minutes this was not sufficient for the thermal motion even with many colloids.

The next case was the bulk effective diffusivity $D_{\text{bulk}} = 3.55\mu$m^{2}s^{-1} predicted by the jump-diffusion model which was introduced in equation (3.22); specifically, the value is the effective diffusivity far from the boundary. We see in this case the exit rate is 2 orders of magnitude higher than the thermal case, although it is still in each initial condition's case too high.

Below this we have the spatially-averaged effective diffusivity over the whole system, $\langle D(r,\theta)\rangle$, where $D(r,\theta) = D_{\text{eff}}(R-r)$, the effective diffusivity as in equation (3.22) and R the radius of the chamber. In doing this, we have then included also the decrease in the effective diffusivity near to the boundary. As before, we see that this is an overestimate, but closer to the experimentally measured value than in the

previous case.

Finally, we have the case where the diffusivity is $\langle D(r, \theta) \rangle_\rho$, here we have the diffusivity being averaged according a weighting given by the distribution of the particles within the chamber. Owing to the fact that that the averaging is performed according to the stationary state the final initial condition is not performed, since this would be a double-accounting of this distribution. The results in this case are quantitively almost identical to the previous constant diffusivity described.

We see from the results in table 4.1 that in all of the different cases of constant diffusivity that the model over-predicts the rate at which colloids leave the system.

4.4 Modelling using Spatially Dependent Effective Drift & Diffusivity

Up to this point we have limited ourselves to a constant diffusivity and no particle drift. But, we have previously seen in our jump-diffusion model, spatially dependent features naturally arise for such systems. In order to include them in the estimate of the escape, we must perform instead a numerical simulation of a colloid subject to the space-dependent effective diffusivity and drift used in the jump-diffusion model. This numerical scheme uses Milstein's Method (see section 2.4.3 for details), the effect of which is to include an extra term due to the gradient in the diffusivity (since now we have a fully spatial-dependent value) the nature of which depends on the integration scheme being employed to evaluate the noise term. The dynamics for each component are

$$x(t + \delta t) = x(t) + \sqrt{2D(r)\delta t}\, \xi_1(t) + v_1(r)\delta t \cos(\theta) + v_2(r)\delta t \cos(\theta),$$
$$y(t + \delta t) = y(t) + \sqrt{2D(r)\delta t}\, \xi_2(t) + v_1(r)\delta t \sin(\theta) + v_2(r)\delta t \sin(\theta). \quad (4.7)$$

Here, $(x(t), y(t))$ is the position of the colloid at time t, $D(r) = D_0 + \frac{1}{2}\lambda(r)m_2(r)$ is the local effective diffusivity at a position $r = |(x, y)|$, $\xi(\cdot)$ is a Gaussian white noise of variance 1, $v_1(r) = \lambda(r)m_1(r)$ is the drift due to the first moment of the jump distributions, $v_2(r) = \frac{1}{2}D'(r)\left(\xi_i(t)^2 - \alpha\right)$ the drift due to the second moment. The constant α captures the integration scheme [156], with $\alpha = 0, 1$ corresponding to the Stratonovitch and Itô respectively. The angle $\theta = \arctan(y(t)/x(t))$ ensures the drifts are oriented towards the center of the chamber. Finally, the simulations boundary conditions match those described in the experiment.

In these numerical simulations we use: $\delta t = 0.1$s; the same boundary struc-

ture used to estimate the values of Table 4.1 with the mixed reflective and absorbing parts distributed along the chamber's edge; and the KM effective diffusivity and drift calculated for the $100\,\mu$m straight channel, rescaled by the ratio of the concentrations between that experiment and the circular chamber one. The results of this numerical simulation can be found in Table 4.2 for the escape rate given an initial condition of particles at the centre of the chamber, where the error is the stochastic error from the simulations.

α	$t(0,0)^{-1}$ $(\times 10^{-5}\,\mathrm{s}^{-1})$	$\pm$ stochastic error $(\times 10^{-5}\,\mathrm{s}^{-1})$
0 (Stratonovitch)	7.408	0.066
1 (Ito)	3.063	0.027

Table 4.2: Passive particle escape rates calculated from Eq. (4.7), the drift-diffusion model equation including both terms with spatial dependence.

We see that the Ito scheme leads to an under-prediction of the experimental escape rate of the colloids, while the Stratonovich provides an excellent match with the experimentally measured value ($k_{\mathrm{in}} = (7.408 \pm 0.066)10^{-5}\,\mathrm{s}^{-1}$ vs. $k_{\mathrm{in}} = (7.8 \pm 0.6) \times 10^{-5}\,\mathrm{s}^{-1}$ respectively). The exact details of which is the correct choices of integration scheme depends on the system being considered and has been discussed within existing literature [156, 157].

A few final details remain to be captured by the model. Notice, here we implemented a spatially dependent diffusivity and drift, but only the drift (by used of trigonometric function of θ) has directionality. The diffusivity parallel to the boundary, if it is largely driven by the swimmer activity, should be expected to be reduced markedly less than perpendicular to the boundary. It is clear from the good agreement to the experiments that this additional feature is overall minimal, but perhaps, in a less symmetric exit geometry, it would be of greater consequence.

Chapter 5

Mixed System Simulations with Tuneable Active Boundary Scattering

5.1 Introduction

In this chapter we will introduce a computational model, which has been developed to further the study of active passive mixtures. The work presented here differs from the two previous chapters, being an exclusively computational study. Where appropriate, we will refer back to the previous chapters to gain a more intuitive understanding of any relevant situations. The model implemented is an adaptation of [158] which drew originally from [159]. The model is centred around an active broken-fore-aft symmetric three-body swimmer, which plays the role of our active particles within the system. By implementing steep potentials which can act on these particles, we are able to simulate these active particles moving within a confined environment, the geometry of which is tuneable. These same types of potentials can also be used to simulate passive particles, existing within the confinement and interact with the swimmers.

Our model also looks at the dynamics of passive particles under the influence of self-propelled active particles within a confinement. The geometry of the confinement we will study is the same as that of the microfluidic device that we discussed in chapter 3. The aim of our model will be to further deepen our understanding of the interactions of passive particles with swimmers. The key result of chapter 4 was that, by choosing a particular geometry that pairs nicely with the way in which our active particle's scatter, we can produce a desirable non-uniform

distribution of swimmers. As a result, we can accumulate them as a given distance from a boundary. However, in this chapter we ask the reverse of this question. If instead of considering a fixed geometry for our swimmers, can we use swimmers which scatter differently to produce different accumulations that can influence our passive particles. To do this, we use several different active particle properties, which will be discussed as the model is outlined, the swimmers behaviour can be tuned and as a result a broader range of swimmer types can be captured by the model. We will then see how by changing the boundary scattering, we can influence the accumulation of the colloids. Much like the systems that we have encountered thus far, the particle concentrations will be in the dilute regime. The focus remains on the predicting long time behaviours of individual passive particles, by separating their diffusive motion and active particle driven jumps.

5.2 The Broken Fore-Aft Symmetric Self-Propelled-Particle Model

5.2.1 Swimmer Properties & Geometry

The first earliest ideas implementation of such a model is found in [159], in which the active particles were rod structures with fore-aft symmetry. These rods were self-propelled with a favoured direction. When undergoing motion, they had an associated translational (both parallel and perpendicular to the axis of the rod) and a rotational friction tensor. The values of which are given by

$$\boldsymbol{f}_{\mathrm{T}} = f_0 \left[f_{||} \hat{\boldsymbol{u}}_\alpha \hat{\boldsymbol{u}}_\alpha + f_\perp (\boldsymbol{I} - \hat{\boldsymbol{u}}_\alpha \hat{\boldsymbol{u}}_\alpha) \right], \tag{5.1}$$

$$\boldsymbol{f}_{\mathrm{R}} = f_0 f_R \boldsymbol{I}. \tag{5.2}$$

Here, f_0 is a Stokesian coefficient of friction, $\hat{\boldsymbol{u}}_\alpha$ is a unit vector which codifies the orientation of the rod, $\boldsymbol{I}$ is a two-by-two identity matrix, and the trio of non-dimensional values $f_{||}, f_\perp$ & f_R are found using the following equations from [160]

$$\frac{2\pi}{f_{||}} = \log a - 0.207 + 0.980a^{-1} - 0.133a^{-2}, \tag{5.3}$$

$$\frac{4\pi}{f_\perp} = \log a + 0.839 + 0.185a^{-1} + 0.233a^{-2}, \tag{5.4}$$

$$\frac{\pi a^2}{3f_R} = \log a - 0.662 + 0.917a^{-1} - 0.050a^{-2}. \tag{5.5}$$
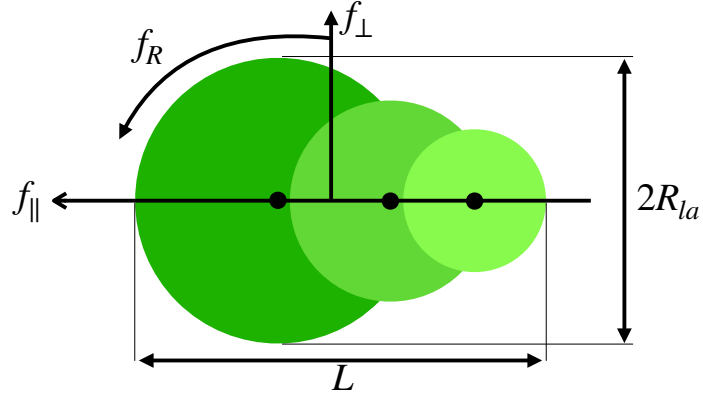
Figure 5.1: **Schematic of the 3-particle active particle** The various lengths and frictional forces for the active particle are shown. An additional active force can then either act to the right (puller) or to the left (pusher).

Here a is the aspect ratio of the active rod. In equation (5.1), the square brackets on the right hand side of the equation can be thought of as a rotation of these dimensionless friction values $f_{||}$ and $f_\perp$ into the direction, and perpendicular to, the orientation of the swimmer.

By use of the friction tensors associated to these values, we can write an equation of motion for the centre of mass of the active rods

$$\boldsymbol{f}_\mathrm{T} \cdot \partial_t \boldsymbol{r}_\alpha = -\nabla_{\boldsymbol{r}_\alpha} U + F \hat{\boldsymbol{u}}_\alpha, \tag{5.6}$$

$$\boldsymbol{f}_\mathrm{R} \cdot \partial_t \boldsymbol{u}_\alpha = -\nabla_{\hat{\boldsymbol{u}}_\alpha} U. \tag{5.7}$$

Here, $\boldsymbol{r}_\alpha$ is the position vector of the centre of mass of the rod, $\nabla_{\boldsymbol{r}_\alpha}$ and $\nabla_{\hat{\boldsymbol{u}}_\alpha}$ are the positional gradient and the gradient on a unit circle respecticely, U is a potential (the exact form of which will be discussed in subsequent sections) and, F is the active force, which drives the self-propelled motion.

Both, equations (5.6) and (5.7) can be straightforwardly solved by pre-multiplying by the inverse of the friction tensors. Using suitable numerical solutions for the resulting differential equations we can get particle trajectories.

Following [158], which builds on this active-rod model, active particles within the system are instead made up of three overlapping circular segments of decreasing size. The reason for this modification is to account for the area swept out by the average motion of the flagella from the microswimmer being modelled. As noted in [158], a triangular shape with a fixed orientation captures well the area that is swept

out. But for practical purposes a series of overlapping circles is more appropriate for a computational model, since such segments each have radial symmetry. We can see such an active particle in figure 5.1, with the frictional components marked. The circles themselves have three distinct radii, relating them to the largest, which is marked in the figure as R_{la}, we have: $\sqrt{2}R_{\mathrm{me}} = R_{\mathrm{la}}$ for the medium and $2R_{\mathrm{sm}} = R_{\mathrm{la}}$ for the smallest. The centre of the next smaller circle in the series sits on the circumference of the larger circle adjacent to it. Notice here, the work by [160] relies on the particle being a rod. Here, we are assuming that the friction coefficients for a rod applies to a three overlapping particle system, using an aspect ratio $a = L/R_{\mathrm{la}}$.

As mentioned in the introduction, one of the aims of this model is to enable the simulation of a broader class of microswimmers. To achieve this, the preferred direction of motion, which is represented within the model by the sign of the active for F, can be easily modified. This allows the model to easily make the switch between an active particle that is a pusher or puller [158].

The model up to this point has represents a ballistically moving swimmer, which is not what is seen in experiments with real swimmers, with their motion made up of run-and-tumble. To begin to account for this, we can easily alter our equations of motion by including a rotational noise term. A noise of the form $D_{\mathrm{R}}\zeta(t)$, where D_{R} is a rotational diffusivity and $\zeta(t)$ a gaussian white noise. From the inverse of this rotational diffusivity we set a timescale in which the direction of the active particle's orientation, $\boldsymbol{u_\alpha}$, de-correlates. This enables us to model swimmers with built in turning dynamics. We should note, a term could also be added into the positional dynamics as translational diffusion. However, owing to the relatively large size of the microswimmers and their high speed, in most cases many times their body-length, this contribution will be neglected.

5.2.2 Particle Forces

Now that we have established the active particle geometry and dynamics when they are unimpeded, we can also include interactions between the boundaries and species within the system. The inclusion of passive particles into the system is relatively straightforward. Passive particles are in effect just active particles with only one segment and with no active force (i.e. $F = 0$). Thus, using the equations of motion described thus far we can also include passive particles. Unlike the swimmers, these particles are given a translation diffusion.

As well as the passive particles, we can also include confining boundaries. Within this work we adopt a geometry matching that of the straight channel microfluidic experiments from chapter 3. As such, there are two parallel boundaries

at the top and bottom of the system. Active (and passive) particles encountering these boundaries experience a potential, the result of which is a force which acts perpendicular to the boundary. The remaining two boundaries in which the system is enclosed are implemented as periodic, with particles passing through the left side of the system ending up on the right and vice versa.

The interaction potential between these species will now be discussed. In equation (5.7), which described the equation of motion for the active particles, we had a term $-\nabla_{\boldsymbol{x}} U$, where $\boldsymbol{x}$ was occupied either by the position vector or the unit vector which encoded the active particle's orientation. This term is a force which is the result of the active particles interacting with various bodies within the system. Within [159] and [158] this was a Yukawa-Potential [161]. However, in our model the form of this potential is modified to be a WCA potential (details on this can be found in 2.4.4). This potential has a cut-off beyond a given distance allows which the potentials value to be set to zero. The distance of the cut-off $r_c = \sigma^{\frac{1}{6}}$ for the WCA potential is determined by the radii of the interacting bodies. The sum of the two radii values of interacting particles/segments can be used to set an appropriate value of r_c in particle-particle interactions, while in particle boundary the particle radius sets r_c The only remaining WCA parameter is then ϵ, a scaling factor, which allows very straightforward tuning of the steepness of the potential. Yukawa in contrast to this requires two parameters to tune the steepness and extent of the potential, which in contrast to WCA is infinite, making WCA easier to modify.

The value of the function U_i for the ith active particle is calculated as

$$U_i = \sum_{s \in S} \sum_{j \in \Sigma \backslash \{i\}} \sum_{\sigma \in S} U_{is;j\sigma} + \sum_{s \in S} \sum_{c \in \Gamma} U_{is;c} + \sum_{s \in S} U_{is;w}. \tag{5.8}$$

Here, we can there are three main type of contribution to the total potential. The first of which are the contributions from $U_{is;j\sigma}$, the potential that is a result of segment s of active particle i with the segment σ of active particle j. The set S is then the collection of all three of the segments of the active particles. To capture the full interaction we need to look at each of the segments of the swimmer we're interested in as compared to each other swimmer (and all their individual segments), this set is given as $\Sigma \backslash \{i\}$. The second contribution comes from terms of the form $U_{is;c}$, this is a back-force of the passive particles acting on the swimmers. Here, this can be summed over all of the colloid in the system for each segment of the active particle to give the total contribution. Finally, the third term is the contributions of the form: $U_{is;w}$, these are interaction of the active particles with predefined boundaries in the system. As previously mentioned, these interactions act purely

perpendicular to the boundaries to prevent active particles from escaping from the system.

For calculating the potentials acting on the passive particles there is a slightly simpler overall equation

$$\sum_{s \in S} \sum_{i \in \Sigma} U_{c;is} + U_{c;w}. \tag{5.9}$$

Here, we have a contribution from each of the different swimmers in the system acting on the passive particle and a contribution from any boundaries on the particle. The passive particles don't see each other within their potential terms and so cannot interact with each other.

Using the total potential of each particle, we can now calculate the gradient in the x, y (and θ for active particles, which have orientation) directions to determine the forces and torques that the particles are subjected to, the explicit forms of which are given by equations (**??**) and (**??**). This is then all the information needed to enable appropriate numerical schemes to calculate the trajectories of all of the particles in the system (an introduction to the details of which is given in 2.4.5). The solution scheme used is a second order SRK, implemented following closely as outlined in [140].

5.2.3   Near-wall Swimmer Kick Events

The last feature of the model which differs from previous implementations is the presence of a Poissonian kicking-process, which occurs near the boundaries. It has been previously noted that microswimmers near boundaries will escape at relatively sharp angles. The scattering angle of microswimmers in the vicinity of a surface is largely dictated by flagella or ciliary contact [162, 163]. This is not an effect which is captured by the current dynamics. The only way in which an active particle can currently leave a boundary, with which it is aligned, is via reorientation caused by rotational diffusion. To enable this scattering effect, we include a small layer near to the boundary. Once an active particle's centre of mass is within this boundary layer each time step an acceptance-rejection Poisson criteria is initiated. If the check is failed, then the particle continues and only the WCA potential, due to other particles/boundaries, can affect its trajectory. However, if the check passes then the active particle is subject to a constant torque, the sign of which is determined so as to rotate the swimmer out of the boundary. For example, a swimmer approaching the lower boundary at an anti-clockwise 45-degree angle to the vertical, the torque applied will also act anti-clockwise. The applied torque is then maintained until

the centre of mass of the active particle passes out of the boundary layer in which the kick process occurs. It is clear that this kicking process is characterised by two parameters: the associated kicking-rate of the Poisson process and the magnitude of the applied torque. It should be noted here, the possible values of the torque can be bounded above for boundary layers of appropriate thickness. This is because it should not be possible for a swimmer facing (even slightly) right to leave the boundary facing to the left. It is this phase space of kicks that allows us to tune the behaviour of the active particles. Thus, using these kick properties we are able to model a range of microswimmer boundary behaviours. As such, in the following results section the focus will largely be on the passive particle dynamics resulting from different positions within this kick phase-space.

5.2.4 Simulation Parameters

For the simulation there are several more parameters of note, which we will discuss prior to the presentation of the results. Firstly, the simulated system was 500μm (between the periodic boundaries) by 100μm (between the WCA boundaries). Within the system there were 20 active particles, each with an overall length of $L_s = 15\mu$m, with the individual segments proportioned as described in section 5.2.1. The swimmers move as pushers (smallest segment first) with a speed of $\sim 100\mu$m s^{-1}. Their rotational diffusivity was set as $D_{\mathrm{sr}} = 0.5$Rad^{2}s^{-1}, the corresponding 2s for a de-correlation of the direction means this kind of active particle behaves highly ballistically.

As well as the active particles there were 40 passive particles in the system, each with a radius 2.5μm, with a thermal diffusivity $D_c = 0.2\mu$m^{2}s^{-1}. These passive particles cannot interact with each other, as outlined in section 5.2.2. As a result of the two species concentrations, the system is well within the dilute regime.

The realisations of the system correspond to 16 different kick frequencies and 6 kick torques. The kick frequency range between $[\frac{25}{16}, 2\frac{25}{16}, ..., 16\frac{25}{16}]$ (Hz). This corresponds to respectively a 0.0781% and 1.24% chance per time-step in the boundary for the lowest and highest. After entering the boundary layer in which the kick process can be activated, which is 1.5 times the size of the largest segment, to reach the boundary (at which point the WCA potential begins to reorient the swimmer) there are at least 150 time-steps (since swimmers move at 100μms^{-1} with $dt = 0.0005$s). Treating the kicks as binomial, the mean number of events in this time are respectively at least 0.117 and 1.86. This gives a good range of behaviours, with the low-kick frequency samples seeing the swimmers generally reaching the boundary, aligning via. the WCA-force and then reorienting due to a scattering by a kick, while

high-kick frequency are rapidly scattered, reorienting and moving out. The kicks then have an associated torque after they have been triggered. This is implemented as a constant change in swimmer orientation, directing it toward the outward normal, per time-step. The torques take values in the range [0.0001,0.0002,...,0.0006] (Rad), this set was chosen using empirical observations in test cases, with an active particle directed into the boundary with high kick-frequency. The results of which showed the low torque cases are slower to leave than the higher and result in a shallower exit angle. Further exploration of this phase space is desirable. However, we shall see that these values are sufficient to show non-trivial differences in the resulting passive distributions.

Finally, the overall elapsed time for each realisation of the system was 4000s, with a time-step dt of 0.0005s. The two values of which must be determined by practical restraints. Firstly, a longer total time is, from a data analysis stand-point, generally good, since this means more overall data. However, it also means a longer run-time, which can be impractical. Using Parallelisation of the different runs, each of the kick-frequencies were run in parallel, and the code's run-time brought down from around a week to 1-2 days, allowing for longer elapsed times within the runs. The time-step poses several challenges, since a higher time-step means a faster code. However, a higher time-step can introduce several undesirable artefacts. As a specific example, within the code the active particles move at a fixed speed. As such, the given time-step can be used to calculate the maximum distance into a potential (either from the boundary, another active particle or a passive particle) that an active particle can reach. If the time step is large, then so too is this distance, which can lead to massive non-physical displacements since the WCA is a very steep potential. Smaller time-steps can of course negate such issues, at the cost of a greater run-time. Overall the time-step arrived at was found to be a reasonable compromise between these different opposing considerations.

5.3 Simulation Results

In this section we will outline the results of the simulation. As with the results in chapter 3, this will consist of looking at the overall passive particle distributions. Following this we will then focus on the jumps within the trajectories. In this case, there is no need to describe a method of detecting the jumps themselves from the trajectories. This is because within the simulation, associated to each passive particle, a value can keep track of whether or not there is a non-zero force acting on the particle (not including from the boundary). Thus, we can easily separate out
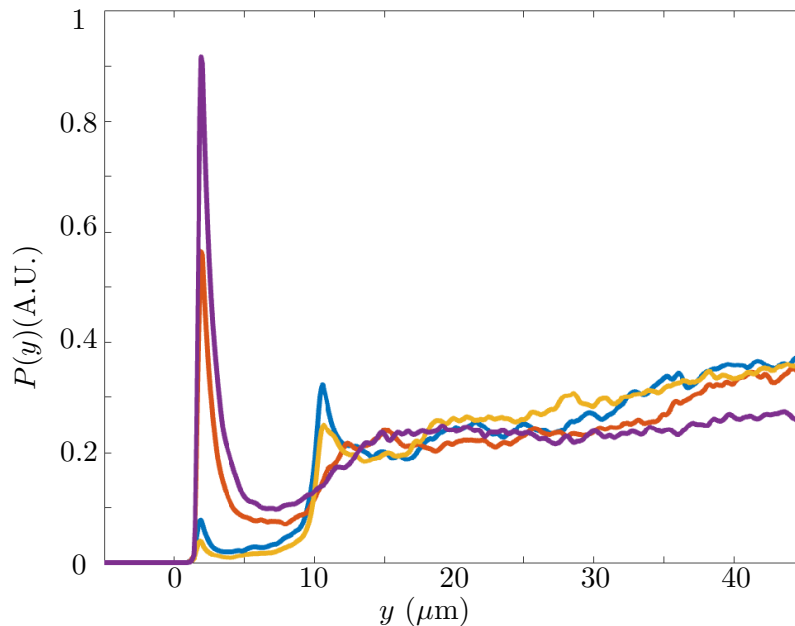
Figure 5.2: **Extrema passive particle distributions.** The passive particle distributions are shown corresponding to the extremes of the kicks sampled in the simulations. (Blue) Low kick frequency, low torque. (Red) High Kick frequency, low torque. (Yellow) Low kick frequency, high torque. (Purple) High kick frequency, high torque.

the times when the particles are in contact and thus, when a jump is occurring.

5.3.1 Active and Passive Positional Distributions

In figure 5.2 we see a few select examples of the distributions of passive particles. With each of the cases, the boundary is placed at $y = 0$ and the curve has been symmetrized about the centre of the channel. First we look at some special cases to highlight the effects which are at play. The lines in the figure correspond to the four most extreme cases of the kick's properties.

The first of which cases is the low kick frequency and low torque (blue). In this distribution we see the presence of two distinct peaks at $\sim 2.5\mu$m and $\sim 12.5\mu$m. Between these there is a relatively depleted region and after the second peak another depletion, after which there is a recovery to a boundary value (with a slight increase). In this case the active particles, upon reaching the boundary, take a while to undergo a scatter. The WCA-force aligns the active particles parallel to the boundary and they then move along the boundary, until such a time that a kick event can remove them. As a result of this, the active particles occupy primarily the area very close

to the boundary, making it difficult for the colloids to reach the boundary. In the case where colloids end up near the boundary they then spend relatively more time very near to it, which is the origin of the first accumulation at 2.5μm, notably equal to the radii of the passive particles. The second accumulation interestingly would seem to be the result of the boundary trapped swimmers themselves acting as a kind of pseudo-boundary. The largest segment of the swimmers has a diameter of $\sim 10\mu$m, combining this diameter with the radii of the passive particles we see the resulting second accumulation at $\sim 12.5\mu$m. After this point, there is then a slight depletion and then a recovery to a bulk value far away from the boundary. In this case there is a slight increasing of the distribution even as far away as 40μm, this could be because there is a persistent alignment of the active particles (which are themselves very ballistic), far away from the boundary. Exploring this further would either require data from a much wider channel or using active particles with a higher rotational diffusivity, to enable them to de-correlate.

Next, the yellow curve, which corresponds to the case when there is a low kick frequency but a high kick torque. This shares many of the different features of the first case. The only differing features are that the accumulations are both markedly smaller. This is likely due to the fact that for higher torque means that active particles are scattered with a steeper angle. This combined with the active particle's ballistic motion means they arrive at the opposing boundary faster and return to their confined state. With more swimmers near the boundary for longer this further restricts the presence of the colloids. The other notable feature, is the slightly faster increase after the second accumulation point.

The third case we consider is the high kick frequency and low torque (Red). In this we no longer have the two accumulations, instead there is a much larger boundary accumulation, a depletion region, a recovery to the bulk and finally a slight bump in the distribution close to the centre of the channel. Opposed to as we had in the previous two cases, the high-kick frequency now means that swimmers that reach the boundary are rapidly scattered and ejected from the area to the channel centre. As a result, the boundary region is much more hospitable to the passive particles, which spend relatively more time in the region. Thus, we see the sharp accumulation peak. The area in which the active particles are scattered ($\sim 7.5\mu$m from the boundary) is then depleted, since this is the area where the swimmers spend a good deal of time while they are being reoriented. In the case of the red curve, due to the lower kick torque, the active particles are scattered to a shallower angle, meaning they likely spend more time in the region out from the boundary ($20 - 30\mu$m) and so we see a slight increase in the distribution in the
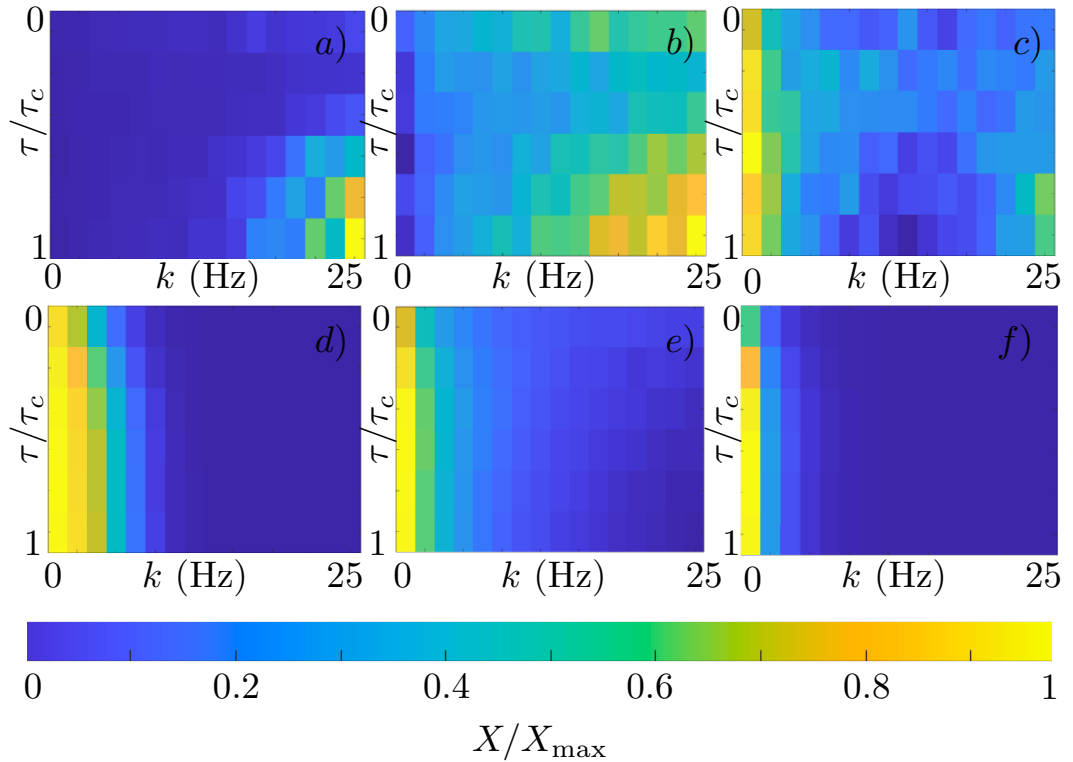
Figure 5.3: **Accumulation heatmap for passive and active particles**. (a-c) Heatmaps for the passive particle distributions are shown. The accumulation is measured using distribution kurtosis (a), a near-boundary integral of the distribution (b) and the variance of the distribution (c). (d-f) Heatmaps for the active particles are shown, following the same order of accumulation rule respectively. All values are shown as relative to the maximum value.

centre of the channel.

Finally, we have the high kick frequency and high torque case (purple). Many of the features are common to the purple as the red curve, with the exception of the slight increase in the centre of the channel. Instead at $\sim 15\mu$m the bulk value for the curve is reached and the value remains relatively stable. We see in this case a curve very similar to what we had in the microfluidic experiments in chapter 3, with each of the key features we highlighted present.

Now that we have seen the features of some specific cases, we can look at the full set of results. This can be see in figure 5.3: Figures (a-c) relate to the passive particles, while (d-f) relate to the active particles. The columns then correspond different methods of measuring the boundary accumulation. The aim here is, for a given point in the frequency-torque phase space, to associate a single value which

tells us the relative amount of particles at the boundary as compared to in the bulk region of the channel.

In the left column of figure 5.3, (a,d), we look at the kurtosis, $X = K$, of the distributions. This is a measure of whether a given distribution is overall heavy tailed [164] and in this case, since we centre our distributions on centre of the channel, a heavy tailed distribution (high kurtosis) corresponds to the particles being largely at the boundary. We see for the passive particles in subfigure (a) for lower kick frequencies there is a lower kurtosis, while at higher kick frequencies the value increases. This matches with what we saw in the specific cases of figure 5.2, with high frequency cases having relatively more accumulation. As well as this, we see that as we increase the torque there is even higher kurtosis. This again matches with the differences we saw between the red and purple curves from 5.2. This method however, presents a clear limitation. We see that for the low torque cases there is little difference between the low and high kick-frequency cases, while in figure 5.2 we saw that these have very different properties (curves: red vs. yellow). In panel (d) we see the kurtosis for the active particles. As expected for the higher kick frequencies we get a lower value, since the swimmers are rapidly moved away from the boundaries by scattering. For the lower kick frequencies we also see that decreasing the torque leads to a slightly lower kurtosis.

In the middle column (b,e) the method of classification is integration of the distribution from 0 to 15μm, $X = I$. As we saw in the previous figure, this was the area where the majority of the non-bulk behaviour was present and so this is another possible method of classifying the boundary accumulation. The results are very similar to what we saw with the kurtosis. Again, high frequency and torque in the passive case (b) shows a larger accumulation, with a decrease in the value for lower frequencies. Unlike in the case of the kurtosis however, for the lowest torque case we see that there is a slight difference in the value of the accumulation measure, with the higher kick-frequency showing a higher value than the lower. For the cases in figure 5.2 red and purple, this measurement registers that there is indeed a difference between the two. However, it does not retain what form the difference takes. For the active particles, shown in (e), we see largely the same as in the kurtosis case (d), but again with greater gradation between the maximum values and the minimum.

Finally, we have the right column (c,f). These plots come from looking at the variance of the distribution $X = V$. This means, the plot quantifies the difference between a uniform distribution and the measured distributions. Again, we see high frequency and torque has a clear signal, the intermediate kick frequencies have a
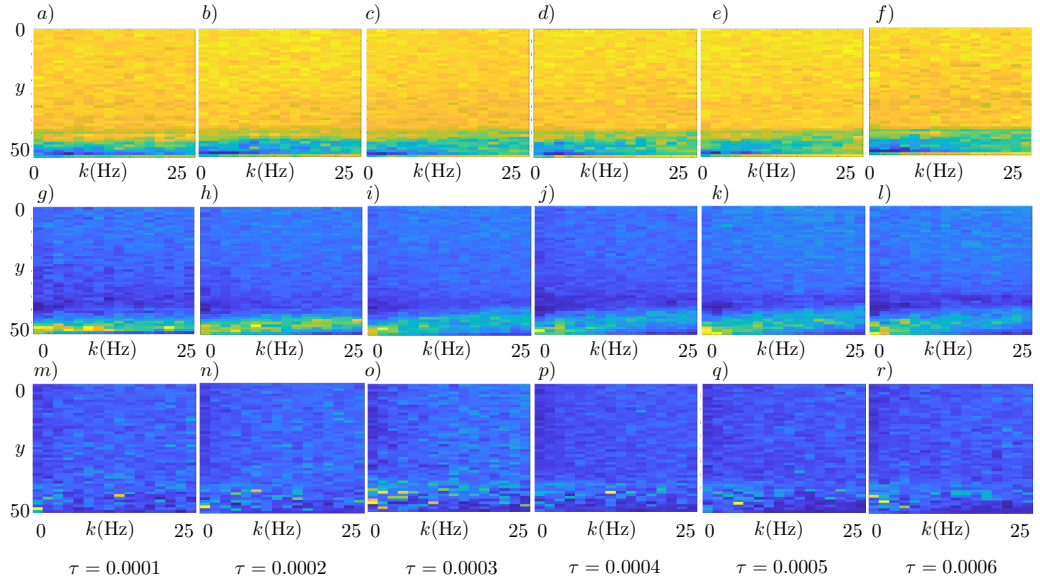
Figure 5.4: **Jump Properties** (a-f) Show the variation of $m_1(y)$, (g-l) shows the variation of $m_2(y)$ and (m-r) shows the variation of $\lambda(y)$: Each are given as a function of distance from the channel centre ($y = 0$). In each case the columns correspond to the kick-torque undergone by the active particle and the x-axis in each figure the kick-frequency.

relatively lower overall variance and then the low kick frequency values show the greatest values. This is likely due to the increase from the bulk value in the very centre of the channel and large depletion region we saw in figure 5.2's blue and yellow curves. The active particle variant of this measure matches well the two previous values, but shows the least intermediate features, sharply transitioning from high values for the low frequencies to low values for medium-high values.

Now that we have classified the distributions and discussed measurements of accumulation, we we now proceed as we did with the experimental data, by looking at the properties of the jumps.

5.3.2   Passive Jump Properties

In the previous analysis of the jumps, we initially highlighted the rate, length and orientation as the key features of the jumps. As reconstruction of the positional distributions progressed we further refined this list of jump features to the average encounter rates and the first two moments of the length distribution, when projected into the direction perpendicular to the boundary. Following this, we proceed in the same way, examining the values of $m_1(y), m_2(y)$ and $\lambda(y)$.

We can see these properties in figure 5.4. In this case, the various columns of subfigures correspond to the different jump-torques. Within each of the subfigures then, the x-axis corresponds to the kick frequency and the y-axis corresponds to the distance from the centre of the channel (data is symmetrized, as was done the positional distributions). The tops within the figures the bulk while the bottom values are near the boundary. The rows then correspond to the three properties of the jumps, which we highlighted as the most important features: The top row (a-f) being the values of $m_1(y)$, the middle row $m_2(y)$ and the bottom row showing $\lambda(y)$.

First, we will look at the relative differences in the $m_1(y)$ profiles. Here, yellow corresponds to high values, while the blue corresponds to lower values. As was the case for the experiments, the drift caused by $m_1(y)$ points away from the boundary, towards the channel's centre. Hence, the sign of the drift is negative, relaxing to zero in the bulk. Indeed, this is what we see in each realisation of the system, with the strongest inward effective drifts near to the boundary. For lower torque cases (a-c) there is a relatively small difference in the near-boundary behaviour between the low and high kick frequency (at $\sim 47\mu$m). However, in the higher torque case we start to see more contrast between the two, with low frequencies having larger magnitudes of inward drift. As well as this for high kick frequencies, particularly in the higher torques there is a lowering of the drift -very-close to the boundary (at $\sim 50\mu$m). This is likely due to the fact that the swimmers in these cases are quickly scattered and so this area is less likely to give an active displacement toward the channel centre for the colloid.

Next, we will look at the value of $m_2(y)$. Here, oppositely to $m_1(y)$: Yellow corresponds to larger magnitudes, while blue to the lower, since all values of $m_2(y)$ are necessarily positive. As with $m_1(y)$ there is a general pattern in all cases with slight differences. We see a bulk value and an increased value close to the boundaries. Looking closely, there is also a reduction in the value of $m_2(y)$ which sits between the enhanced region and the bulk. This is particularly the case for lower kick-frequencies. The differences arise for the higher torques (k-l), present in a larger difference in high vs. low frequencies' increased m_2 value, with lower kick frequencies the increase is more similar across the length of the plot, while for higher torques there is more of an increase on the left than right (at $\sim 47\mu$m). With this, there is a greater depression in the m_2 value for the higher torques' lower frequency cases (at $\sim 40\mu$m).

Finally, we have the average encounter rate $\lambda(y)$. For the most part this actually turns out to be relatively constant throughout the channel in each reali-sation of the system. There is a slight increase in the value near to the boundary,
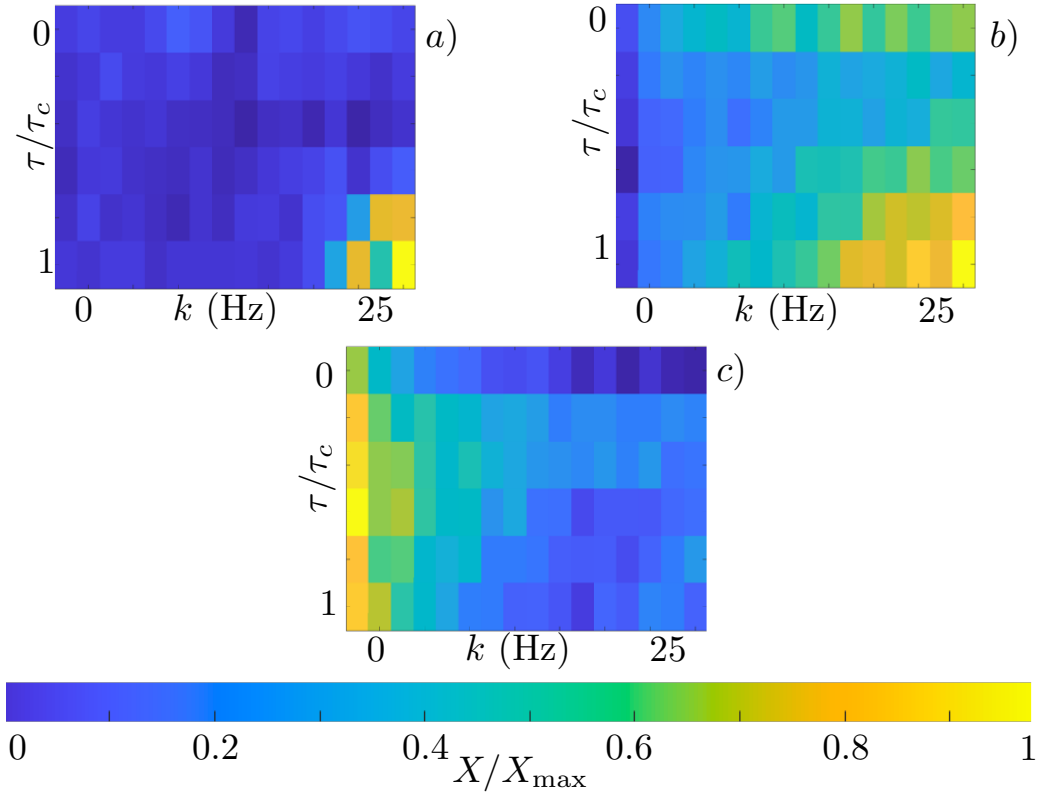
Figure 5.5: **Effective drift-diffusion model solution's associated accumulation** (a-c) Show the relative change in the accumulation according to distribution kurtosis (a), integration of the distribution near the boundary (b) and distribution variance (c).

specifically for the passive particles near to the boundary with low kick frequency swimmers.

5.3.3 Reconstructing the Distributions using the Jump-Diffusion Analytical Solution

Now that we have characterised the relevant spatially-dependent properties of the jumps within the simulation we can refer back to equation (3.23) from section 3.4.2. As before, if we think about the motion of the passive particles as the result of a jump-diffusion process coming from a coloured noise, then we can use $m_1(y), m_2(y)$ and, $\lambda(y)$ to construct effective diffusivities and drifts which the particles are subjected to. The result of which gives us a prediction of the positional distribution from the dynamic properties.

In figure 5.5 the calculation results of these distribution curves are shown.

As in figure 5.3 the kurtosis (a), boundary integration (b) and the variance (c) are shown. We see in the kurtosis and the integration methods, there is a good agreement with the positional distribution found directly from the trajectories. In both cases the peak in the value for high kick frequency and torque is present. For the kurtosis plot overall there is a greater amount of variance in the value for the lower kick frequencies, unlike what was seen in figure 5.3(a). 5.5(b) replicates many of the key features present in figure 5.3(b); the relative difference in the value for the low torque's high vs. low kick frequency cases can clearly be seen. Finally, in 5.5(c) we see the variance case. The low kick frequency cases are a reasonably good match with figure 5.3 (c). However, the slight increase in variance seen in a small number of high frequency and torque cases is not clearly present.

Overall, we see that the resulting distributions share a similar accumulation profile. With the correct scatter effects leading to the a similar portion of the passive particles near to the boundary.

Chapter 6

Conclusions

6.1 Conclusion

Within this thesis, we have looked at systems which are made up of active and passive particles, interacting with each other in confined environments. It has been a key theme throughout that the environment has lead to a non-homogeneous distribution of the swimmers and as a result, there is spatially dependent active-flux present which the passive particles experience and as such themselves acquire non-trivial distributions. Building on previous studies in the literature, which have shown that the geometry of a microfluidic device can be designed in such a way as to control the behaviour of microswimmers, we have detailed the impacts of the resulting swimmer distributions on passive particles. We have outlined two experimental set ups in chapters 3 and 4. The first being the straight channel experiments which showed that the non-equilibrium stationary state of the passive colloids could be understood as a result of the underlying spatially dependent dynamics of the colloids when exposed to the active particles. The second a different geometry, which has similar features of colloidal accumulation near to the boundary. By using a selective membrane we demonstrated that the active particles could be harnessed to segregate the colloids into side channels. In chapter 5 a model that studies how modifying the swimmer's boundary scattering, the colloid accumulation can be modified. In this section, the main results pertaining to the specifics of each of the chapters will be discussed and their place in the wider literature. After this, a short section on the reamining open questions and possible avenues for further inquiry will be presented.

6.1.1 Chapter Three

In this chapter we outlined a series of experiments, with a mixture of CR and polystyrene micro-colloids, confined using a microfludic device in straight channels. From these we were able to track the particles positions and thus, measure their steady-state. To do this, a jump-tracking algorithm was developed based on previous studies, utilising both the non-Brownian magnitudes and directional correlations of the colloid's trajectories to extract parts of their motion that were due to interactions with active particles. This steady-state, owing to the energy flux injected into the system by the swimmers, was non-equilibrium, yet had a defined profile if measured over a long time which was measured, the results of which were in line with previous studies of active particles in confinement. Showing that the presence of the boundary resulted in an accumulation of active particles. In addition to this the measured distribution of the colloids was non-monotonic and made up of a few key features: An accumulation peak near the boundary, depletion nearby and then a recovery within the bulk of the microfluidic channel to a flat (uniform) value. In an effort to understand these distributions, using the trajectory data for the colloids, we extracted a series of large non-Brownian moves, which we called jumps. Based on previous work, that has shown that the dynamics of passive particles in bulk comes largely as a result of entrainment events, it was hypothesised that these jumps were what lead to the colloid distribution. These jumps were then shown to have spatially dependent properties. By looking at the motion of the colloid's different properties projected perpendicular to the boundaries of the channel, the spatial differences were characterised. Following this, first by use of inverse-sampling of the distributions of these jumps in a numerical simulation, we were able to reconstruct the colloid distribution and the result was in good agreement with what we observed experimentally. This validated our initial hypothesis that that jumps were central to understanding the positional distributions. Particularly that the diffusivity of the colloids and swimmer encounter time was not crucial to capture the stationary state. However, asymmetries in the properties of jumps toward and away from the boundaries proved fundamental to predicting their behaviour. Building on this, a new semi-analytical jump-diffusion model was outlined and the results of this model were again a good agreement with the experimental measurements.

6.1.2 Chapter Four

Following on from the results from chapter three, in this chapter we describe another experimental set up. This time, designed to exploit the distributions seen for the

colloids, in tandem with a semi-permeable membrane, to separate out the passive particles from the mixture. We showed that the colloid positional distributions share the key-features from the straight channels if we account for the area of the annuli on which they are measured. We also see that, with the inclusion of off-shoots which can fit the colloids but not the swimmers, the colloids will indeed segregate. We classified the experimental dynamics of the segregation, which can be reasonably well fitted by first-order kinetics. From such a fit, we can then extract rates at which the colloids enter and exit the channel via the off-shoots. Next, we showed using numerical solutions to the 'narrow escape problem' equations do not show a good match with the experimentally measured rates. However, using a numerical simulation, which contained a positionally-dependent effective drift and diffusivity of the form we found in chapter three, we get a very good match for the experimental rate.

6.1.3   Chapter Five

In section five we describe a simulation developed to explore problems similar to those outlined in chapters three and four. The origin of the code, specifically the various codes which inspired its design are discussed. Here we noted that previous studied of this sort have been performed with active rods and broken fore-aft symmetric swimmers in bulk. Our work makes several additions, including passive particles that can interact with the active particles, hard boundaries and also a near-boundary scattering of the active particles which has previously been characterised in experimental studies. Specifically, this scattering is introduced by way of a 'kick' process designed to emulate microswimmer boundary scattering caused by mechanical flagella-boundary interactions. We then measured positional distribution of passive particles within these mixed systems over a range of kick parameters. The values of three different measurements of the quantity of accumulation of passive particles is then explored, showing distinct regimes of boundary and bulk accumulation, depending on the parameters of the active particle scattering kicks. Early results suggest that by choosing swimmers which interact with boundaries in different ways that the distribution of the swimmers can be altered, and in turn the distribution of the colloids. Finally, using the semi-analytic results presented in chapter three, we extract the properties of jumps within the simulation and use these to reconstruct the distributions. The accumulation profiles of which show a good agreement with the direct measurements from the simulated trajectories.

6.2 Open Problems and Future Work

As with the resolution of any problem, results more often than not, contain more question than resolutions. As a result of the numerous discussions, seminars and conferences in which the research was presented, this work is no exception to that rule. In this section a few of the remaining open questions and further topics to be explored will be described.

6.2.1 Chapter Three

In addition to the current microfluidic device, one possibility is that further anisotropies could be added. Two reasonably straightforward examples of this are in utilisation of a chemical or light intensity gradient. To do this the microfluidic device itself could be exposed to a light intensity gradient or light introduced by way of an optical fibre. Thus, generating a bias in the swimmer direction. Alternatively, by choosing a different microfluidic in which media and chemicals are injected and flowed parallel to each other, a chemical gradient can be produced. As a result of either, in the case of CR, this would result in a preferential motion up (or down) such gradients. We would no longer be able to look at the measured colloidal dynamics in the direction perpendicular to the boundary. Instead, the parallel direction would also come into play. This is something that we hope to first explore using the code from chapter five. By including into the equation of motion for the particle's orientation a term to bias it along one direction of a straight channel, this can be simulated. In this case, it would be interesting to see if the swimmer dynamics near to the boundaries result in different colloidal dynamics.

6.2.2 Chapter Four

The experiments outlined in this section pertained to one of the simplest possible geometries. Microfluidics by their very nature enable the rapid prototyping and implementation of a broad range of designs. In figure 6.1 another channel geometry which could be explored experimentally is shown. These designs are a hybridisation of the straight channels with the off-shoots from the circular channel experiments, with pores between the channel pairs. The idea then, is that by changing the boundary modulation (which in this case is sinusoidal) you can affect the swimmer distributions. This then would lead to a change in the colloid dynamics and possibly even circulations of colloids for adjacent pores.

One possibility building on this work is that such experimental systems could be utilised to measure swimming induced pressure. In this case the passive would
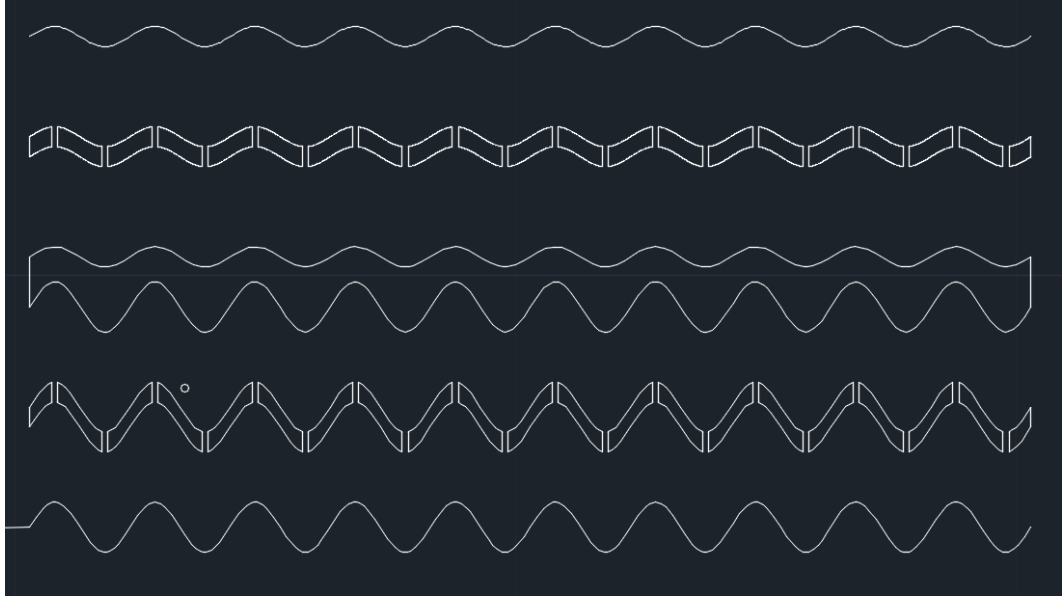
Figure 6.1: **Prototype microfluidic design for modulated boundaries.** Schematic of possible modulated boundary microfluidic channels. Two pairs of parallel channels are shown, with the top two having a lower amplitude of modulation than the bottom two. In both cases the modulation period is equal.

act as tracers in such experiments, to define and measure non-equilibrium analogs to pressure (swim pressure) [165, 166, 167, 168]. This might be measurable indirectly, by using an experimental set up similar to that of chapter four. Here, the aim would be to measure the exit rate of colloids for different swim-pressures.

For the approach using the narrow escape parallel using a constant diffusivity, further inclusion of a constant drift is eluded to in [145] to see whether this refinement improved the numerical solution. Further to this, the inclusion of spatially dependent drift and diffusivity (of a known functional form) into the narrow escape problem's numerical solution would be an interesting follow up.

For the numerical simulation, using the positionally dependent drift and diffusivity, we used the values from the drift-diffusion model outlined in chapter three. However, this model said nothing of the motion of the colloids parallel to the boundary. In data relating to this measurement, it looked to be the case that the parallel jump sizes were largely unaffected by the proximity to the boundary. As a result, a non-isotropic diffusivity could also be implemented to further verify the outcome. It is however possible that due to the large number of evenly spread exits that this would not be the case. Such a model, with this directional inclusion, could complement well the taxis experiments described in 6.2.1.

6.2.3 Chapter Five

The simulation opens several possible exciting avenues of progress. Indeed the work presented in this thesis is from an as yet incomplete project.

Firstly, as with the jumps from chapter three, it would be nice to use inverse-sampling to reconstruct the distributions for the passive particles to compare their shape to that was found in the directly measured distributions.

To build on the simulation, similar to the geometry as shown in 6.1, a preliminary code has been written. This code has all of the boundaries in the system periodic and then running through the centre of the long axis is a line of overlapping passive particles, modified so they cannot be moved by the swimmers/passive particles. The line itself can be either straight or modulated and can be written to have gaps (which could replace the inter-channel off-shoots). That way we can have boundaries with modulation. Clearly, due to the large number of passive particles required, there are computational limitations that need to be overcome to make reasonable data-collection viable for this code.

Next, as discussed in the possible progress avenues for the work in chapter three, inclusion of anisotropy in the swimmer orientation dynamics parallel to the boundary would be interesting to explore. Similarly to how the kicks are implemented near the boundary with a constant torque, a small torque could be applied to the swimmers at all times to model chemo/photo-tactic behaviour. That way the code could allow such systems to be explored.

Finally, there has been some recent developments in understanding microswimmer distributions for arbitrary geometries by analysing the fluxes generated by their motion [149]. In all the work within this thesis we have understood the resulting distributions for the passive particles in terms of the moments of their jump distributions. It would be interesting to explore whether the distributions could instead be understood in terms of the fluxes induced by the swimmers themselves. That way, instead of measuring the colloid trajectory (as a result of the active fluxes it is subjected to) to predict its distribution, we could look directly at the active fluxes themselves and predict the resulting distributions. The simulation offers a straightforward way in which the active fluxes could be tuned, the colloid dynamics measured. Then the measures compared to the results for specific cases of straightforward active fluxes.

Bibliography

[1] S. Ramaswamy. The Mechanics and Statistics of Active Matter. *Annual Review of Condensed Matter Physics*, 1(1):323–345, 2010.

[2] M.C. Marchetti, J.F. Joanny, S. Ramaswamy, T.B. Liverpool, J. Prost, M. Rao, and R.A. Simha. Hydrodynamics of soft active matter. *Rev. Mod. Phys.*, 85(3):1143–1189, 2013.

[3] H.S. Jennings and J.H. Crosby. Studies on reaction to stimuli in unicellular organisms. -VII The manner in which bacteria react to stimuli, especially chemical stimuli. *American Journal of Physiology-Legacy Content*, 6(1):31–37, 1901.

[4] H.C. Berg and D.A. Brown. Chemotaxis in Escherichia coli analysed by Three-dimensional Tracking. *Nature*, 239(5374):500–504, 1972.

[5] H.C. Berg and R.A. Andersen. Bacteria Swim by Rotating their Flagellar Filaments. *Nature*, 245(5425):380–382, 1973.

[6] H.C. Berg. Bacterial behaviour. *Nature*, 254(5499):389–392, 1975.

[7] E.M. Purcell. Life at low Reynolds number. *American Journal of Physics*, 45(1):3–11, jan 1977.

[8] E Lauga, T Powers, The hydrodynamics of swimming microorganisms *Rep. Prog. Phys.*, 72 096601, 2009

[9] K. Bente, S. Mohammadinejad, M.A. Charsooghi, F. Bachmann, A. Codutti, C.T. Lefèvre, S. Klumpp, and D. Faivre. High-speed motility originates from cooperatively pushing and pulling flagella bundles in bilophotrichous bacteria. *eLife*, 9:e47551, 2020.

[10] S.G. McInally and S.C. Dawson. Eight unique basal bodies in the multi-flagellated diplomonad Giardia lamblia. *Cilia*, 5(1):21, 2016.

[11] S.C. Dawson and S.A. House. Life with eight flagella: flagellar assembly and division in Giardia. *Current opinion in microbiology*, 13(4):480–490, 2010.

[12] R. Jeanneret, M. Contino, and M. Polin. A brief introduction to the model microswimmer Chlamydomonas reinhardtii. *The European Physical Journal Special Topics*, 225(11-12):2141–2156, 2016.

[13] J Elgeti et. al. Physics of microswimmers—single particle motion and collective behavior: a review *Rep. Prog. Phys.*, 78 056601, 2015

[14] R. Henshaw, R. Jeanneret, and M. Polin. Phototaxis of the dominant marine pico-eukaryote Micromonas sp.: from population to single cell. *bioRxiv*, 2019.

[15] M. Polin, I. Tuval, K. Drescher, J.P. Gollub, and R.E. Goldstein. Chlamydomonas Swims with Two "Gears" in a Eukaryotic Version of Run-and-Tumble Locomotion. *Science*, 325(5939):487–490, 2009.

[16] A.P. Solon, M.E. Cates, and J. Tailleur. Active brownian particles and run-and-tumble particles: A comparative study. *The European Physical Journal Special Topics*, 224(7):1231–1262, 2015.

[17] J. Bastos-Arrieta, A. Revilla-Guarinos, W.E. Uspal, and J. Simmchen. Bacterial Biohybrid Microswimmers. *Frontiers in Robotics and AI*, 5, 2018.

[18] H. Su, C.A. Hurd-Price, L. Jing, Q. Tian, J. Liu, and K. Qian. Janus particles: design, preparation, and biomedical applications. *Materials Today Bio*, 4:100033, 2019.

[19] C. Bechinger, R. Di Leonardo, H. Löwen, C. Reichhardt, G. Volpe, and G. Volpe. Active particles in complex and crowded environments. *Rev. Mod. Phys.*, **88**, 045006, 2016.

[20] R.F. Ismagilov, A. Schwartz, N. Bowden, and G.M. Whitesides. Autonomous Movement and Self-Assembly. *Angewandte Chemie International Edition*, 41(4):652–654, 2002.

[21] S. Auschra, A. Bregulla, K. Kroy, and F. Cichos. Thermotaxis of Janus particles. *The European Physical Journal E*, 44(7):90, 2021.

[22] N. Yu, X. Lou, K. Chen, and M. Yang. Phototaxis of active colloids by self-thermophoresis. *Soft Matter*, 15(3):408–414, 2019.

[23] A. Jee, Y. Cho, S. Granick, and T. Tlusty. Catalytic enzymes are active matter. *Proceedings of the National Academy of Sciences*, 115(46):E10812–E10821, 2018.

[24] J.P. Hernandez-Ortiz, C.G. Stoltz, and M.D. Graham. Transport and Collective Dynamics in Suspensions of Confined Swimming Particles. *Phys. Rev. Lett.*, 95(20):204501, 2005.

[25] S. Das, G. Gompper, and R.G. Winkler. Confined active Brownian particles: theoretical description of propulsion-induced accumulation. *New Journal of Physics*, 20(1):15001, 2018.

[26] R. Jeanneret, D. Pushkin, and M. Polin. Confinement Enhances the Diversity of Microbial Flow Fields. *Phys. Rev. Lett.*, **123**, 248102, 2019.

[27] L. Caprini, F. Cecconi, and U. Marini Bettolo Marconi. Transport of active particles in an open-wedge channel. *Journal of Chemical Physics*, 150(14), 2019.

[28] S. Das, S. Ghosh, and R. Chelakkot. Aggregate morphology of active Brownian particles on porous, circular walls. *Phys. Rev. E*, 102(3):32619, 2020.

[29] G. Li, J. Bensson, L. Nisimova, D. Munger, P. Mahautmr, J.X. Tang, M.R. Maxey, and Y.V. Brun. Accumulation of swimming bacteria near a solid surface. *Phys. Rev. E*, **84**, 041932, 2011.

[30] S Xiao, Z Wang, H.Y. Chen, Y.Jane. Sheng, and H.K. Tsao. Diffusion and surface excess of a confined nanoswimmer dispersion. *Journal of Chemical Physics*, 141(18), 2014.

[31] E Lauga, W DiLuzio, G Whitesides, H Stone. Swimming in Circles: Motion of Bacteria near Solid Boundaries *Biophys J.*, 90(2): 400–412, 2006

[32] X.L. Wu and A. Libchaber. Particle diffusion in a quasi-two-dimensional bacterial bath. *Phys. Rev. Lett.*, 84, 3017, 2000.

[33] M.J. Kim and K.S. Breuer. Enhanced diffusion due to motile bacteria. *Physics of Fluids*, **16**, L78, 2004.

[34] C. Valeriani, M. Li, . Novosel, J. Arlt, and D. Marenduzzo. Colloids in a bacterial bath: Simulations and experiments. *Soft Matter*, **7**, 5228-5238, 2011.

[35] A. Jepson, V.A. Martinez, J. Schwarz-Linek, A. Morozov, and W.C.K. Poon. Enhanced diffusion of nonswimmers in a three-dimensional bath of motile bacteria. *Phys. Rev. E*, **88**, 041002(R), 2013.

[36] L. Angelani, C. Maggi, M. L Bernardini, A. Rizzo, and R. Di Leonardo. Effective Interactions between Colloidal Particles Suspended in a Bath of Swimming Cells. *Phys. Rev. Lett.*, 107(13):138302, 2011.

[37] G.L Miño, J. Dunstan, A. Rousselet, E. Clément, and R. Soto. Induced diffusion of tracers in a bacterial suspension: theory and experiments. *Journal of Fluid Mechanics*, 729:423–444, 2013.

[38] G. Miño, T.E. Mallouk, T. Darnige, M. Hoyos, J. Dauchet, J. Dunstan, R. Soto, Y. Wang, A. Rousselet, and E. Clement. Enhanced diffusion due to active swimmers at a solid surface. *Phys. Rev. Lett.*, 106, 048102, 2011.

[39] Y. Huang, W. Ou, M. Chen, Z. Lu, N. Jiang, Y. Liu, X. Qiu, and Q. Zhou. Taylor dispersion in two-dimensional bacterial turbulence. *Physics of Fluids*, **29**, 051901, 2017.

[40] E.F. Semeraro, J.M. Devos, and T. Narayanan. Effective interactions and dynamics of small passive particles in an active bacterial medium. *The Journal of Chemical Physics*, 148(20):204905, 2018.

[41] A. Lagarde, N. Dagès, T. Nemoto, V. Démery, D. Bartolo, and T. Gibaud. Colloidal transport in bacteria suspensions: from bacteria collision to anomalous and enhanced diffusion. *Soft Matter*, 16(32):7503–7512, 2020.

[42] S. Ye, P. Liu, Z. Wei, F. Ye, M. Yang, and K. Chen. Constraint dependence of average potential energy of a passive particle in an active bath. *Chinese Physics B*, 29(5):58201, 2020.

[43] K.C. Leptos, J.S. Guasto, J.P. Gollub, A.I. Pesci, and R.E. Goldstein. Dynamics of Enhanced Tracer Diffusion in Suspensions of Swimming Eukaryotic Microorganisms. *Phys. Rev. Lett.*, 103(19):198103, 2009.

[44] H Kurtuldu, J.S. Guasto, K.A. Johnson, and J.P. Gollub. Enhancement of biomixing by swimming algal cells in two-dimensional films. *Proceedings of the National Academy of Sciences*, 108(26):10391–10395, 2011.

[45] O. Yang, Y. Peng, Z. Liu, C. Tang, X. Xu, and X. Cheng. Dynamics of ellipsoidal tracers in swimming algal suspensions. *Phys. Rev. E*, 94(4):42601, 2016.

[46] R. Jeanneret, D. Pushkin, V. Kantsler, and M. Polin. Entrainment dominates the interaction of microalgae with micron-sized objects. *Nature Communications*, 7(1):12518, 2016.

[47] T. Kurihara, M. Aridome, H. Ayade, I. Zaid, and D. Mizuno. Non-Gaussian limit fluctuations in active swimmer suspensions. *Phys. Rev. E*, 95, 030601(R), 2017.

[48] L. Ortlieb, S. Rafaï, P. Peyla, C. Wagner, and T. John. Statistics of Colloidal Suspensions Stirred by Microswimmers. *Phys. Rev. Lett.*, 122(14):148101, 2019.

[49] F. von Rüling, F. Kolley, and A. Eremin. Diffusive dynamics of elongated particles in active colloidal suspensions of motile algae. *Colloid and Polymer Science*, 299(2):289–296, 2021.

[50] P.T. Underhill, J.P. Hernandez-Ortiz, and M.D. Graham. Diffusion and Spatial Correlations in Suspensions of Swimming Particles. *Phys. Rev. Lett.*, 100(24):248101, 2008.

[51] J. Harder, S.A. Mallory, C. Tung, C. Valeriani, and A. Cacciuto. The role of particle shape in active depletion. *The Journal of Chemical Physics*, 141(19):194901, 2014.

[52] J.J. Molina and R. Yamamoto. Diffusion of colloidal particles in swimming suspensions. *Molecular Physics*, 112(9-10):1389–1397, 2014.

[53] J. de Graaf and J. Stenhammar. Stirring by periodic arrays of microswimmers. *Journal of Fluid Mechanics*, 811:487–498, 2017.

[54] E.W. Burkholder and J.F. Brady. Tracer diffusion in active suspensions. *Phys. Rev. E*, 95(5):52605, 2017.

[55] C. Yuan, A. Chen, B. Zhang, and N. Zhao. Activity–crowding coupling effect on the diffusion dynamics of a self-propelled particle in polymer solutions. *Phys. Chem. Chem. Phys.*, 21(43):24112–24125, 2019.

[56] C. Wang and H. Jiang. The inhibition of concentrated active baths. *The Journal of Chemical Physics*, 152(18):184907, 2020.

[57] J. Reichert and T. Voigtmann. Tracer dynamics in crowded active-particle suspensions. *Soft Matter*, 17(46):10492–10504, 2021.

[58] S. Ye, P. Liu, F. Ye, K.Chen, and M. Yang. Active noise experienced by a passive particle trapped in an active bath. *Soft Matter*, 16(19):4655–4660, 2020.

[59] L. Wang and J. Simmchen. Review: Interactions of Active Colloids with Passive Tracers. *Condens. Matter*, 4(3), 78, 2019.

[60] M. Huang, J. Schofield, and R. Kapral. Transport in active systems crowded by obstacles. *Journal of Physics A: Mathematical and Theoretical*, 50(7):74001, 2017.

[61] J. Katuri, E. William , M.P. Mihail, and S. Sánchez. Inferring non-equilibrium interactions from tracer response near confined active Janus particles. *Science Advances*, 7(18):eabd0719, 2022.

[62] D. Debnath, P.K. Ghosh, Y. Li, F. Marchesoni, and B. Li. Communication: Cargo towing by artificial swimmers. *The Journal of Chemical Physics*, 145(19):191103, 2016.

[63] J. Stenhammar, C. Nardini, R.W. Nash, D. Marenduzzo, and A. Morozov. Role of Correlations in the Collective Behaviour of Microswimmer Suspensions. *Phys. Rev. Lett.* 119, 028005, 2017.

[64] Q. Yang, H. Liang, R. Liu, K. Chen, F. Ye, and M. Yang. Edge Transport and Self-Assembly of Passive Objects in a Chiral Active Fluid. *Chinese Physics Letters*, 38(12):128701, 2021.

[65] T. Eisenstecken, G. Gompper, and R.G. Winkler. Internal dynamics of semiflexible polymers with active noise. *The Journal of Chemical Physics*, 146(15):154903, 2017.

[66] X. Liu, H. Jiang, and Z. Hou. Non-monotonic dependence of polymer chain dynamics on active crowder size. *The Journal of Chemical Physics*, 152(20):204906, 2020.

[67] S.M. Mousavi, G. Gompper, and R.G. Winkler. Active bath-induced localization and collapse of passive semiflexible polymers. *The Journal of Chemical Physics*, 155(4):44902, 2021.

[68] B. Zhang, T. Lei, and N. Zhao. Comparative study of polymer looping kinetics in passive and active environments. *Phys. Chem. Chem. Phys.*, 23(21):12171–12190, 2021.

[69] B. Zhang, F. Tan, and N. Zhao. Polymer looping kinetics in active heterogeneous environments. *Soft Matter*, 17(45):10334–10349, 2021.

[70] M. Knežević and H. Stark. Effective Langevin equations for a polar tracer in an active bath. *New Journal of Physics*, 22(11):113025, 2020.

[71] S. Belan and M. Kardar. Active motion of passive asymmetric dumbbells in a non-equilibrium bath. *The Journal of Chemical Physics*, 154(2):24109, 2021.

[72] K. Goswami and K. Sebastian. Diffusion caused by two noises-active and thermal. *J. Stat. Mech.*, 083501, 2019.

[73] N. Koumakis, A. Lepore, C. Maggi, and R. Di Leonardo. Targeted delivery of colloids by swimming bacteria. *Nature Communications*, 4(1):2588, 2013.

[74] G.G.N. Thushari and J.D.M. Senevirathna. Plastic pollution in the marine environment. *Heliyon*, 6(8):e04709, 2020.

[75] M. Cole, P. Lindeque, E. Fileman, C. Halsband, R. Goodhead, J. Moger, and T.S. Galloway. Microplastic Ingestion by Zooplankton. *Environmental Science & Technology*, 47(12):6646–6655, 2013.

[76] A. Visser Biomixing of the Oceans? *Science*, 316(5826):838–839, 2007.

[77] J. Thiffeault and S. Childress. Stirring by swimming bodies. *Physics Letters A*, 374(34):3487–3490, 2010.

[78] E. Pinçe, S. K P Velu, A. Callegari, P. Elahi, S. Gigan, G. Volpe, and G. Volpe. Disorder-mediated crowd control in an active matter system. *Nature Communications*, 7(1):10907, 2016.

[79] S. Gokhale, J. Li, A. Solon, J. Gore, and N. Fakhri. Dynamic clustering of passive colloids in dense suspensions of motile bacteria. *Phys. Rev. E*, **105**, 054605, 2021.

[80] P. Dolai, A. Simha, and S. Mishra. Phase separation in binary mixtures of active and passive particles. *Soft Matter*, 14(29):6137–6145, 2018.

[81] L. Angelani. Spontaneous assembly of colloidal vesicles driven by active swimmers. *Journal of physics. Condensed matter : an Institute of Physics journal*, 31(7):75101, feb 2019.

[82] F. Hauke, H. Löwen, and B. Liebchen. Clustering-induced velocity-reversals of active colloids mixed with passive particles. *The Journal of Chemical Physics*, 152(1):14903, 2020.

[83] D. Rogel Rodriguez, F. Alarcon, R. Martinez, J. Ramírez, and C. Valeriani. Phase behaviour and dynamical features of a two-dimensional binary mixture of active/passive spherical particles. *Soft Matter*, 16(5):1162–1169, 2020.

[84] Y. Wang, Z. Shen, Y. Xia, G. Feng, and W. Tian. Phase separation and super diffusion of binary mixtures of active and passive particles*. *Chinese Physics B*, 29(5):53103, 2020.

[85] S.A. Mallory, M.L. Bowers, and A. Cacciuto. Universal reshaping of arrested colloidal gels via active doping. *The Journal of Chemical Physics*, 153(8):84901, 2020.

[86] F. Kümmel, P. Shabestari, C. Lozano, G. Volpe, and C. Bechinger. Formation, compression and surface melting of colloidal clusters by active particles. *Soft Matter*, 11(31):6187–6191, 2015.

[87] J. Palacci, S. Sacanna, A. P. Steinberg, D. J. Pine, P. M. Chaikin. Living crystals of light-activated colloidal surfers. *Science 339* 936-940 (2013),

[88] J. Zhang, E. Luijten, and S. Granick. Toward Design Rules of Directional Janus Colloidal Assembly. *Annual Review of Physical Chemistry*, 66(1):581–600, 2015.

[89] S.A. Mallory, C. Valeriani, and A. Cacciuto. Curvature-induced activation of a passive tracer in an active bath. *Phys. Rev. E*, 90(3):32309, 2014.

[90] G. Mishler, A. C.H. Tsang, and O.S. Pak. Hydrodynamic Capture and Release of Passively Driven Particles by Active Particles Under Hele-Shaw Flows. *Journal of Nonlinear Science*, 28(4):1379–1396, 2018.

[91] B. Kichatov, A. Korshunov, V. Sudakov, V. Gubernov, A. Golubkov, and A. Kiverin. Superfast Active Droplets as Micromotors for Locomotion of Passive Droplets and Intensification of Mixing. *ACS Applied Materials & Interfaces*, 13(32):38877–38885, 2021.

[92] C.J. Olson Reichhardt and C. Reichhardt. Ratchet Effects in Active Matter Systems. *Annual Review of Condensed Matter Physics*, 8(1):51–75, 2017.

[93] J. Schwarz-Linek, C. Valeriani, A. Cacciuto, M.E. Cates, D. Marenduzzo, A.N. Morozov, and W.C.K. Poon Phase separation and rotor self-assembly in active particle suspensions. *Proceedings of the National Academy of Sciences*, 109(11):4052–4057, 2012.

[94] R. Zakine, A. Solon, T. Gingrich, and F. Van Wijland. Stochastic Stirling Engine Operating in Contact with Active Baths. *Entropy*, 19(5), 2017.

[95] P. Pietzonka, É. Fodor, C. Lohrmann, M.E. Cates, and U. Seifert. Autonomous Engines Driven by Active Matter: Energetics and Design Principles. *Phys. Rev. X*, 9(4):41032, 2019.

[96] A. Saha and R. Marathe. Stochastic work extraction in a colloidal heat engine in the presence of colored noise. *Journal of Statistical Mechanics: Theory and Experiment*, 2019(9):94012, 2019.

[97] V. Holubec, S. Steffenoni, G. Falasco, and K. Kroy. Active Brownian heat engines. *Phys. Rev. Research*, 2(4):43262, 2020.

[98] V. Holubec and R. Marathe. Underdamped active Brownian heat engine. *Phys. Rev. E*, 102(6):60101, 2020.

[99] A. Gopal, É. Roldán, and S. Ruffo. Energetics of critical oscillators in active bacterial baths. *Journal of Physics A: Mathematical and Theoretical*, 54(16):164001, 2021.

[100] É. Fodor and M.E. Cates. Active engines: Thermodynamics moves forward. *Europhysics Letters*, 134(1):10003, 2021.

[101] S.E. Spagnolie and E. Lauga. Hydrodynamics of self-propulsion near a boundary: predictions and accuracy of far-field approximations. *Journal of Fluid Mechanics*, 700:105–147, 2012.

[102] M.T. Downton and H. Stark. Simulation of a model microswimmer. *Journal of Physics: Condensed Matter*, 21(20):204101, 2009.

[103] T. Bickel, A. Majee, and A. Würger. Flow pattern in the vicinity of self-propelling hot Janus particles. *Phys. Rev. E*, 88(1):12301, 2013.

[104] G.K. Batchelor. Slender-body theory for particles of arbitrary cross-section in Stokes flow. *Journal of Fluid Mechanics*, 44(3):419–440, 1970.

[105] H. Shum and E.A. Gaffney. Chapter 2 - Mathematical Models for Individual Swimming Bacteria. In MinJun Kim, A Agung Julius, and Edward B T Microbiorobotics Steager, editors, *Micro and Nano Technologies*, pages 29–54. William Andrew Publishing, Boston, 2012.

[106] T.V. Kasyap, D.L. Koch, and M. Wu. Hydrodynamic tracer diffusion in suspensions of swimming bacteria. *Physics of Fluids*, 26(8), 2014.

[107] J. de Graaf and J. Stenhammar. Lattice-Boltzmann simulations of microswimmer-tracer interactions. *Physical review. E*, 95(2-1):23302, 2017.

[108] C. Jin, Y. Chen, C.C. Maass, and A.J.T.M. Mathijssen. Collective Entrainment and Confinement Amplify Transport by Schooling Microswimmers. *Phys. Rev. Lett.*, 127(8):88006, 2021.

[109] A.J.T.M. Mathijssen, D.O. Pushkin, and J.M. Yeomans. Tracer trajectories and displacement due to a micro-swimmer near a surface. *Journal of Fluid Mechanics*, 773:498–519, 2015.

[110] R.C. Krafnick and A.E. Garcia. Impact of hydrodynamics on effective interactions in suspensions of active and passive matter. *Phys. Rev. E*, 91(2):22308, 2015.

[111] O. Granek, Y. Baek, Y. Kafri, and A.P. Solon. Bodies in an interacting active fluid: far-field influence of a single body and interaction between two bodies. *Journal of Statistical Mechanics: Theory and Experiment*, 2020(6):63211, 2020.

[112] O.T. Dyer and R.C. Ball. Influence of thermal fluctuations on active diffusion at large Péclet numbers. *Physics of Fluids*, 33(5):51904, 2021.

[113] H. Shum and J.M. Yeomans. Entrainment and scattering in microswimmer-colloid interactions. *Phys. Rev. Fluids*, 2(11):113101, 2017.

[114] A.J.T.M. Mathijssen, R. Jeanneret, and M. Polin. Universal entrainment mechanism controls contact times with motile cells. *Phys. Rev. Fluids*, **3**, 033103, 2018.

[115] E.H. Harris, D.B. Stern, and G.B.B.T. Witman. The Chlamydomonas Source Book. Elizabeth H Harris, David B Stern, and George B B T The Chlamydomonas Sourcebook (Second Edition) Witman, editors, *The Chlamydomonas Sourcebook*, page iii. Academic Press, London, 2009.

[116] The Chlamy Collection. CC-125 History. https://www.chlamycollection.org/?f=strains&s=cc-125&chromosome=&locus=&strain_source=&accession_year=&collection=

[117] T. Pröschold, E.H. Harris, and A.W. Coleman. Portrait of a species: Chlamydomonas reinhardtii. *Genetics*, 170(4):1601–1610, aug 2005.

[118] Merchant Sabeeha S., Prochnik Simon E., Vallon Olivier, Harris Elizabeth H., Karpowicz Steven J., Witman George B., Terry Astrid, Salamov Asaf, Fritz-Laylin Lillian K., Maréchal-Drouard Laurence, Marshall Wallace F., Qu Liang-Hu, Nelson David R., Sanderfoot Anton A., Spalding Martin H., Kapitonov Vladimir V., Ren Qinghu, Ferris Patrick, Lindquist Erika, Shapiro Harris, Lucas Susan M., Grimwood Jane, Schmutz Jeremy, Cardol Pierre, Cerutti Heriberto, Chanfreau Guillaume, Chen Chun-Long, Cognat Valérie, Croft Martin T., Dent Rachel, Dutcher Susan, Fernández Emilio, Fukuzawa Hideya, González-Ballester David, González-Halphen Diego, Hallmann Armin, Hanikenne Marc, Hippler Michael, Inwood William, Jabbari Kamel, Kalanon Ming, Kuras Richard, Lefebvre Paul A., Lemaire Stéphane D., Lobanov Alexey V., Lohr Martin, Manuell Andrea, Meier Iris, Mets Laurens, Mittag Maria, Mittelmeier Telsa, Moroney James V., Moseley Jeffrey, Napoli Carolyn, Nedelcu Aurora M., Niyogi Krishna, Novoselov Sergey V., Paulsen Ian T., Pazour Greg, Purton Saul, Ral Jean-Philippe, Riaño-Pachón Diego Mauricio, Riekhof Wayne, Rymarquis Linda, Schroda Michael, Stern David, Umen James, Willows Robert, Wilson Nedra, Zimmer Sara Lana, Allmer Jens, Balk Janneke, Bisova Katerina, Chen Chong-Jian, Elias Marek, Gendler Karla, Hauser Charles, Lamb Mary Rose, Ledford Heidi, Long Joanne C., Minagawa Jun, Page M Dudley, Pan Junmin, Pootakham Wirulda, Roje Sanja, Rose Annkatrin, Stahlberg Eric, Terauchi Aimee M., Yang Pinfen, Ball Steven, Bowler Chris, Dieckmann Carol L., Gladyshev Vadim N., Green Pamela, Jorgensen Richard, Mayfield Stephen, Mueller-Roeber Bernd, Rajamani Sathish, Sayre Richard T., Brokstein Peter, Dubchak Inna, Goodstein David, Hornick Leila, Huang Y Wayne, Jhaveri Jinal, Luo Yigong, Martínez Diego, Ngau Wing Chi Abby, Otillar Bobby, Poliakov Alexander, Porter Aaron, Szajkowski Lukasz, Werner Gregory, Zhou Kemin, Grigoriev Igor V., Rokhsar Daniel S., and Grossman Arthur R. The Chlamydomonas Genome Reveals the Evolution of Key Animal and Plant Functions. *Science*, 318(5848):245–250, 2007.

[119] S.E. Barsel, D.E. Wexler, and P.A. Lefebvre. Genetic analysis of long-flagella mutants of Chlamydomonas reinhardtii. *Genetics*, 118(4):637–648, 1988.

105

[120] Dolly K Khona, Venkatramanan G Rao, Mustafa J Motiwalla, P C Sreekrishna Varma, Anisha R Kashyap, Koyel Das, Seema M Shirolikar, Lalit Borde, Jayashree A Dharmadhikari, Aditya K Dharmadhikari, Siuli Mukhopadhyay, Deepak Mathur, and Jacinta S D'Souza. Anomalies in the motion dynamics of long-flagella mutants of Chlamydomonas reinhardtii. *Journal of biological physics*, 39(1):1–14, 2013.

[121] The Chlamy Collection. TAP protocol. https://www.chlamycollection.org/methods/media-recipes/tap-and-tris-minimal/

[122] Polysciences. Polystyrene Microspheres. https://www.polysciences.com/german/catalog-products/microparticles-particles/polystyrene-microspheres

[123] K. Karin, W. Luisa, and B. Burkhard. The Contractile Vacuole as a Key Regulator of Cellular Water Flow in Chlamydomonas reinhardtii. *Eukaryotic Cell*, 13(11):1421–1430, 2014.

[124] M. Hung and J. Chang. Developing microfluidics for rapid protoplasts collection and lysis from plant leaf. *Proceedings of the Institution of Mechanical Engineers, Part N: Journal of Nanoengineering and Nanosystems*, 226(1):15–22, 2012.

[125] Darwin Microfluidics. Microfludics Image. https://darwin-microfluidics.com/products/pdms-biopsy-puncher-kit?variant=38608511553

[126] J. Friend and L. Yeo. Fabrication of microfluidic devices using polydimethylsiloxane. *Biomicrofluidics*, 4(2):26502, 2010.

[127] A. Alrifaiy, O. Lindahl, and K. Ramser. Polymer-Based Microfluidic Devices for Pharmacy, Biology and Tissue Engineering, *Polymers*, 4(3), 1349-1398, 2012.

[128] G.G. Morbioli, N.C. Speller, and A.M. Stockton. A practical guide to rapid-prototyping of PDMS-based microfluidic devices: A tutorial. *Analytica Chimica Acta*, 1135:150–174, 2020.

[129] Zeiss. Zeiss AxioVert 200M inverted microscope. https://www.manualslib.com/products/Zeiss-Axiovert-200-3105784.html

[130] H S M Bradbury, B Bracegirdle. *Introduction to Light Microscopy. Taylor & Francis*, 2019.

[131] S. Williams, R. Jeanneret, I. Tuval, and M. Polin. Confinement-induced accumulation and spontaneous de-mixing of microscopic active-passive mixtures, *Under review*, 2021.

[132] T. Caswell. Tracking Codes. http://tacaswell.github.io/tracking/html/

[133] Y. Gao and M.L. Kilfoil. Accurate detection and complete tracking of large populations of features in three dimensions. *Opt. Express*, 17(6):4685–4704, 2009.

[134] R. J. A Practical Guide to Spline. *Mathematics of Computation*, 34(149):325–326, 2022.

[135] I. Karatzas, S. Shreve. *Brownian Motion and Stochastic Calculus. Springer*, Graduate Texts in Mathematics volume 113, 1998.

[136] M.A. Omar, A. Aboul-Hassan, and S.I. Rabia. The composite Milstein methods for the numerical solution of Ito stochastic differential equations. *Journal of Computational and Applied Mathematics*, 235(8):2277–2299, 2011.

[137] Q. Guo, W. Liu, X. Mao, and R. Yue. The truncated Milstein method for stochastic differential equations with commutative noise. *Journal of Computational and Applied Mathematics*, 338:298–310, 2018.

[138] D.M. Heyes and H. Okumura. Equation of state and structural properties of the Weeks-Chandler-Andersen fluid. *The Journal of Chemical Physics*, 124(16):164507, 2006.

[139] D. Talay. *Numerical solution of stochastic differential equations. Stochastics and Stochastic Reports*, 47:1-2, 121-126, 1994.

[140] R.L. Honeycutt and I. White. Stochastic Runge-Kutta algorithms. I. White Noise. *Asymptotics, Nonparametrics, and Time Series*, 45(2):396–409, 1991.

[141] A.J. Roberts. Modify the Improved Euler scheme to integrate stochastic differential equations. *Arxiv preprint*, arXiv:1210.0933, 2012.

[142] H. Risken. Fokker-Planck Equation *Springer*, Springer Series in Synergetics, volume 18, 1996.

[143] M.R.R. Tabar. *Analysis and Data-Based Reconstruction of Complex Nonlinear Dynamical Systems: Using the Methods of Stochastic Processes. Springer*, Understanding Complex Systems, 2019.

[144] A. Singer, Z. Schuss, and D. Holcman. Narrow escape, part II: The circular disk. *Journal of Statistical Physics*, 122(3):465–489, 2006.

[145] S. Redner. *A Guide to First-Passage Processes. Cambridge University Press*, 9780511606014, 2001.

[146] A Costanzo *et al. Transport of self-propelling bacteria in microchannel flow. J. Phys.: Condens. Matter* 24 065101, 2012.

[147] V. Kantsler, J. Dunkel, M. Polin, and R. E. Goldstein Ciliary contact interactions dominate surface scattering of swimming eukaryotes *PNAS* 110 (4) 1187-1192, 2013.

[148] T. Ostapenko, F. J. Schwarzendahl, T. J. Böddeker, C. T. Kreis, J. Cammann, M. G. Mazza, and O. Bäumchen Curvature-Guided Motility of Microalgae in Geometric Confinement *Phys. Rev. Lett.*, **120**, 068002, 2018.

[149] J. Cammann, F. Jan Schwarzendahl, T. Ostapenko, D. Lavrentovich, O. Bäumchen, and M.G. Mazza. Boundary-interior principle for microbial navigation in geometric confinement. *ArXiv preprint*, arXiv:2011.02811, 2020.

[150] L.S. Mosby, M. Polin, and D.V. Köster. A Python based automated tracking routine for myosin II filaments. *Journal of Physics D: Applied Physics*, 53(30):304002, 2020.

[151] M. Contino. Characterisation and control of the dynamical properties of swimming microorganisms under confinement. *Warwick Thesis*, 2017.

[152] S.I. Denisov and Y.S. Bystrik. Statistics of bounded processes driven by Poisson white noise. *Physica A: Statistical Mechanics and its Applications*, 2019.

[153] S.I. Denisov, W. Horsthemke, and P. Hänggi. Generalized Fokker-Planck equation: Derivation and exact solutions. *The European Physical Journal B*, 68(4):567–575, 2009.

[154] K. Misiunas, S. Pagliara, E. Lauga, J.R. Lister, and U.F. Keyser. Nondecaying Hydrodynamic Interactions along Narrow Channels. *Phys. Rev. Lett.*, 115(3):38301, 2015.

[155] E. Locatelli, M. Pierno, F. Baldovin, E. Orlandini, Y. Tan, and S. Pagliara. Single-File Escape of Colloidal Particles from Microfluidic Channels. *Phys. Rev. Lett.*, 117(3):38001, 2016.

[156] P. Lançon, G. Batrouni, L. Lobry, and N. Ostrowsky. Drift without flux: Brownian walker with a space-dependent diffusion coefficient. *Europhysics Letters (EPL)*, 54(1):28–34, 2001.

[157] G. Pesce, A. McDaniel, S. Hottovy, J. Wehr, G. Volpe. Stratonovich-to-Itô transition in noisy systems with multiplicative feedback. *Nature Communications*, volume 4, Article number: 2733, 2013

[158] H.H. Wensink, V. Kantsler, R.E. Goldstein, and J. Dunkel. Controlling active self-assembly through broken particle-shape symmetry. *Phys. Rev. E* 89, 010302(R), 2014.

[159] H.H. Wensink and H. Löwen. Emergent states in dense systems of active rods: From swarming to turbulence. *J. Phys.: Condens. Matter*, **24** 464130,, 2012.

[160] M. Mercedes Tirado, C. López Martínez, and J. García De La Torre. Comparison of theories for the translational and rotational diffusion coefficients of rod-like macromolecules. Application to short DNA fragments. *The Journal of Chemical Physics*, 81(4):2047–2052, 1984.

[161] J.S. Rowlinson. The Yukawa potential. *Physica A: Statistical Mechanics and its Applications*, 156(1):15–34, 1989.

[162] M.S. Krieger. Microorganism billiards in closed plane curves. *The European Physical Journal E*, 39(12):122, 2016.

[163] E. Lushi, V. Kantsler, and R.E. Goldstein. Scattering of biflagellate microswimmers from surfaces. *Phys. Rev. E*, 96(2):23102, 2017.

[164] A. Kallner. Laboratory Statistics: Methods in Chemistry and Health Sciences, Formulas. *Elsevier*, 9780128143483, 2018.

[165] A.P. Solon, Y. Fily, A. Baskaran, M.E. Cates, Y. Kafri, M. Kardar, and J. Tailleur. Pressure is not a state function for generic active fluids. *Nature Physics*, 11(8):673–678, 2015.

[166] S.C. Takatori, W. Yan, and J.F. Brady. Swim Pressure: Stress Generation in Active Matter. *Phys. Rev. Lett.*, 113(2):28103, 2014.

[167] R. Wittmann, F. Smallenburg, and J.M. Brader. Pressure, surface tension, and curvature in active systems: A touch of equilibrium. *The Journal of Chemical Physics*, 150(17):174908, 2019.

[168] W. Yan and J.F. Brady. The force on a boundary in active matter. *Journal of Fluid Mechanics*, 785, R1, 2015.